BIOLOGICAL NANO SILICA REINFORCED POLYMERIC COMPOSITES

A Thesis Submitted to
the Graduate School of
İzmir Institute of Technology
in Partial Fulfillment of the Requirements for the Degree of

DOCTOR OF PHILOSOPHY

in Material Science and Engineering

by
Sevkan ÜLKER

December 2022
İZMİR

ACKNOWLEDGEMENTS

I'd like to thank Prof. Mustafa GÜDEN, my supervisor, for his technical, useful, and motivating assistance throughout my thesis study. I owe him a lot of gratitude for including me on his research team and for everything else he did to improve both my personal and professional circumstances. Having him as my advisor and working with him is a huge privilege.

I want to thank everyone who worked at the Dynamic Testing and Modeling Laboratory at IZTECH for the enjoyable times we had at work. I want to express my gratitude to Mesut BAYHAN, Mustafa Kemal SARIKAYA, Çetin BAKICI and Samed ENSER, in particular for their useful suggestions, technical assistance during my experimental investigations, and friendship.

I want to express my gratitude to the Center for Materials Research IZTECH's knowledgeable staff, in particular Mutlu Devran YAMAN, for helping me with the technical aspects of using the scanning electron microscope and conducting additional microstructural analysis for my thesis study.

Finally, I would like to express my sincere appreciation to my wife, Pınar ÇETİN ÜLKER, for always being a kind friend, an understanding listener, and an inspiring exhorter whenever I felt stuck in the trying periods during my educational life. Her presence, unwavering affection, and unending support enable me to accomplish my objectives. Without her, I could not have been successful. I am incredibly grateful for what she gave up for me. I'll make it my life's mission to make her proud of me.

ABSTRACT

BIOLOGICAL NANO SILICA REINFORCED POLYMERIC COMPOSITES

The present thesis study focused on processing nano-silica powders of varying sizes and crystallinities through heat treatment (900–1200 °C), hydrofluoric acid leaching (1–7 N), and ball milling (1 h, 500 rpm) of natural diatom frustules. As-received frustules was composed of amorphous silica (88%) and quartz. The partially ordered crystalline low-quartz and/or precursor to low-cristobalite started to form at ~900 °C. As the heat treatment temperature increased, the crystallinity of the frustules increased from 9.3% at 25 °C to 46% at 1200 °C. Applying a ball milling reduced the mean particle sizes of the as-received and heat-treated frustules from 15.6–13.7 μm to 7.2-6.7 μm, respectively. Acid leaching of the as-received and heat-treated frustules resulted in a further increase in the crystallinity. Furthermore, ball milling applied after an acid leaching was very effective in reducing the particle size of the as-received and heat-treated frustules. The mean particle size of the acid-leached frustules decreased to 774-547 nm with a crystallinity varying between 12 and 48% after ball milling. A partially dissolved amorphous phase was observed in between crystalline silica grains after acid leaching, which resulted in a rapid fracture/separation of the frustules in ball milling. The prepared nano-silica powders were further used as a filler in an epoxy matrix. The tensile strength, fracture strain, and modulus of epoxy increased with increasing the volume percent of nano-silica up to 2%. The increase in the yield strength and elastic modulus was about 50% and 30% with the addition of 2 vol% frustules, respectively. The rule of mixtures showed a very good agreement with the experimental elastic modulus values and a numerical model of the tensile test in LS-DYNA agreed well with the experimental tensile stress-strain behavior. The microscopic observations showed the presence of nano-silica powder, proving an efficient load transfer from matrix to powders on the fracture surfaces, confirming a strong interface between silica powders and matrix.

ÖZET

BİYOLOJİK NANO SİLİKA TAKVİYELİ POLİMERİK KOMPOZİTLER

Mevcut tez çalışması doğal diatom kabuklarının ısıl işlem (900-1200 °C), hidroflorik asit liçi (1-7 N) ve bilyeli öğütme (1 saat, 500 rpm) yoluyla değişen boyutlarda ve kristalliklerde nano-silika tozlarının işlenmesine odaklanmıştır. Temin edilen diatom kabuklarının amorf silika (%88) ve kuvars fazlarından oluşmuştur. Kısmen düzenli kristalli düşük kuvars ve/veya düşük kristobalit öncüsü ~900 °C'de oluşmaya başlamıştır. Isıl işlem sıcaklığı arttıkça, kabukların kristalliği 25 °C'de %9,3'ten 1200 °C'de %46'ya yükselmiştir. Bilyeli öğütme uygulamak, temin edilen ve ısıl işlem görmüş kabukların ortalama parçacık boyutlarını sırasıyla 15,6-13,7 μm'den 7,2-6,7 μm'ye düşürmüştür. Temin edilen ve ısıl işlem görmüş kabukların asitle yıkanması sonrası kristallikte daha fazla bir artışla sonuçlanmıştır. Ayrıca, asitle yıkamadan sonra uygulanan bilyeli öğütme, temin edilen ve ısıl işlem görmüş kabukların parçacık boyutunun küçültülmesinde çok etkili olmuştur. Asitle yıkanan kabukların ortalama parçacık boyutu, bilyeli öğütmeden sonra %12 ile %48 arasında değişen bir kristallik ile 774-547 nm'ye düşmüştür. Asitle yıkamadan sonra kristalli silika taneleri arasında kısmen çözünmüş amorf bir faz gözlemlenmiştir, bu da bilyeli öğütmede kabukların hızlı bir şekilde kırılmasına/ayrılmasına neden olmuştur. Hazırlanan nano-silika tozlar ayrıca bir epoksi matrisinde dolgu maddesi olarak kullanılmıştır. Çekme dayanımı, kırılma gerilmesi ve elastik modülü nano-silikanın hacim yüzdesinin %2'ye kadar artmasıyla artmıştır. Akma dayanımı ve elastik modüldeki artış, hacimce %2 kabukların eklenmesiyle sırasıyla yaklaşık %50 ve %30 olmuştur. Karışım kuralı, deneysel elastik modül değerleri ile çok iyi bir uyum göstermiştir ve LS-DYNA'daki çekme testinin sayısal bir modeli, deneysel çekme gerilimi-uzama davranışı ile iyi bir uyum sağlamıştır. Mikroskobik gözlemler, kırılma yüzeylerinde matristen tozlara verimli bir yük aktarımını kanıtlayan nano-silika tozunun varlığını göstermiştir ve silika tozları ile matris arasında güçlü bir arayüzü doğrulamıştır.

TABLE OF CONTENTS

LIST OF FIGURES

Figure **Page**

Figure **Page**

Figure **Page**

Figure **Page**

Figure **Page**

Figure **Page**

Figure **Page**

LIST OF TABLES

Table **Page**

LIST OF ABBREVIATIONS

XRD	X-Ray Diffraction
XRF	X-Ray Florescence Spectrometer
SEM	Scanning Electron Microscopy
FTIR	Fourier Transform Infrared Spectroscopy
TGA	Thermo Gravimetric Analysis
PP	Polypropylene
PA	Polyimide
PC	Polycarbonate
PEEK	Polyetheretherketone
UP	Unsaturated polyester
PU	Polyurethane
Si	Silicone
SBR	Styrene Butadiene Rubber
NR	Natural Rubber
HF	Hydrofluoric
HCl	Hydrochloric
TEM	Transmission Electron Microscopy
EDX	Energy Dispersive X-ray Spectroscopy
SiO_2	Silica
CNTs	Carbon Nanotubes
CR	Crystallite
AFM	Atomic Force Microscopy
DE	Diatomaceous Earth
CD	Calcined Diatom
ND	Natural Diatom

CHAPTER 1

INTRODUCTION

1.1. Background

The wide use of polymeric materials is simply due to their low-cost combined with their low density. On the other side, their engineering applications are limited, because of their comparatively low strength, stiffness and resistance to high temperatures. Light weight, strong and stiff fillers including silica (SiO_2), carbon nanotubes (CNTs), graphene and alumina (Al_2O_3), are usually added into polymers in order to enhance their thermal, mechanical, electrical and /or properties [1-5]. When the filler is nano-size, i.e. nano powder and/or whiskers, the resultant structure is called a nanocomposite [6]. Nanocomposites combine the advantages of an inorganic filler (e.g., rigidity, thermal stability) and a polymer matrix (e.g., flexibility, dielectric, ductility, and processability) [7] and, more nano-size filler causes a dramatic increase in the interfacial area between the filler and polymer as compared with traditional composites. This results in physical and mechanical properties that are quite different from those of a bulk polymer, even at very low filler percentages [8].

Diatoms are a group of photosynthetic unicellular microalgae [9], which have the highest variety among the microalgae and are considered the predominant group of primary producers of food in aquatic environments [10]. The shell of diatoms, known as frustule, is made of nano-size silica particles with an intricate 3D structure. When these aquatic plants cells die, the silica shell/frustules form diatomaceous earth (diatomite) on the floor of the ocean. Diatomaceous earth is an extremely cheap material, abundant, and extensively used in heat and sound insulation, explosives, abrasives, absorbents, and filters. [11]. In each year, the number of research articles on diatoms are increasing as they form a source of many different of bioactive substances (Figure 1.1) [12]. Intricate microscale polymeric and ceramic structures, such as zirconia [13, 14], gold nanostructures [15] and MgO and TiO_2 structures [16] can also be produced by employing diatom frustules as temporary scaffolds, templates, and catalysts in solid-gas displacement reactions, according to recent investigations. Recently, medical uses and the prospective

engineering of diatom frustules have also been suggested, containing targeted drug administration, metal film membranes, and the generation of bioactive compounds [17]. Due to their exceptional capacity for lipid accumulation during their dormancy and under specific stress conditions, diatoms are renowned for providing an important platform for the production of a variety of high-value products for the nutraceutical and pharmaceutical industries as well as the production of biofuel (Figure 1.2) [17]. They are also a source for processing nano silica powder, which is the main focus of this thesis study.

1.2. Scope of the Thesis

Present thesis focusses on processing nano-silica powders by means of a combined process of ball milling, acid leaching and heat-treatment. The selection of a combined process of heat-treatment and acid leaching was due to the fact that the amorphous silica phase dissolves more rapidly than the crystal phase in hydrofluoric acid [18]. After a leaching process, the leachate was filtered. Then, the filtered frustules (over filter frustules) were ball milled to obtain nano size particles. Both powders (under filter and ball milled over filter) can be directly added to a polymer matrix as reinforcement.

In the content of the thesis, the prepared powders were utilized as reinforcement in an epoxy matrix in order to determine its effect on the mechanical properties. Finally, the studied nano-silica processing method offers a new, natural, and economical way of obtaining nano-silica powders with different crystallinities.

The thesis is organized into seven chapters as

- Chapter 1: Brief introduction and the scope of the thesis
- Chapter 2: A literature survey on the properties of polymer nanocomposites
- Chapter 3: The formation, structure and potential applications diatom frustules
- Chapter 4: The experimental methodology used in the thesis study
- Chapter 5: The experimental results
- Chapter 6: The discussion of experimental results
- Chapter 7: Conclusions

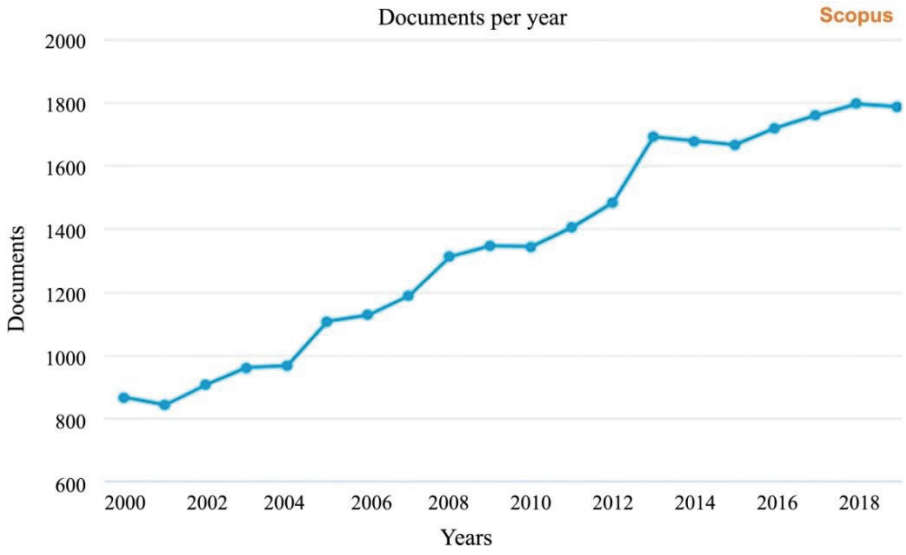

Figure 1.1. Data on diatom research trends, including the volume of publications per year, were obtained from Scopus.: https://www.scopus.com (using the keyword diatoms) [12].

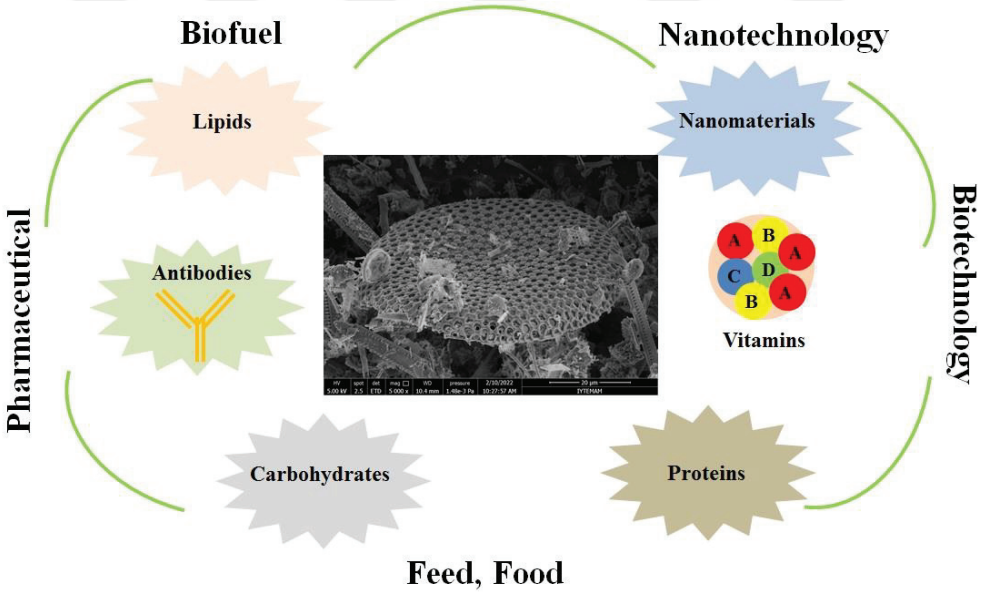

Figure 1.2. Schematic presentation, summarizing a number of molecules with extra benefits made from diatoms and their uses in many industries (modified [17]).

CHAPTER 2

POLYMER NANOCOMPOSITES

2.1. Introduction

A composite structure is made by mixing physically and chemically different at least two materials. It consists of a continuous and a discontinuous phase in a two-material composite system. The continuous phase is called matrix and the discontinuous phase reinforcement. The matrix surrounds the reinforcing phase, whereas the reinforcement modifies the properties of the matrix. The combination of reinforcement and matrix results in physical and chemical properties that are quite different from that of each constituent. Polymer matrix composites are relatively light; therefore, they are well-suited for the applications where the weight is an important design criterion like the automotive and aerospace industries [2, 5, 19, 20]. Other important properties of polymer matrix composites may include high corrosion resistance, nonconductive nature, one-piece design and vibration absorption tendency [21]. Polymer matrix composites are further durable, maintenance-free, dimensionally stable, easy transportation/installation and pest resistant materials [22].

In polymer matrix nanocomposites, the inorganic phase is nano-size [23, 24]. The small-size of fillers significantly increases the interfacial area between filler and matrix (Figure 2.1), which cannot be seen in traditional composites [3, 25]. The surface area/volume ratio (A/V) of particles increases with a decrease in particle size, and the ratio increases significantly for nano-size particles. A large interfacial area enhances the properties of a nanocomposite, even at very low loading ratios [6-8].

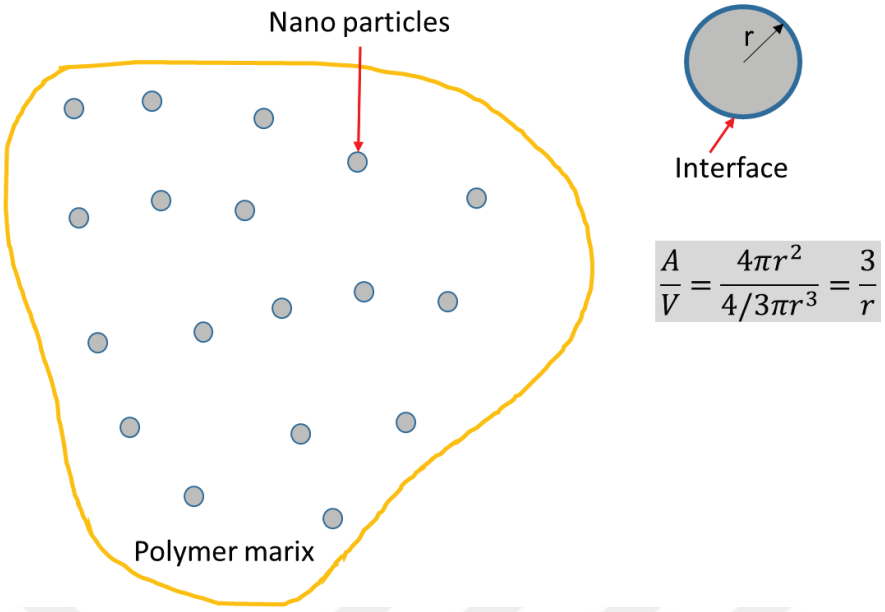

Figure 2.1. The schematic of nano-size particle reinforced polymer matrix composite and surface to volume ratio.

Most composites used by the industry today are polymer based and the most used matrices, that are thermosets, thermoplastics, and elastomers, are listed in Table 2.1. In thermosets, chemical cross-linking, which results in the production of a strong three-dimensional network structure between molecular chains, transforms the liquid resin into a hard, rigid solid (Figure 2.2(a)). They do not soften upon subsequent heating and contain large cross-linking percentages (10 to 50% of the chains). Heating to excessive temperatures causes severance of these crosslink bonds and polymer degradation. Due to these, they are harder and stronger than thermoplastics, and have better dimensional stability and corrosion resistance. Examples include epoxies, phenolic and polyester resins. The bonds between the chains in a thermoplastic polymer are however weaker, secondary type (Figure 2.2(b)). Therefore, they soften when heated and harden when cooled and are much more ductile than thermosets. Most linear polymers and those having some branched structures with flexible chains are thermoplastics. Examples include polypropylene, polyamide and polycarbonate. Elastomers have a few cross-linked molecular chains, which makes them extremely elastic. The cross-linked chains do not melt, and this makes the polymer an elastomer, capable of elastic extensions more than 100% or more which are recovered completely on unloading. Examples include polyurethane and silicone.

Table 2.1. Commonly used polymer matrices.

MATRIX		
Thermoset	**Thermoplastic**	**Elastomer**
Unsaturated polyester (UP)	Polypropylene (PP)	Polyurethane (PU)
Epoxy resins	Polyimide (PA)	Silicone (Si)
Vinyl ester resins	Polycarbonate (PC)	
Phenols	Polyetheretherketone (PEEK)	
	Styrene-butadiene rubber	
	Ethylene	

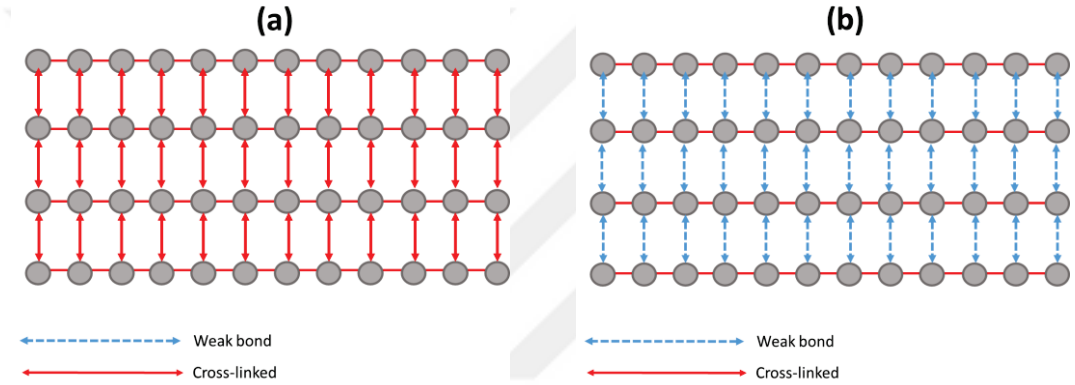

Figure 2.2. Bonding between the molecular chains of (a) a thermoset and (b) a thermoplastic.

Particulate fillers are grouped either inert or reinforcing. Inert fillers are usually added to increase the volume and to reduce the processing cost of polymers. For example, inert fillers are usually added into rubber for above purposes. Whereas, reinforcing fillers like carbon black and silica improve the mechanical properties, electrical conductivities, barrier properties, resistance to fire and ignition of rubber [26, 27].

Silica is one of the most widely found minerals in the Earth crust [28]. Crystalline silica has a repeating network of the silica-oxygen tetrahedron, while amorphous silica has a random arrangement of the network (Figure 2.3). The amorphous structure has an open structure in which positive ions such as Na^+ can readily migrate (Figure 2.3).

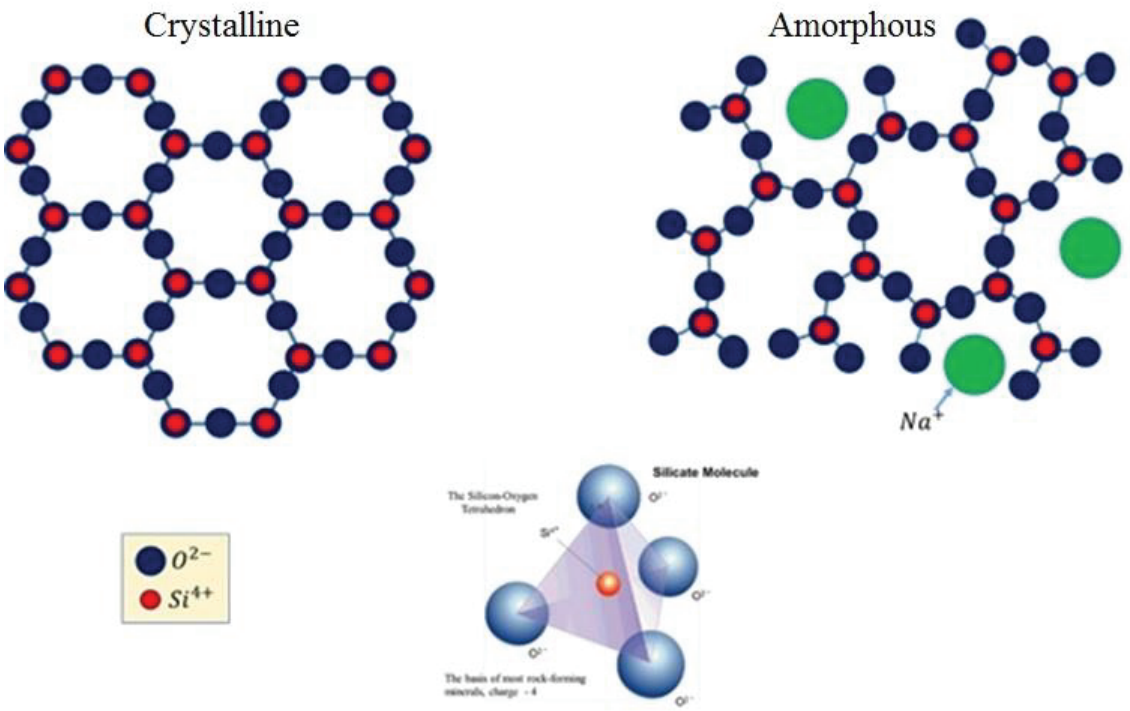

Figure 2.3. The crystalline and amorphous forms of silica and the silicon-oxygen tetrahedron.

Classification silica is shown in Figure 2.4. The crystalline silica has three forms: quartz, cristobalite and tridymite (Figure 2.5). Quartz is abundant in most soils and rocks and also found in sand [29], mortar [30], abrasives [31], concrete [32], construction aggregate [33], paints, fluxes, porcelain and brick [34]. The quartz-including dust can also be generated in any process of construction, mining [35], farming and disturbance of silica-including products such as the use of sand and other silica-containing products (e.g., foundry processes) [36] or masonry and concrete. Therefore, a variety of jobs and industries could expose people to quartz dust. Cristobalite and tridymite are found in soils and volcanic rocks [37-39]. Some industrial processes can also manufacture these polymorphs. For example, cristobalite transformation occurs in foundry processes [40], calcining of diatomaceous earth [41], ceramics and brick manufacturing [42], and silicon carbide production [43]. Amorphous silica can also change into cristobalite when waste or agricultural products, like rice hulls, are burned [44].

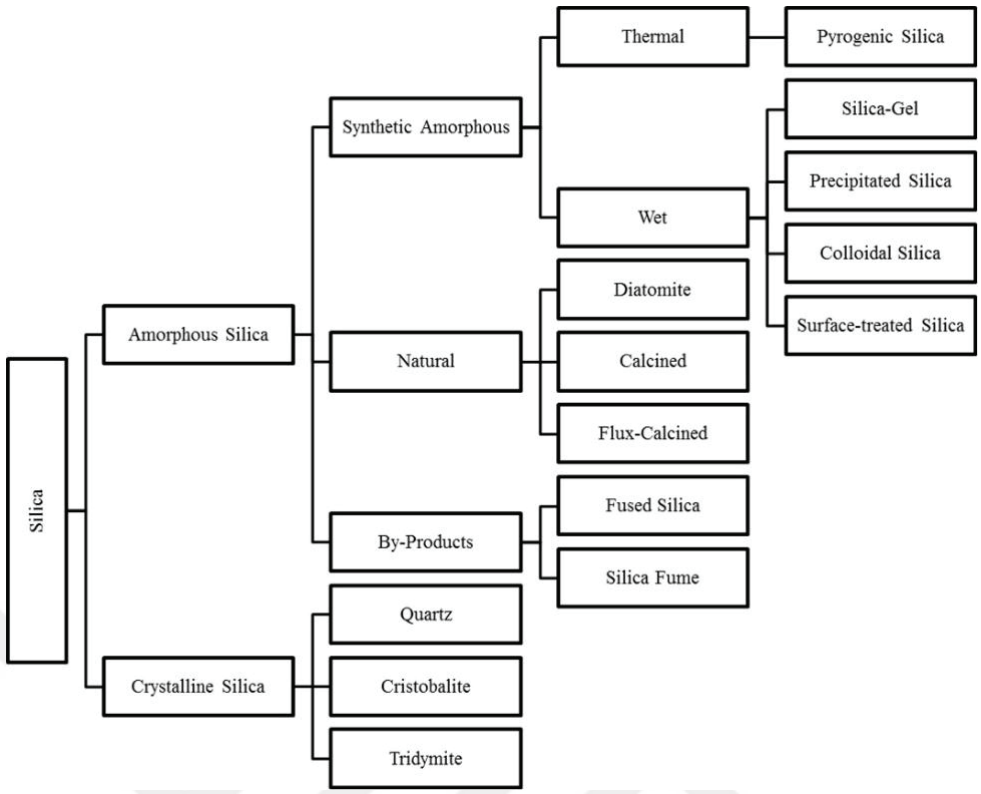

Figure 2.4. The various forms of silica (modified [45]).

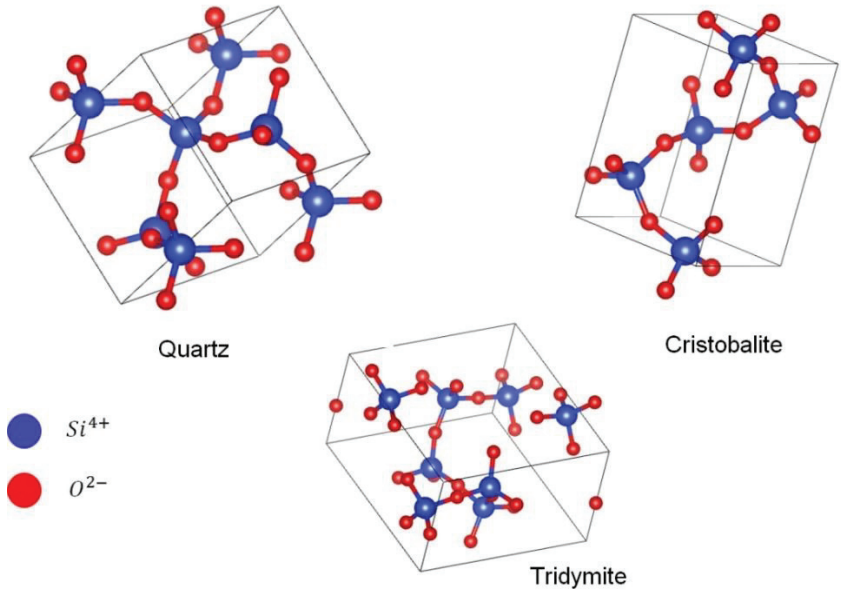

Figure 2.5. The crystalline silica has three crystal forms: quartz, cristobalite and tridymite.

Nano-silica has also become the most widely used material in many industries. Among these, the rubber industry which manufactures many products uses silica as a filler [46, 47]. The silica inclusion enhances the mechanical strength, shrinkage heat-resistance and thermal expansion [48]. The silica-based nanocomposites have many notable properties that allow their applications in electronics, automotive, marine, and other industries [45, 49, 50]. Currently, nano-silica is synthesized by chemical reactions, for example by the sol-gel method. A sol is mainly a dispersion of colloidal particles (1–100 nm) in a liquid. The gel is a connected rigid network with pores of sub-micron dimensions and polymeric chains [51]. The sol-gel method includes four stages namely hydrolysis, condensation, growth and aggregation (Figure 2.6). Colloidal silica (silica sol) nanoparticles were synthesized through the hydrolysis of tetraethoxysilane with ammonia and hydrochloric acid, followed by condensation and polymerization [52]. Particle size of silica sols synthesized in the presence of ammonia vs. the ratio of initial reactants are tabulated in Table 2.2 and transmission electron microscopy (TEM) images of silica sol samples nos. 1 (a), 2 (b), and 3 (c) synthesized at various ratios of the catalyst and initial reactants are demonstrated in Figure 2.7.

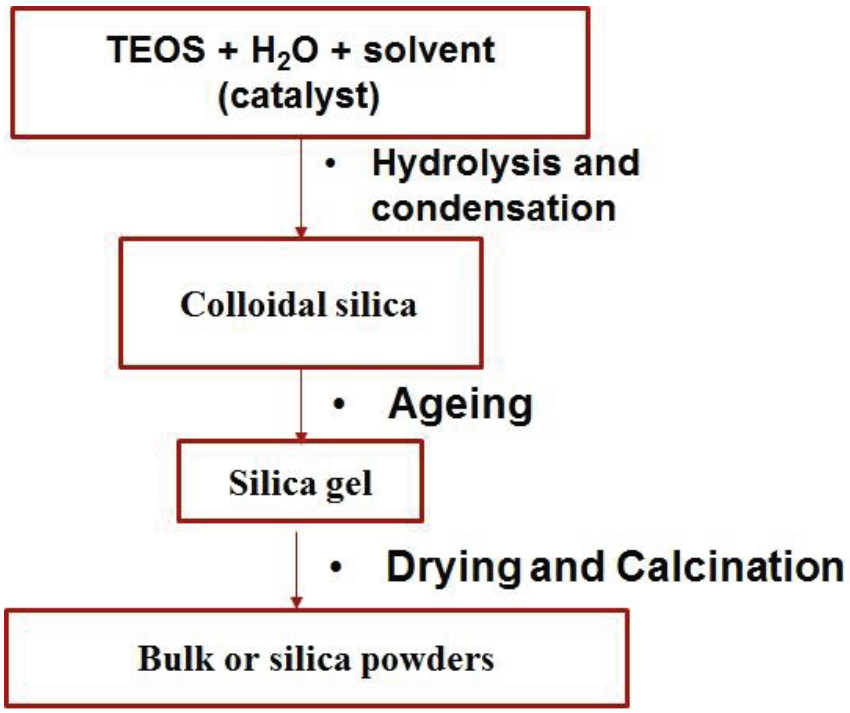

Figure 2.6. Flow chart of a typical sol-gel process.

Table 2.2. Particle size of colloidal silica (silica sol) synthesized in the various amounts of the initial reactants.

Material	Temperature (°C)	Amount (mol)				Particle size (nm)
		Water	TEOS	Ammonia	Ethanol	
1	70	21.6	1	2	57	25-30
2	70	4.8	1	0.6	33	16-20
3	70	15	1	0.2	33	12-14

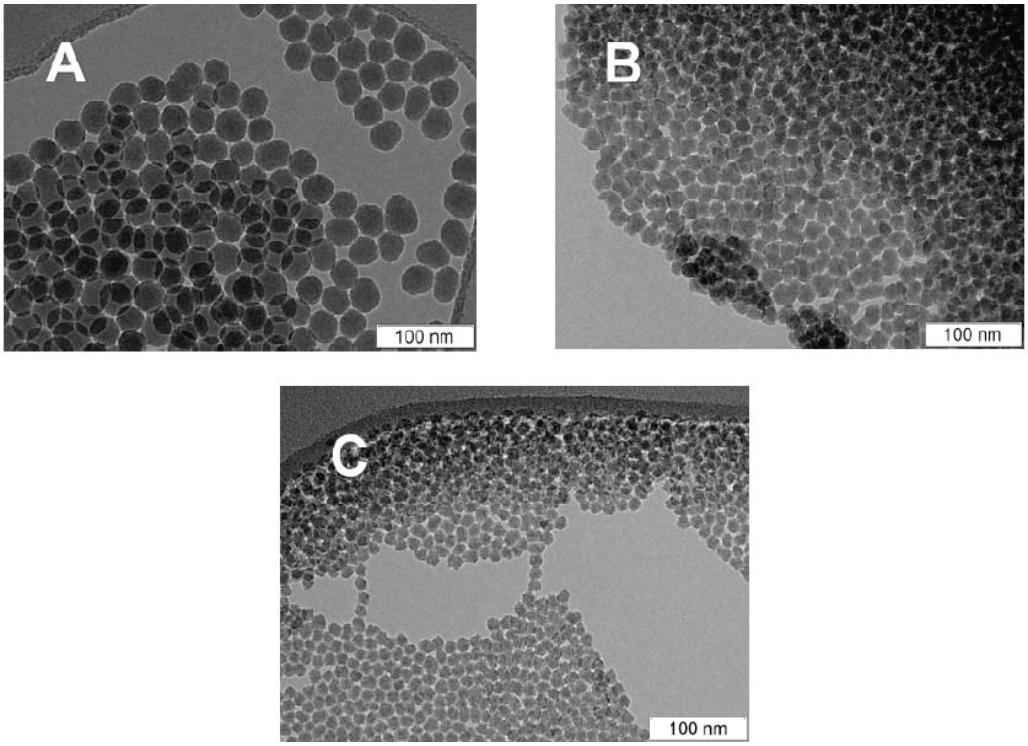

Figure 2.7. TEM micrographs of silica sol models 1 (a), 2 (b) and 3 (c) produced at various amounts of the initial reactants [52].

Combining nano-silica with other reinforcements also increases the mechanical properties of rubber [53-55]. Especially, high-quality silica holds the absolute advantage medical rubber (boots, gloves, etc.) or the fabrication of household products (fashion footwear soles, rubber mattresses, etc.). In the pharmaceutical industry, silica is utilized as a transporter for some proprietary medicines [56-58]. Silica also behaves as a catalyst in some organic reactions [59-61]; it increases the reaction's yield and speeds up its rate. To

meet the inclining demand for silica for industrial applications, researches have been focused on the manufacture of silica from different sources [62-65].

2.2. The Mechanical Properties of Nano-Silica Filled Polymeric Composites

Nano-silica reinforced polymer matrices are among the most widely studied composites as they have applications in many different types of products, especially in the electronics, automotive and aerospace industries [66]. The mechanical properties of silica nanoparticles added into epoxy, styrene-butadiene and natural rubber matrices are reviewed in the following section.

2.2.1. Silica Modified Epoxy Composites

Epoxy resins are the thermosetting materials that have been widely chosen in the engineering applications due to their excellent mechanical, thermal and electrical features [67, 68]. Most common group of epoxy resins are classified as bisphenol-A, bisphenol-F, cycloaliphatic, trifunctional, tetrafunctional, novolac, bio-based, fluorine-containing, phosphorus-containing, and silicon-containing epoxy resins (Figure 2.8) [69]. The very first synthesis of epoxy resin was practiced in the US in the late of 1930s by the reaction of bisphenol-A and epichlorohydrin which is shown in Figure 2.9. Epoxies are usually cured to have a high thermal stability and glass transition temperature (Tg). Epoxies generally outperform polyesters and vinyl esters in terms of strength and have less shrinkage during the curing process. Over the past decade, there have been intensive investigations on the improvement of epoxy nanocomposites with the inclusion of various types of nano-size fillers [4, 70-72]. Among these epoxy nanocomposites, nano (1–100 nm) silica filled epoxy composites have been widely investigated up-to-date applications in coatings [73], adhesives [74], construction, functional coatings, packaging materials for electronic devices [75], aerospace [76] and automotive industries [77-80].

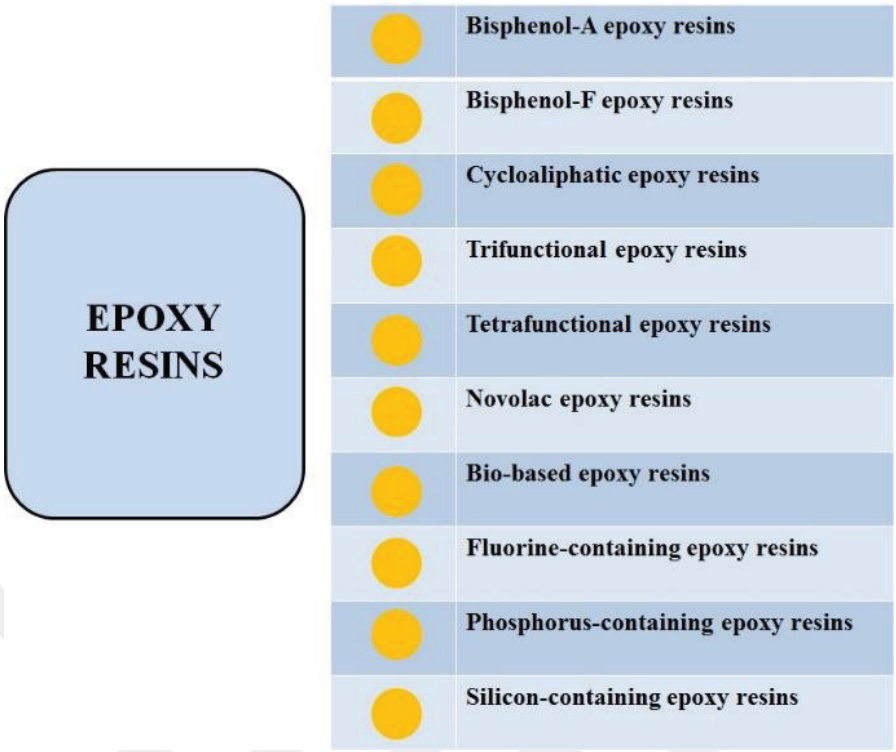

Figure 2.8. Most common group of epoxy resins.

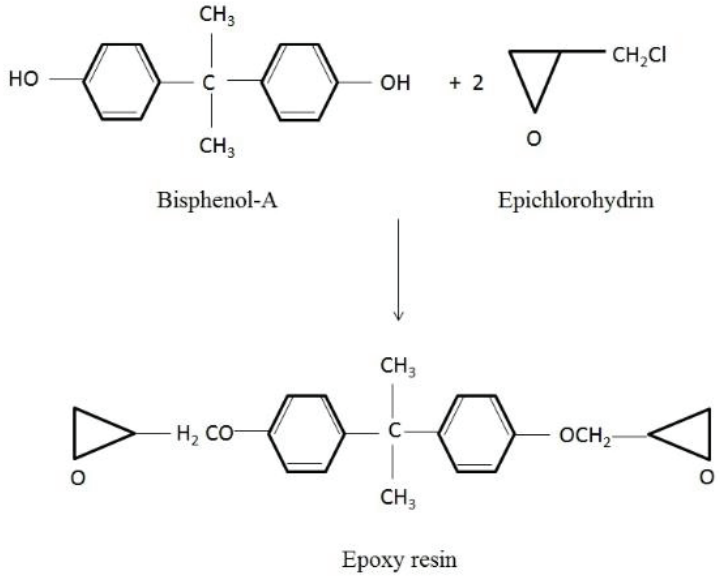

Figure 2.9. Synthesis of epoxy resin (modified [69]).

The preparation steps of an epoxy/nanocomposite are shown in Figure 2.10 [81]. First, nanoparticles are stirred with a probe homogenizer using acetone. The mixture is then swirled in a cool ice container while epoxy glue is added. The mixed solution is held in a vacuum chamber to remove acetone. The determined amount of curing agent is added and the solution is stirred again. At this stage, the gas bubbles are removed from the solution. The samples are then held in a vacuum at room temperature. Epoxy nanocomposites are cured after being poured into a mold.

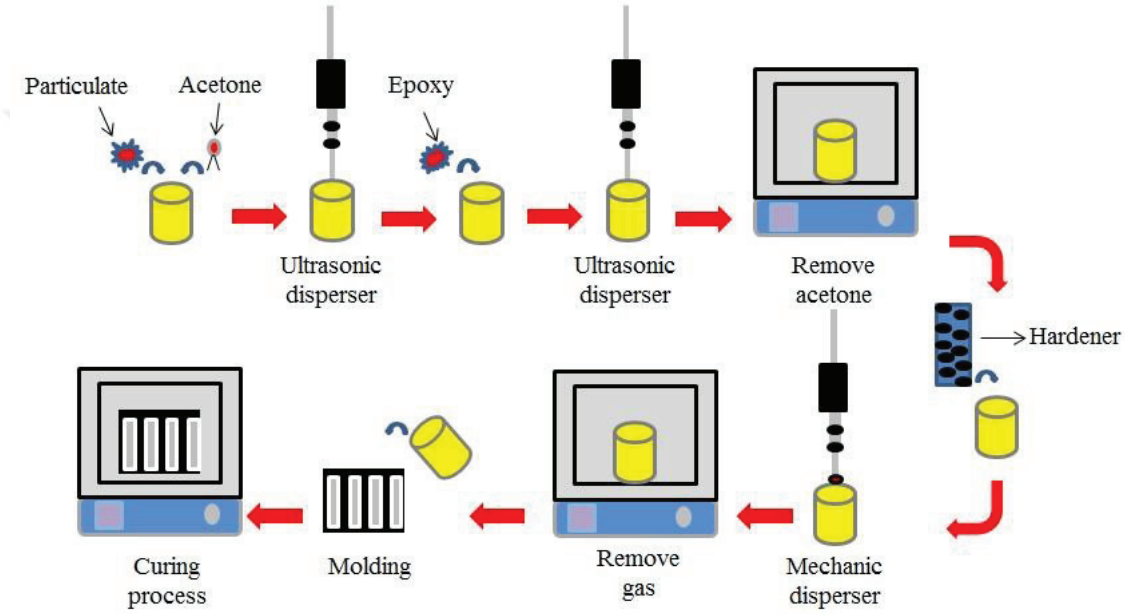

Figure 2.10. Schematic representation of the preparation steps of epoxy/nanocomposite samples (modified [81]).

The thermo-mechanical and wear behavior of surface-treated pineapple woven fibre and nano-silica dispersed mahua oil toughened epoxy composite were investigated in another study [82]. The epoxy thermoset resin used in this study was a liquid diglycidyl ether of bisphenol-A type epoxy resin. The additions of 3.4 and 6.8 wt% of nano-silica particles to epoxy resin increased the tensile strength from 65 MPa to 142 and 160 MPa, respectively. In another study, the effect of surface-functionalized crystalline nano-silica addition on the mechanical, fatigue and drop load impact damage behavior of an E-glass fibre-reinforced epoxy resin were investigated [83]. A TEM image of the surface-functionalized crystalline 20 nm nano-silica particles is shown in Figure 2.11. The highest

tensile strength and modulus of the composite investigated in this study were reported 135 MPa and 5.56 GPa, respectively.

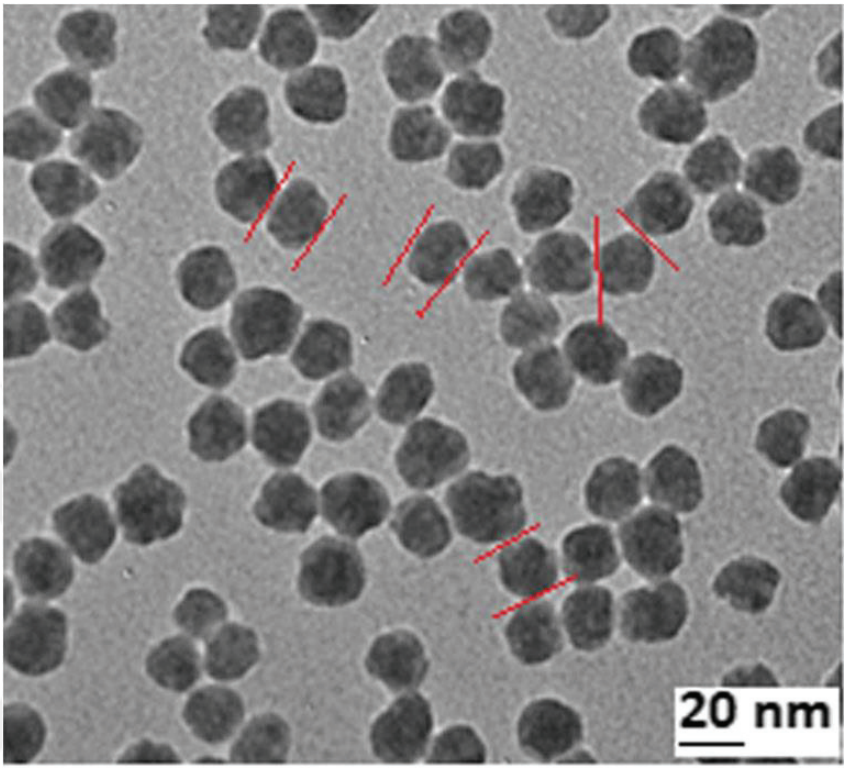

Figure 2.11. TEM images of silica nanoparticles [83].

The physico-mechanical properties of nano-silica filled epoxy-based mono and hybrid composites were examined [84]. The studied epoxy was filled with 0.5, 1.0, 1.5, 3, and 5 wt% nano-silica particle and the carbon fabric-reinforced epoxy composite was filled with 1.5 and 3 wt% of nano-silica. Figure 2.12 displays a schematic of the procedure that was employed. The highest increment in the tensile strength and modules was reported with 3 wt% of silica addition, with a tensile strength of 66.45 MPa and an elastic modulus of 3.12 GPa (tensile strength and modulus of matrix were 50.52 MPa and 2.82 GPa, respectively). The strength and modulus of carbon fabric-reinforced epoxy composite increased sequentially by 13.87% and 16.69% by the addition of 3.0 wt% silica.

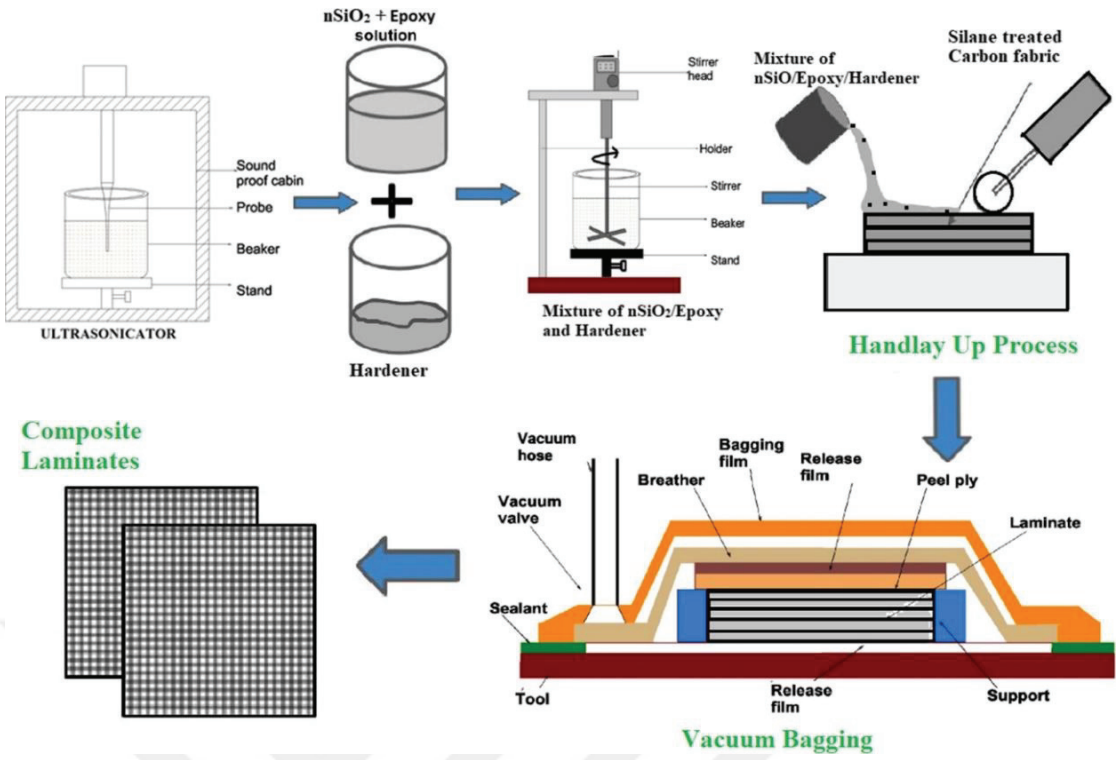

Figure 2.12. Detailed scheme for the fabrication of the carbon fabric-reinforced epoxy hybrid composites [84].

The effect of silica aerogel nanoparticle addition on the vibrational, mechanical, and morphological features of an epoxy was investigated [85]. Neat epoxy was prepared with 1, 2, and 4 wt% of silica aerogel nanoparticles. The tensile stress–strain curves of epoxy-based nanocomposites and neat epoxy are shown in Figure 2.13. The tensile strength and modulus of the neat epoxy were sequentially 45.4 MPa and 2.36 GPa. The addition of 1 wt% silica aerogel nanoparticles reduced the elastic modulus and ultimate tensile strength of the resin, while the elastic modulus increased when the silica aerogel nanoparticle content was increased to 2 and 4 wt%. The tensile strength was higher than that of neat epoxy when the silica aerogel nanoparticle content was 4%.

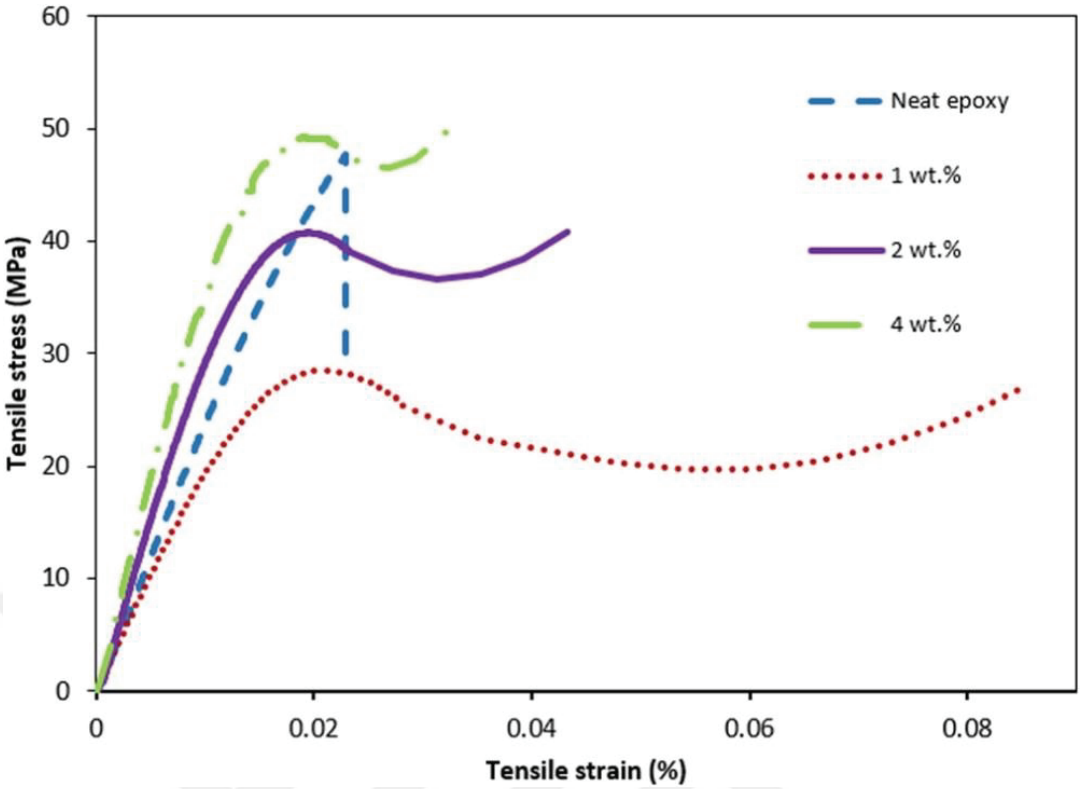

Figure 2.13. Tensile stress–strain curves silica filled epoxy composites [85].

In a separate study, the epoxy resin of a E-glass fiber reinforced composite were prepared with the surface functionalized crystalline nano-silica particles [86]. The polymerization method for uniform dispersion of nano-silica in the epoxy matrix in this study is shown in Figure 2.14. Nano-silica inclusion to the glass fiber composite increased the tensile strength and modulus up to 3 wt%. The addition of 2, 3, 4 and 5 wt% of nano-silica particle increased the tensile strength to 150.16, 156.2, 138.51 and 131.44 MPa, respectively (the tensile strength and modulus of the neat epoxy were 107.44 MPa and 9 GPa, respectively). The highest modulus was 10.06 GPa.

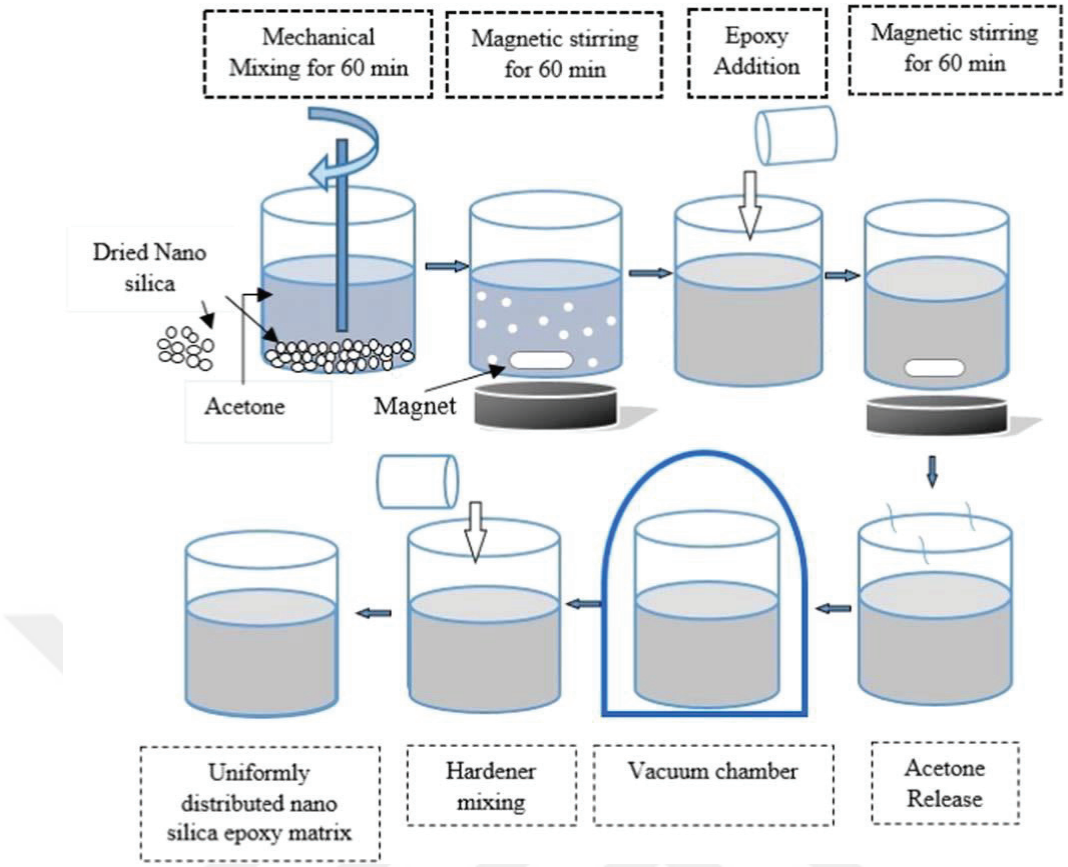

Figure 2.14. Schematic of homogeneous distribution of silica nanoparticles in epoxy matrix [86].

The mechanical and low velocity impact behavior of intra-ply glass/kevlar fibre reinforced micro-rubber and nano-silica (Figure 2.15) modified epoxy resin hybrid composites were examined [87]. The tensile strength increased from 65 MPa to 190 MPa with 11 wt% nano-silica addition. Additions of micro rubber (9 wt%) along with nano-silica (11 wt%) into intra-ply glass/kevlar-reinforced epoxy composite further increased the tensile strength, modulus and fracture toughness.

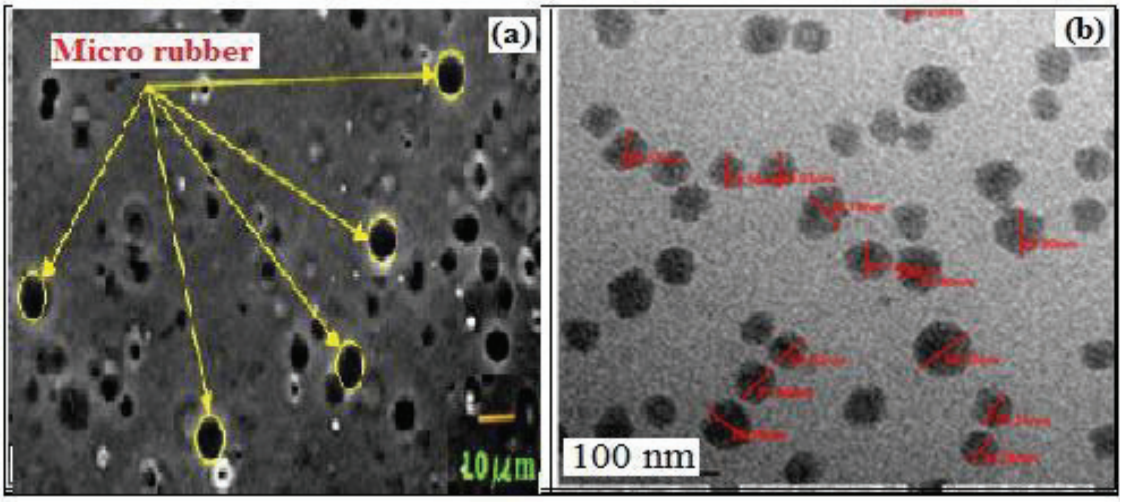

Figure 2.15. TEM images of dispersed (a) micro-rubber and (b) nano-silica in epoxy matrix [87].

The mechanical properties of nano-silica on a ramie/epoxy composite including tensile, flexural, and interfacial strength were characterized [88]. There was a distinct improvement in the mechanical properties of the composites after the addition of nano-silica. This improvement gradually increased as the concentration of nano-silica increased.

The strain-rate-dependent mechanical behavior of a photopolymer matrix composite with fumed nano-silica filler was investigated [89]. The main objective was to determine the rate dependency of the material. Results showed that fumed silica addition improved the mechanical properties of photopolymer matrix composite. Figures 2.16(a-c) display the stress–strain curves of 4, 8, 9, and 10% nano-silica filled composite at 1.3 $\times 10^{-2}$, 1.3 $\times 10^{-3}$ and 1.3 $\times 10^{-4}$ s^{-1} strain rates, respectively. The tensile strength of 4, 8, 9 and 10 wt% silica added composite was 15, 17, 18 and 16 MPa at a strain rate of 1.3x10^{-2} s^{-1}.

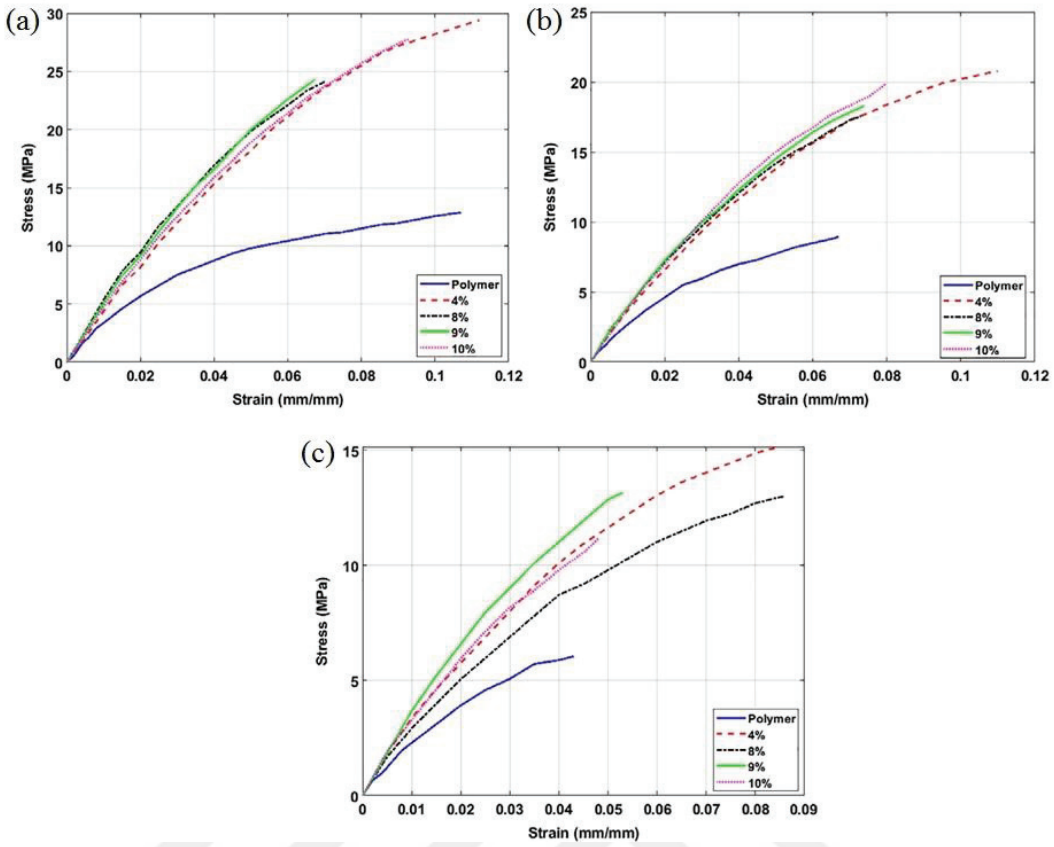

Figure 2.16. Stress–strain curves of polymer, 4, 8, 9, and 10% nano-silica filler concentration at strain rate: (a) 1.3×10^{-2} s^{-1}, (b) 1.3×10^{-3} s^{-1}, and (c) 1.3×10^{-4} s^{-1} [89].

The reinforced mechanisms and mechanical properties of hyperbranched polyesters functionalized silica epoxy composites were studied [90]. In order to introduce amino reactive groups as the growth points, 3-aminopropyltriethoxysilane (APTES) was used to create the nano-silica for grafting and coating of hyperbranched polyesters (HBP). By using solution casting, hyperbranched polyesters functionalized nano-silica reinforced epoxy composites (HBP-APTES-SiO_2/EP) were prepared (Figure 2.17). The tensile strength, microhardness and fracture toughness were determined and the reinforced mechanisms of HBP-APTES-SiO_2 were examined. This study revealed that both of the un-treated nano-silica reinforced EP (U-SiO_2) and HBP-APTES-SiO_2 increased the tensile strength and modulus of the epoxy composites, in particular, the HBP-APTES-SiO_2/EP composites demonstrated more outstanding mechanical features. For example, when the content of HBP-APTES-SiO_2 was 2 phr (1.96 wt%), the modulus and tensile

strength of the HBP-APTES-SiO_2/EP composites reached the maximum values, which were increased by 42.64% and 16.61% than those of the epoxy.

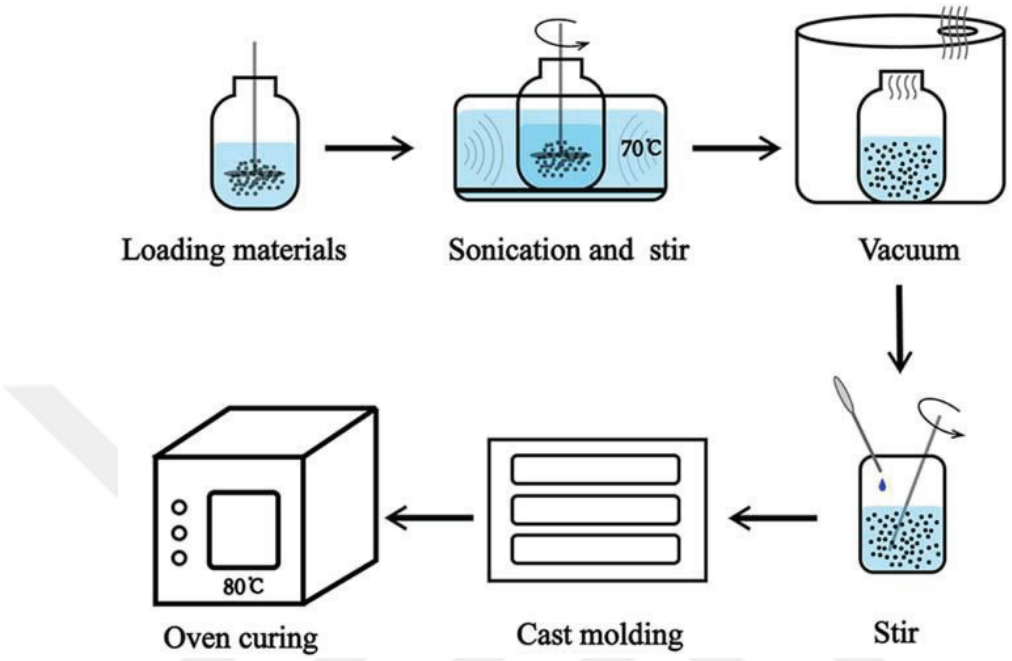

Figure 2.17. The steps in preparation of APTES-SiO_2/EP composites [90].

In another study, six silica aerogel epoxy composites were fabricated with different silica aerogel contents [91]. The brittle mechanism of epoxy was altered to a ductile mechanism by the silica aerogel addition. The yield strength further increased with increasing the silica aerogel content. At lower filler loadings, the silica aerogel particles acted as a plasticizer. Due to the plasticizing effect of the silica aerogel particles, the sample containing 1 wt% had the highest strain at break and toughness and the lowest ultimate tensile strength and elastic modulus. An increment of the filler content to 2 and 3 wt% led to increases in the yield stress, ultimate tensile strength, and elastic modulus.

The fracture toughness and mechanical properties of an epoxy resin with nano-silica additions were studied [92]. The nano-silica was prepared from rice husk by applying a thermal treatment method, having a particle size ranging 40–80 nm. The tensile strength of the neat epoxy, 38 MPa, increased to 39, 40, 41 and 42 MPa with the additions of 0.3, 0.5, 0.7 and 1 wt% nano-silica, respectively. While, the fracture strain was reduced with the nano-silica addition by 29.3%.

A series of polyethylene glycol (PEG) epoxy-based electrolytes filled with 2.5-10 wt% nano-silica were prepared [93]. It was shown that increasing nano-silica content increased the ionic conductivity, reduced glass transition temperature and decreased the strength and modulus. The tensile strength and modulus of the neat epoxy were sequentially 4 MPa and 5.5 GPa. The tensile strengths of nano-silica added composite were however reduced to 3, 2.25, 2 and 1.75 MPa, with the additions of 2.5, 5, 7.5 and 10 wt% of nano silica, respectively.

Silica/epoxy nanocomposites with two different loading, 3 and 5 wt%, were prepared in order to investigate the erosion-wear, mechanical and thermal properties [94]. The tensile strength and modulus of the neat epoxy were 40 MPa and 0.87 GPa, respectively. The tensile strength increased from 40 to 43 MPa with 3 wt% silica addition; but the strength was reduced to 12 MPa with the addition of 5 wt% nano-silica. The plasticizing effect of 3 wt% nano-silica powder addition was confirmed. The composite having 3 wt% of silica had a higher strength and fracture strain than the neat epoxy resin.

The effect of 5-15 nm silica nanopowder and functionalized fumed silica additions on the mechanical properties of epoxy-based nanocomposites was investigated [95]. The elastic modulus and tensile strength of nanocomposites are tabulated in Table 2.3 and Table 2.4 sequentially for silica nanopowder and fume silica additions. Although both powders increased the elastic modulus of the neat epoxy, the fume silica reduced the tensile strength, while nano-silica powder had the opposite effect. The poor nano filler dispersion associated with the lack of chemical compatibility between the powder and the resin was found for fume silica.

Table 2.3. Mechanical properties of nanocomposites of silica nano powder [95].

M1	Weight percentage (wt%)	Longitudinal modulus of elasticity (MPa)	Ultimate strength (MPa)
Pure epoxy	0	3471	71.37
		3116	77.07
Nano-silica	0.3	3526	83.02
	1	3633	85.74
	3	3438	85.02

Table 2.4. Mechanical properties of nanocomposites of fume silica [95].

M2	Weight percentage (wt%)	Longitudinal modulus of elasticity (MPa)	Ultimate strength (MPa)
Pure epoxy	0	3910	90.00
		4815	103.98
Nano-silica	0.1	3910	82.86
	0.3	3215	77.38
	0.5	4230	57.95

The mechanical properties of 0.5, 1.0, 1.5, 2.0 and 3.5 wt% silica nanoparticle reinforced epoxy/nanocomposites were investigated [81]. While 1 wt% silica nanoparticle added specimens had better strength than neat epoxy resin with an increment at 37.10%, there was a linear reduction of the strength as the reinforcement content was increased and lowest values were determined at 3.5 wt% silica addition with a reduction of 7.18% (Table 2.5). The increased amount of nanoparticles caused the agglomeration of nanoparticles, reducing the strength.

Table 2.5. Mechanical properties of silica nanoparticle reinforced epoxy nanocomposites.

Nano silica (wt%)	Tensile strength (MPa)	Variation of tensile strength (%)	Elastic modulus (GPa)	Variation of elastic modulus (%)	Toughness (MPa)	Variation of toughness (%)
0	58.65	-	2.60	-	1.09	-
0.5	78.87	34.48	1.90	-27.09	3.95	262.39
1	80.41	37.10	2.71	4.12	3.62	232.11
1.5	74.13	26.39	2.35	-9.43	5.51	405.50
2	64.22	9.50	2.35	-9.54	2.95	170.64
3.5	54.44	-7.18	1.76	-32.24	2.56	134.86

The effect of 17 and 65 nm silica nanoparticle addition on the modulus, yield strength and energy absorption capability of thin-walled square epoxy columns was investigated [96]. Nano-silica particles were dispersed almost homogeneously in the epoxy resin. The powder content ranged 1.5-6 wt%. The first and second series of the composites were reinforced with 17 nm and 65 nm size particles, respectively and the third series were reinforced with the combination of both particle sizes. The tensile strength and

modulus of neat epoxy were 20.3 MPa and 1.521 GPa, respectively. By adding silica nanoparticles, the modulus increased in both unimodal particle size and bimodal particle size composites. Also, the optimized mixture proportions of epoxy-based hybrid nanocomposite with different compositions of nano-silica as nano reinforcement, high impact polystyrene (HIPS) as the thermoplastic phase and hardener were determined [100].

AFM substantiation of the fracture behavior and mechanical properties of sol–gel derived silica packed epoxy networks were studied [97]. The main objective was to examine the mechanical properties of silica packed epoxy networks produced by an in–situ, solvent–free, sol–gel process. A series of silica packed epoxy networks with different silica contents, 0, 5, 10, and 20 wt% were synthesized by pre–hydrolyzing TEOS in the liquid epoxy resin (DGEBA) using stoichiometric amounts of acidic water. The tensile strength of the neat epoxy was 19.9 MPa. The mechanical properties of epoxy networks expressively developed on silica packing. 10 wt% silica polymer displayed maximum increment in tensile strength (55%), modulus (101%) and toughness (20%). However, the tensile strength was reduced sharply above 10 wt% silica from 30.9 MPa to 10.6 MPa.

Thermal and mechanical evaluation of epoxy resin composites by synthesis of amine-based coupling agent nano-silica complex was examined [98]. Nano particulate fillers displayed an incremental influence on the stress–strain and thermal resistance behavior of epoxy (the tensile strength of the neat epoxy was 6 MPa). The additions of 0.3, 0.6, 0.9, 1.2, 1.5, 1.8 and 2.1 wt% of nano-silica were improved the tensile properties of epoxy composite. The tensile strength of 0.3, 0.6, 0.9, 1.2, 1.5, 1.8 and 2.1 wt% nano-silica was increased to 7-50 MPa with the addition of nano-silica (Figure 2.18).

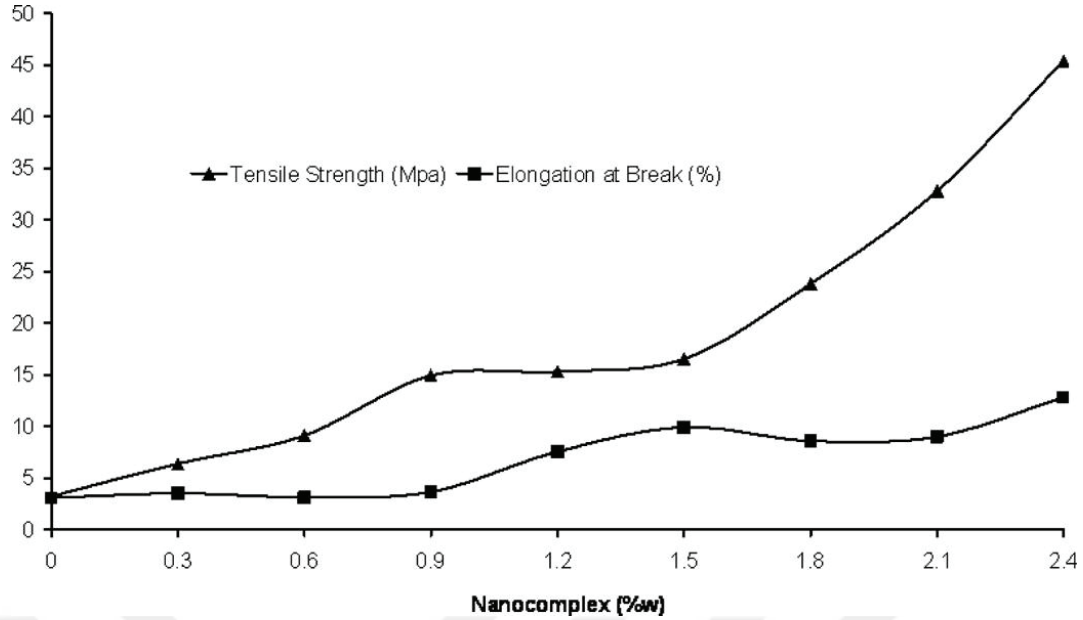

Figure 2.18. Tensile strength and elongation at break of prepared epoxy nanocomposites [98].

The Molecular Dynamics and Finite Element models were performed in order to predict the mechanical properties of a glass silica nanoparticle/epoxy composite [99]. The addition of 5 wt% of nano-silica was increased the tensile strength from 5 MPa to 12 MPa. The elastic moduli of silica/epoxy nanocomposites determined from molecular dynamics and finite element models method were found to be very much similar to those of experimental.

Figure 2.19 shows the effect of silica addition on the tensile strength of different types of epoxy-based composites. In general, the addition of nano silica increases the tensile strength. But, at higher concentrations of silica, the strengthening effect vanishes and the strength starts to decrease after a critical silica content, as seen in Figure 2.19. It is presumed that until about a critical content, silica nano particles are homogeneously mixed with epoxy matrix, and above, the agglomeration nanoparticles occur which decline the tensile properties. The maximum silica content is 10 wt% and the maximum tensile strength of silica epoxy composite is about 160 MPa. Also, high is the neat epoxy strength, high is the composite strength.

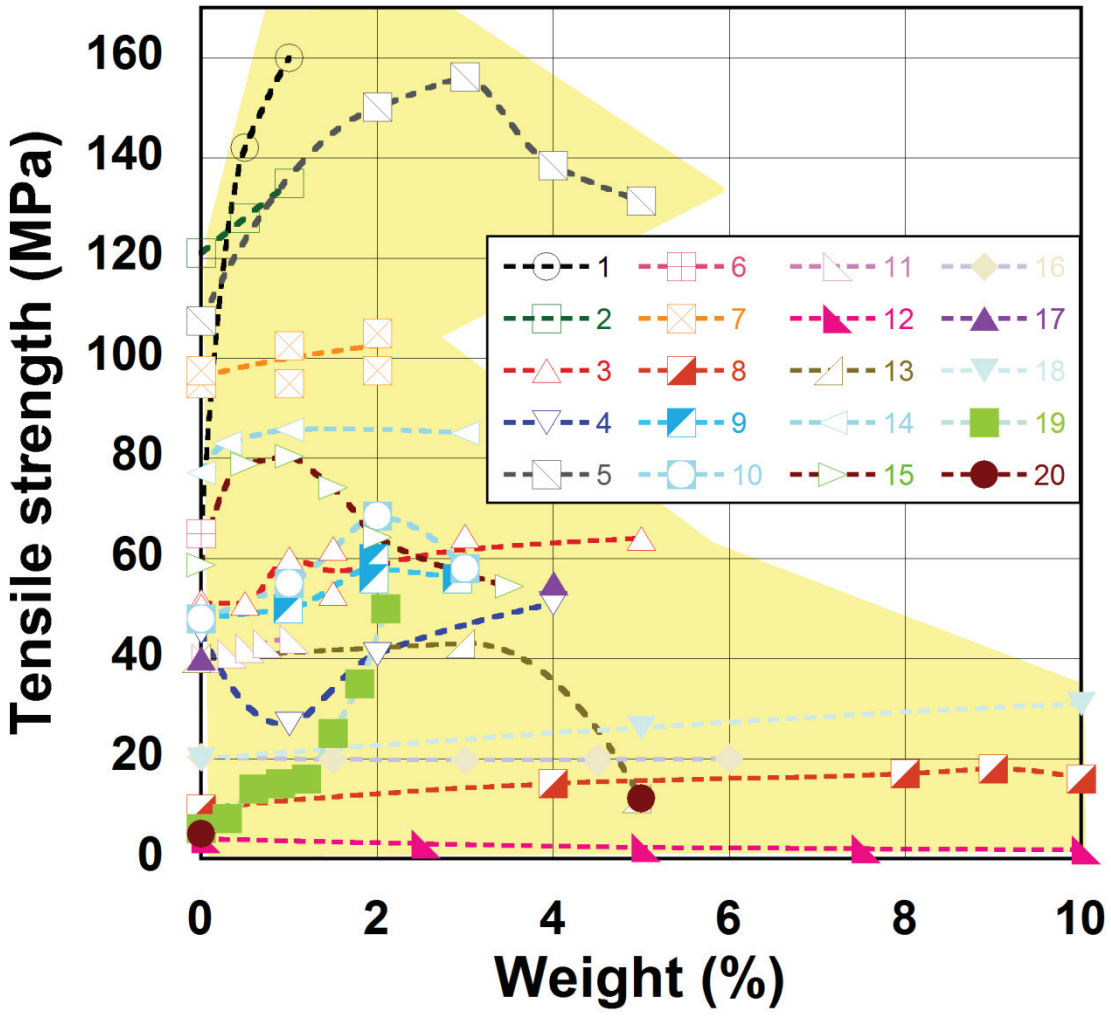

Figure 2.19. Tensile strength of silica modified epoxy composites 1 [82], 2 [83], 3 [84], 4 [85], 5 [86], 6 [87], 7 [88], 8 [89], 9 [90], 10 [91], 11 [92], 12 [93], 13 [94], 14 [95], 15 [81], 16 [96], 17 [100], 18 [97], 19 [98], 20 [99].

2.2.2. Silica Modified Styrene-Butadiene Rubber Composites

The elastomer industry's most extensively used synthetic rubber, styrene-butadiene rubber (SBR), is produced in the highest volume (Figure 2.20). It is a copolymer of butadiene (CH_2=CH-CH=CH_2) and styrene (C_6H_5CH=CH_2), generally containing 77% butadiene and 23% styrene. Although emulsion and solution polymerization can be used to create SBR, emulsion polymerization accounts for roughly 85–90% of global SBR production [101, 102]. SBR is synthesized from 1,3-butadiene and

styrene monomers via two ubiquitous synthetic pathways, by emulsion (ESBR) and solution (SSBR) processes as illustrated in Figure 2.21. The mechanical properties of SBR are improved by adding reinforcing fillers such as silica [103].

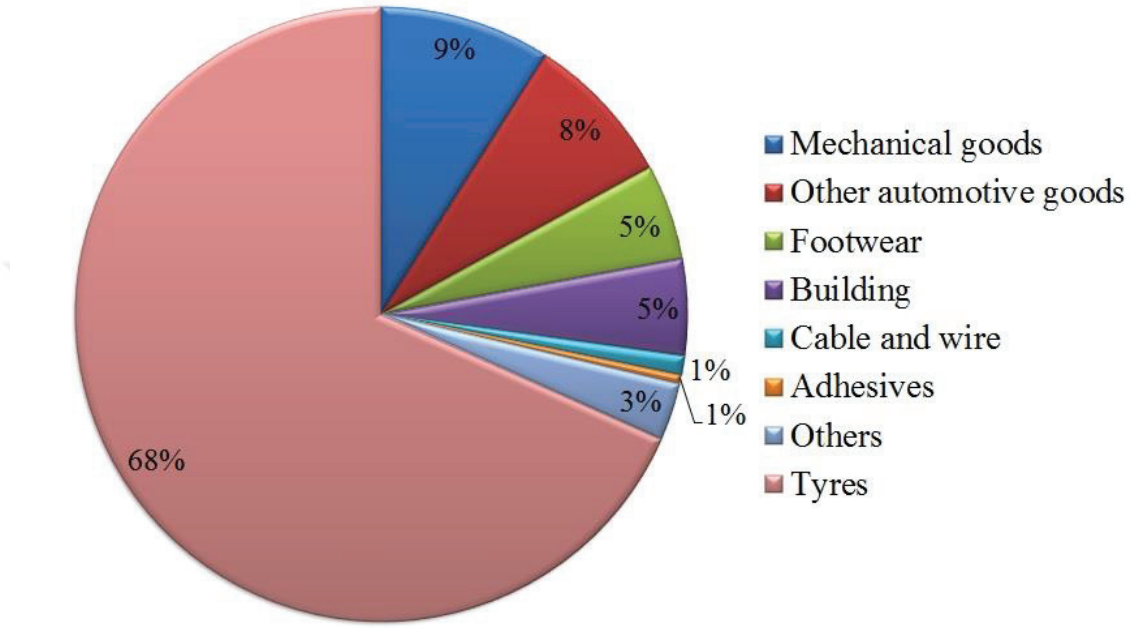

Figure 2.20. The main application of styrene-butadiene rubber (SBR) (modified [102]).

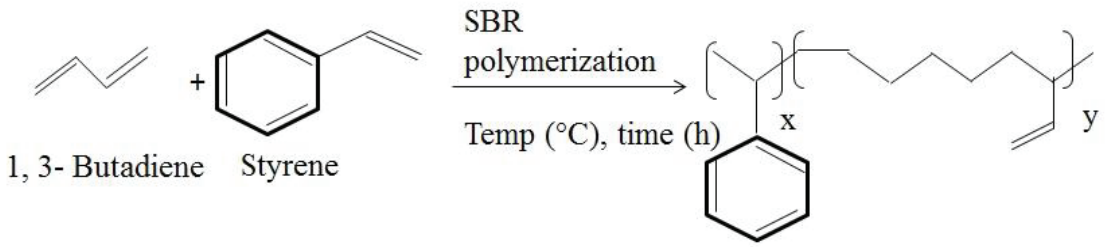

Figure 2.21. Synthesis of styrene–butadiene rubber (modified [102]).

The effects of co-silanized silica on the thermal and mechanical properties of NR/SBR blends were previously investigated [104]. The addition of 4 wt% silica increased the tensile strength of silica-NR/SBR and co- silica-NR/SBR blends from 18.93 MPa to 23.68 and 25.6 MPa, respectively.

The effect of styrene-butadiene rubber and fumed silica nano-filler on the mechanical properties and microstructure of glass fiber reinforced unsaturated polyester resins were examined [105]. The tensile strength and modulus of the neat SBR were 21 MPa and 0.34 GPa, respectively. The addition of 1.33 and 4 wt% of nano-silica particle was increased the tensile strength of SBR from 21 MPa to 25 to 27 MPa, respectively. The elastic modulus was increased from 0.34 GPa to 0.39 to 0.43 GPa with the addition of 1.33 and 4 wt% of nano-silica particles, respectively.

The effect of nano-silica surface-capped by bis[3(triethoxysilyl) propyl] tetrasulfide on the mechanical properties of SBR/BR nanocomposites were studied [106]. Neat SSBR/BR composites and four kinds of SSBR/BR/Si-Sx nanocomposites, denoted as neat SSBR/BR, SSBR/BR/Si-Sx-0-0, SSBR/BR/Si-Sx-0-6.5, SSBR/BR/Si-Sx-6.5-0, and SSBR/BR/Si-Sx-6.5-6.5 were prepared. The tensile strength of SSBR/BR was increased from 1.20 to 14.88 MPa in SSBR/BR/Si-Sx-6.5-0.

The mechanical, rheological, thermal and morphological properties of in-situ 20, 31.30 and 30.20 wt% silica filled butadiene rubber composites were investigated [107]. The tensile strength and modulus were increased from 0.97 MPa, to 1.49, 1.98 and 3.17 MPa, sequentially for 20, 31.30 and 30.20 wt% silica addition. For the same loading, the modulus increased to 0.98, 1.13 and 1.21 MPa, respectively.

A study focused on the treatment of the silica surface by silane coupling agents to promote the interaction with styrene-butadiene rubber [108]. Using potassium peroxydisulfate (KPS) as an initiator, vinyltriethoxysilane (VTES) was grafted onto styrene-butadiene rubber (SBR) in latex. After that, mechanical mixing was used to create SBR-g-VTES/silica, SBR/TESPT/silica, and SBR-g-VTES/TESPT/silica with varied silica loadings of 20.87, 25.85, and 30.17 wt%. Particle reinforced SBR-g-VTES was examined to see how VTES affected the cure characteristics, physical qualities, and dynamic mechanical properties. While the elongation at break of all samples showed a tendency in the opposite direction, all samples showed an increase in hardness and with increasing silica concentration. The SBR-gVTES/TESPT/silica composites showed the highest harness and tensile strength. The SBR-g-VTES/silica composites exhibited higher hardness and tensile strength than SBR/TESPT/silica.

The result of the above literature survey is summarized as a tensile strength versus weight percent of silica graph in Figure 2.22. As is seen clearly in the same figure, an increase in nano-silica content in the SBR matrix increases the tensile strength. The maximum silica content is about 32 wt% and the maximum tensile strength is about 27 MPa.

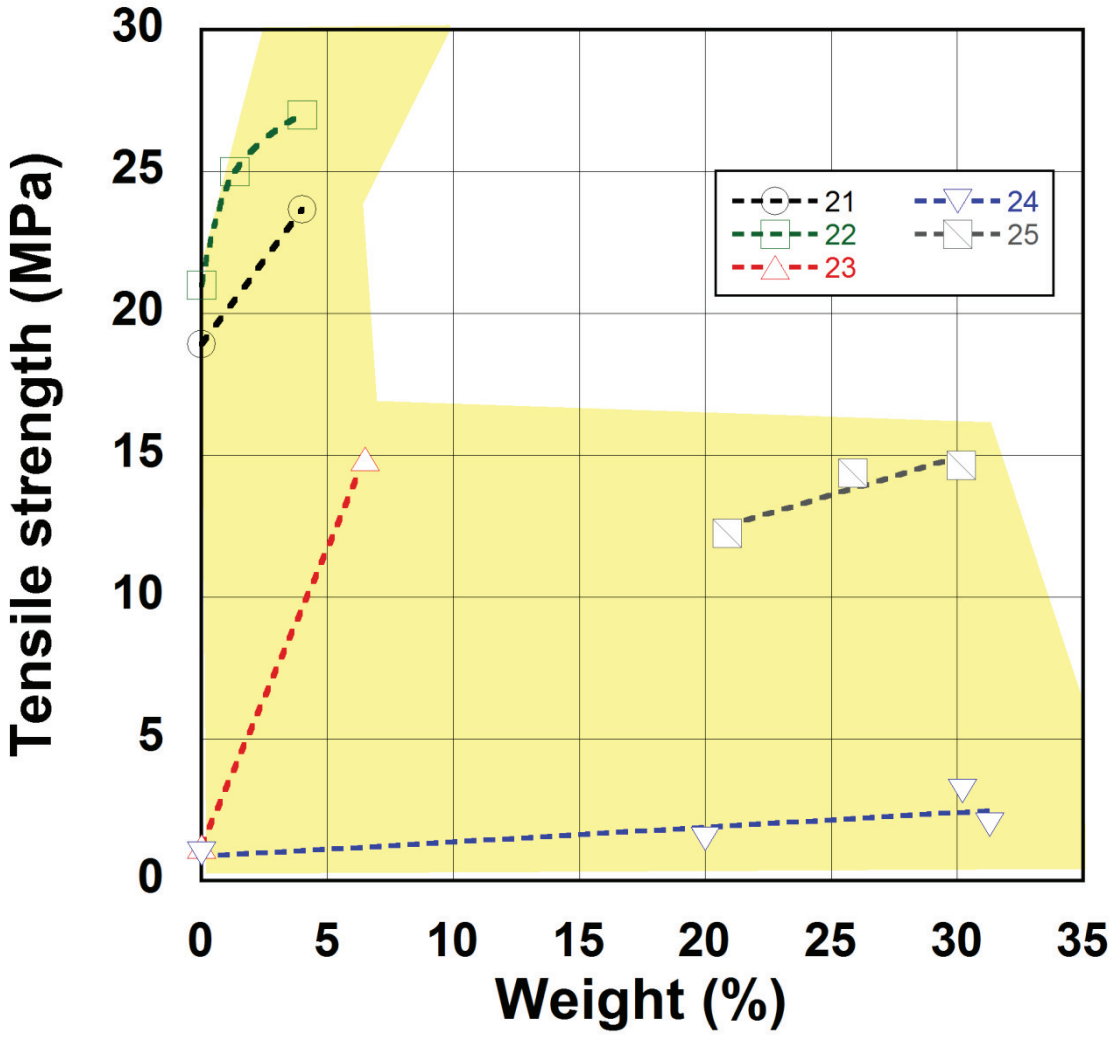

Figure 2.22. Tensile strength of silica modified styrene butadiene rubber composites 21 [104], 22 [105], 23 [106], 24 [107], 25 [108].

2.2.3. Silica Modified Natural Rubber Composites

Natural and synthetic rubbers are utilized in numerous industrial products (Figure 2.23). Natural rubber has outstanding tensile and tear strength and good abrasion resistance [109] and therefore it is suitable for the production of o-rings, seals, tires, conveyor belts, and so on. By adding fillers to achieve desired properties for individual products, the use of natural rubber in everyday products is continuously expanding [110]. One of the most popular fillers in the rubber industry is silica [111-113]. Additional advantages and compounding flexibility can be obtained by filling silica [114-116].

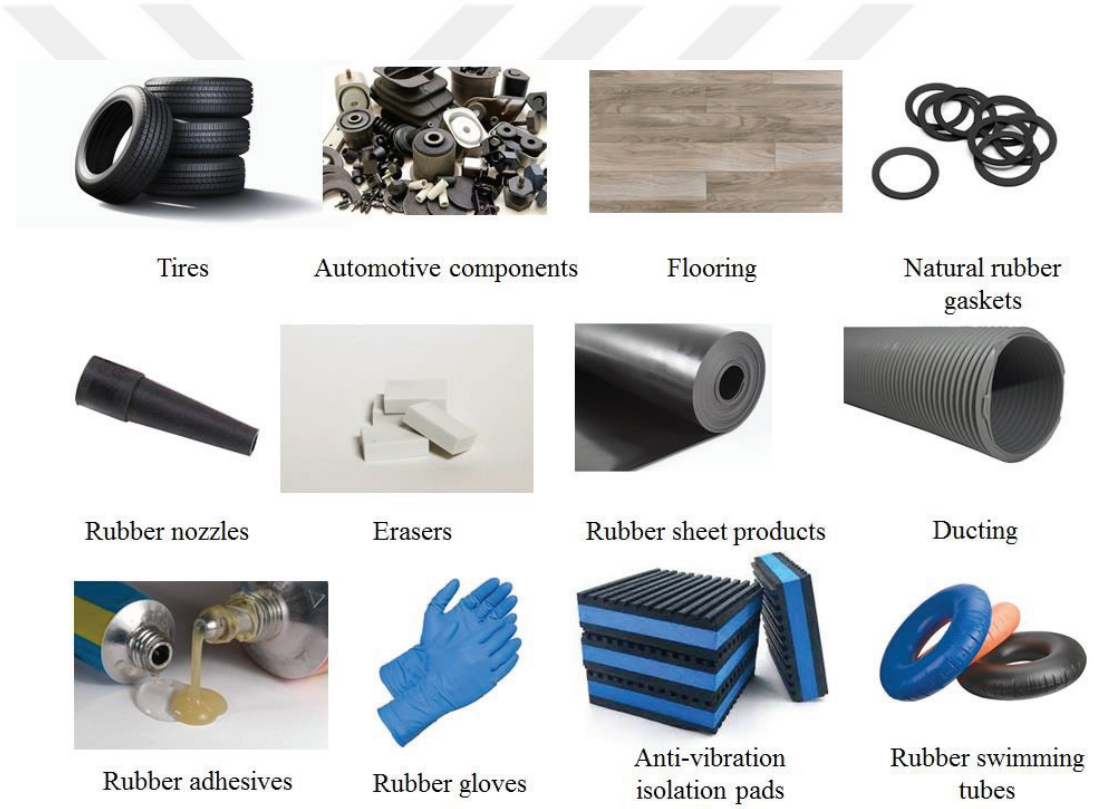

Figure 2.23. Industrial rubber products.

The NR nanocomposites were manufactured by filling ionic liquid 1-allyl-3-methyl-imidazolium chloride (AMI) modified nano-silica in NR matrix through mechanical mixing and a following curing process [117]. The bound rubber, vulcanization characteristics, mechanical properties, and dynamic mechanical properties of the

modified nano-silica /NR nanocomposites with various morphologies and network structures were systematically examined. The tensile strength and modulus of the neat NR were 17.79 MPa and 0.85 MPa, respectively. AMI-modified nano-silica greatly increased the tensile strength of nano-silica/NR nanocomposites. When unmodified nano-silica/NR nanocomposite was compared to AMI-modified nanosilica /NR nanocomposite, the tensile strength was improved by 102%. The additions of 0.68, 1.35 and 2.02 wt% of AMI-modified nano-silica developed the tensile properties. The tensile strength of 0.68, 1.35 and 2.02 wt% AMI-modified nano-silica was 23.95, 22.52 and 15.99 MPa and the young modulus of 0.68, 1.35 and 2.02 wt% AMI-modified nano-silica was 1.18, 1, 0.89 MPa, respectively.

Quaternized polyvinyl alcohol (QPVA) was manufactured and utilized as an intermedium to develop dispersion of silica in NR. QPVA/silica nanoclusters reinforced NR nanocomposite was prepared by latex compounding via electrostatic interaction (Figure 2.24) [118]. For silica modified NR films, the tensile strength reduced dramatically when the silica content was more than 2 wt%. The maximum tensile strength of NR-QPVA/SiO_2 films was 34.2 MPa at 3 wt% SiO_2 loading, which was increased by 60% as compared with that of neat NR film.

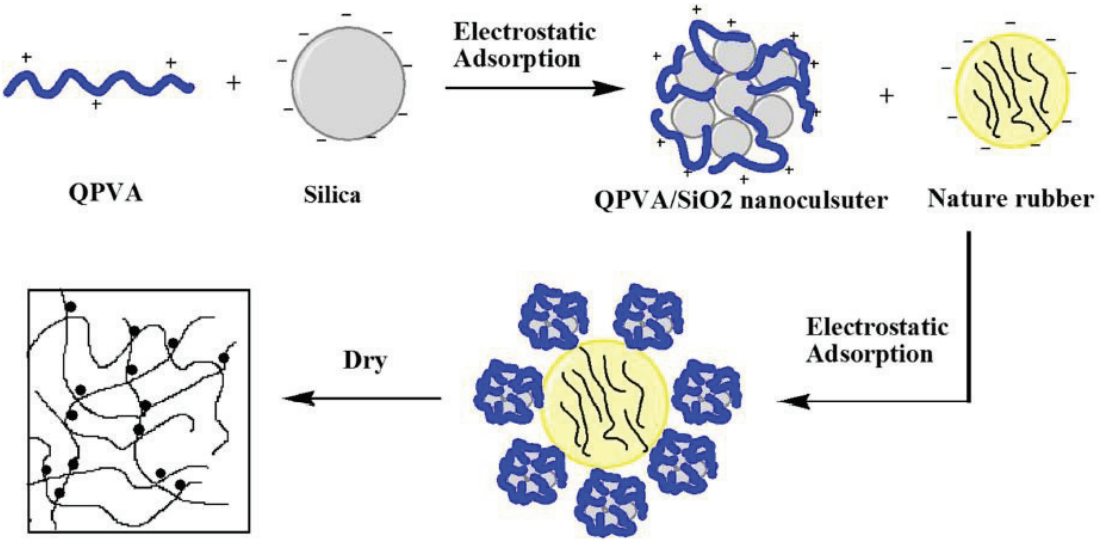

Figure 2.24. The mechanism of preparing NR-QPVA/SiO_2 nanocomposite [118].

The mechanical properties of NR, SBR and NR/SBR blends filled with silica hybrid filler, and their abrasive wear behavior against various counterface materials were examined [119]. The addition of 3.66, 7.06 and 10.22 wt% of nano-silica particle increased the tensile strength to 8.97, 10.83, and 10.37 MPa, respectively. The highest modulus was 1.51 MPa.

Natural rubber compound utilizing various silica, containing admicellar modified silica, unmodified silica and silica with a silane coupling agent, were investigated [120]. The strength and modulus features of both admicellar silica and silica with silane coupling agent did not change so much, but they were better than those of unmodified silica. The reason was that silica compatibility with natural rubber and silica dispersion in rubber. The tensile strength of unmodified silica, admicellar silica and silica with a silane coupling agent was 11.7, 29.7 and 25.1 MPa, respectively. Also, the modulus of unmodified silica, admicellar silica and silica with a silane coupling agent was 1.4, 2.7 and 2.3 MPa, respectively.

The mechanical and thermophysical properties of NR filled with titanium dioxide and nano-silica were investigated at room temperature with different filler concentrations [121]. The tensile strength increased from 16.9 MPa to 18.4 and 26.5 MPa with the additions of 10 and 20 wt% nano-silica, respectively. Also, the modulus was increased from 8.8 MPa to 17, 26.7 and 27.2 MPa with the additions of 5, 10 and 20 wt% nano-silica, respectively.

The damping and mechanical features of silica/NR composites prepared from latex system were studied [46]. To make silica/NR master-batches, a well-dispersed silica suspension was made using a bead mill and then added to NR latex. On a two-roll mill, various rubber chemicals were combined with the coagulated silica/NR master-batches with 10-30 parts of silica per hundred parts of rubber (phr) (8.94-20.9 wt%). Without Si-69, the tensile strength progressively increased with enhancing silica loading up to 14.97 wt%. Due to poor silica dispersion, it had a tendency to decline when more silica was added. However, the tensile strength of 20.9 wt% silica-filled conventional composite without Si-69 was not much dissimilar from that of the unfilled NR vulcanizate. At 8.94 wt% silica loading, the tensile strengths of all conventional and master-batch composites were found to be similar. At higher silica loadings (14.97 and 20.9 wt%) and without Si-69, the master-batch composites displayed greater tensile strength than the conventional composites.

The mechanical properties of NR latex nano-silica composites were investigated [122]. Nano-silica, which was utilized as filler, was separately incorporated into the latex matrix. There was a noticeable increase in the properties when nano-silica was utilized as filler in the latex matrix due to the developed latex-nanoparticle interaction and better homogeneity in the distribution of nanoparticles in the latex matrix. The additions of 0.2, 0.4, 0.6, 0.8 and 1 wt% nano-silica to NR latex vulcanizates, the tensile strength increased gradually and reached a maximum and then slightly declined.

The optimization of the physico-mechanical properties of silica-filled NR/SBR compounds was studied [123]. The tensile strength of the NR/SBR blends was reduced with increasing SBR content. The tensile strength of NR/silica compounds 6.47, 12.15, 17.19 and 21.68 wt% silica was 15.2, 20.1, 15.5 and 8.1 MPa, respectively.

The effects of cyclohexylamine (CA) modified silica (Sil) addition on the mechanical properties of a NR were investigated [124]. The tensile strength of silica modified samples increased from 21.5 MPa to 27 MPa. The tensile strength of natural rubber vulcanizates had a maximum value at about 20.47 wt% silica. Furthermore, the highest modulus was 5.5 MPa.

The mechanical and fracture mechanical properties of the elastomers filled with the precipitated silica and nano-fillers based upon layered silicates were studied [125]. The vulcanizates were filled with various contents (4.52–39.90 wt%) of two filler types. The fillers were precipitated silica and an organic-modified nano-disperse layered silicate. The addition of precipitated silica increased the tensile strength of natural rubber from 7 MPa to 23 MPa.

Figures 2.26(a) and (b) show the tensile strength versus silica content of silica modified natural rubber composites. As is seen clearly in the same figure, an increase in nano-silica content in the natural rubber matrix increases the tensile strength. The maximum silica content is about 40 wt% and the maximum tensile strength is about 68 MPa.

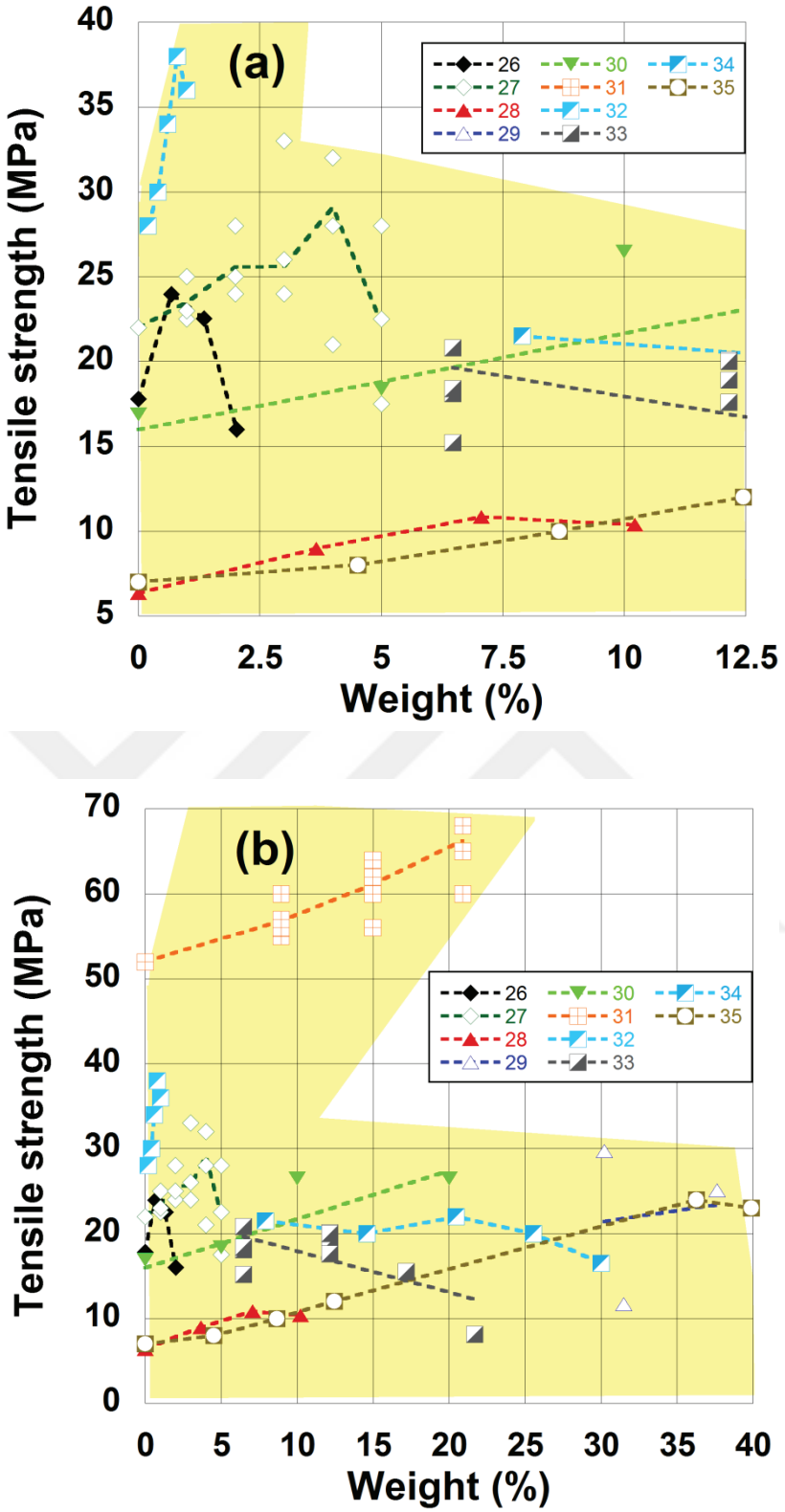

Figure 2.25. Tensile strength of (a) 0-12.5 wt% and (b) 0-40 wt% silica modified natural rubber composites 26 [126], 27 [117], 28 [118], 29 [119], 30 [120], 31 [121], 32 [46], 33 [122], 34 [123], 35 [124], 36 [125].

CHAPTER 3

DIATOM FRUSTULES

3.1. Diatom Frustules

Single-celled algae are known as diatoms [17, 127, 128], responsible ~25% of the world's primary food production [10] and release O_2 by a photosynthesis process that consumes a significant amount of atmospheric CO_2, claimed to be more than rain forests [129]. Each species of diatom (more than ten thousands) has a unique intricate 3D siliceous shell/skeleton of transparent, biogenic (or opaline) amorphous nano-silica particles, also known as frustule, and a surrounding soft organic matrix [130-133]. The frustule comprises pores, ridges and protuberance, the sizes, shapes and percentages of which alter locally, inherited from the different stages of a bio-mineralization process [134]. The location dependent mechanical properties make the diatoms mechanically highly efficient structures, bearing the loads 1000 times of their weight [130]. The sizes of frustules range 1-500 μm, and the pores 10-200 nm [14, 129, 135-137].

Diatoms are classified in two major groups, pennate (bilaterally symmetric) and centric (radially symmetric), based on the frustules symmetry (Figure 3.1). Pennate diatoms exhibit parallel striae, which are rows of holes oriented normally to the long axis of the silica. The striae are normally spaced 0.3-2 m apart. Costae are the silica rows that lie in between the striae. Costae are set up in honeycombs or combs (Figure 3.2). Frustules exhibit an unmatched structural difference in addition to their symmetry [128].

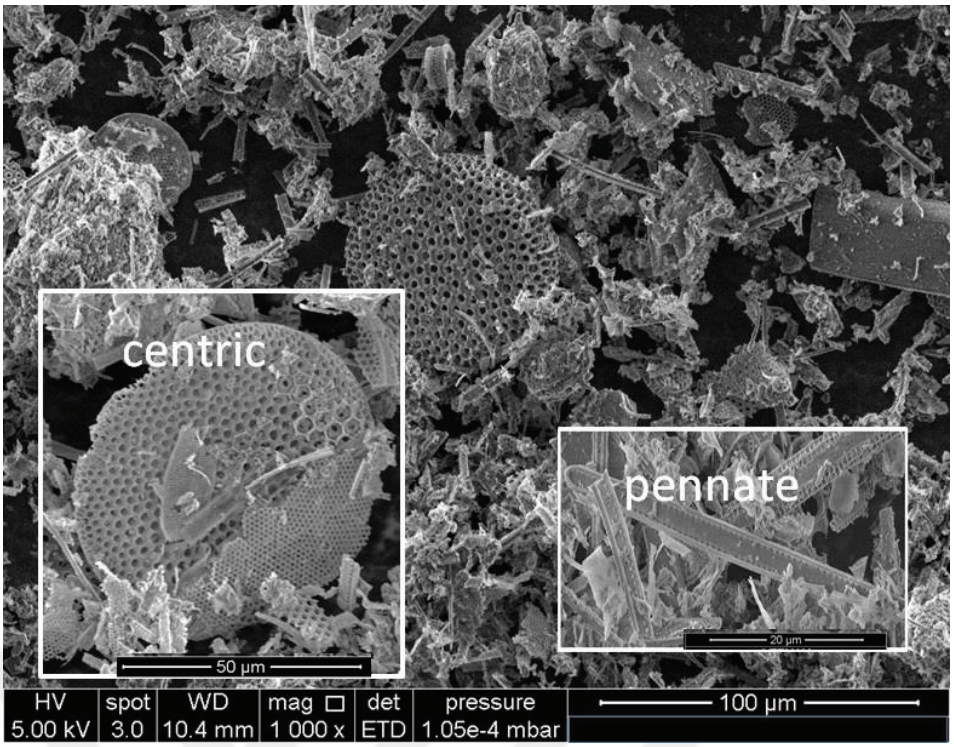

Figure 3.1. The SEM pictures of the as-received diatom frustules, centric and pennate partially crushed frustules.

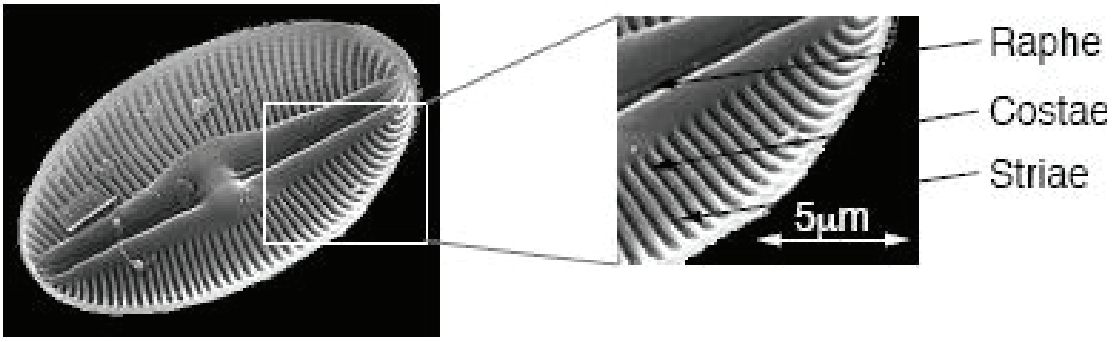

Figure 3.2. The pennate diatom displaying the central raphe, the striae and the costae [128].

Figure 3.3 shows a diagram of the siliceous parts of the diatom cell walls. The diatom frustule is made up of two almost equal halves that fit together like a Petri dish and enclose the majority of the single cell therein (Figure 3.3). The epitheca and hypotheca are the terms for the exterior and interior frustules, respectively (Figure 3.4). The bigger outer surface of each half (theca) is formed by a valve, and there are many girdle bands, which are ring-shaped silica structures (Figures 3.3 and 3.4). Every diatom

species produces frustules that are distinctively formed, with fine characteristics like ridges, pores, and protuberances arranged in complex, species-specific patterns. Amorphous silica skeletons have diameters range ~1-500 μm, but the regular features scattered across the frustules wall have typical dimensions of 10-200 nm [14, 129].

Figures 3.5 demonstrate similarities between the morphology of artificial and natural silica formations [138]. Macroporous silica can be used as a platform for in situ synthesis of Thrombin Binding Aptamer for optical biosensing purposes because of its similar morphology to the diatom Coscinodiscus wailesii, as shown in Figures 3.5 and 3.6. This material is produced by electrochemical etching of crystalline silicon followed by thermal oxidation at 900 °C (a and b). A chirped photonic-crystal fiber and the valve of the diatom Arachodiscus wailesii are seen in Figures 3.5(c) and (d), respectively. Both structures have the property of focusing the light. Synthetic and natural porous silica nanovectors for drug delivery are also shown in Figures 3.5(e and f), respectively.

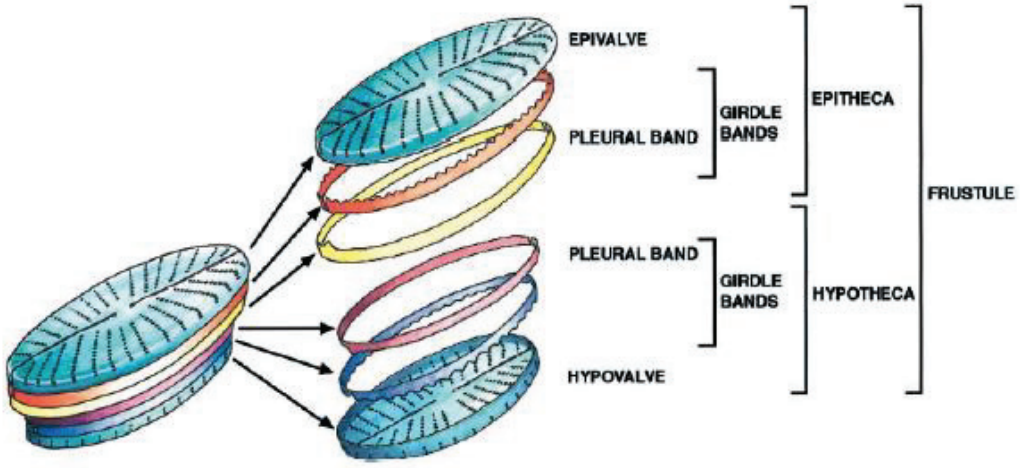

Figure 3.3. Diagram showing the siliceous elements in the diatom cell walls [139].

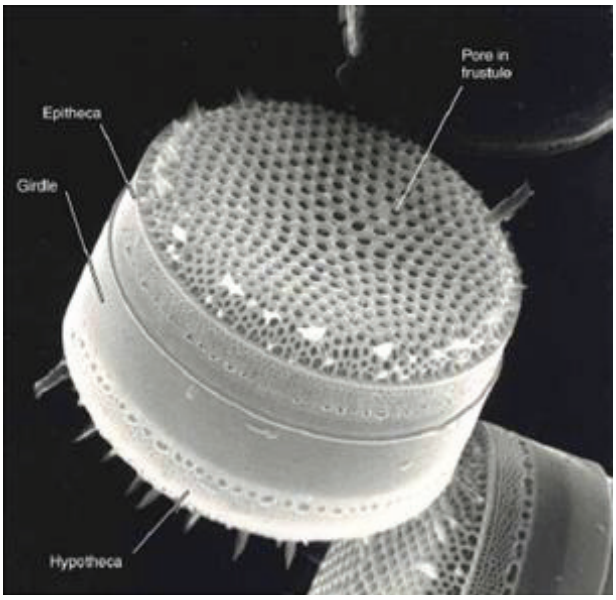

Figure 3.4. A SEM micrograph of Thalassiosira [9].

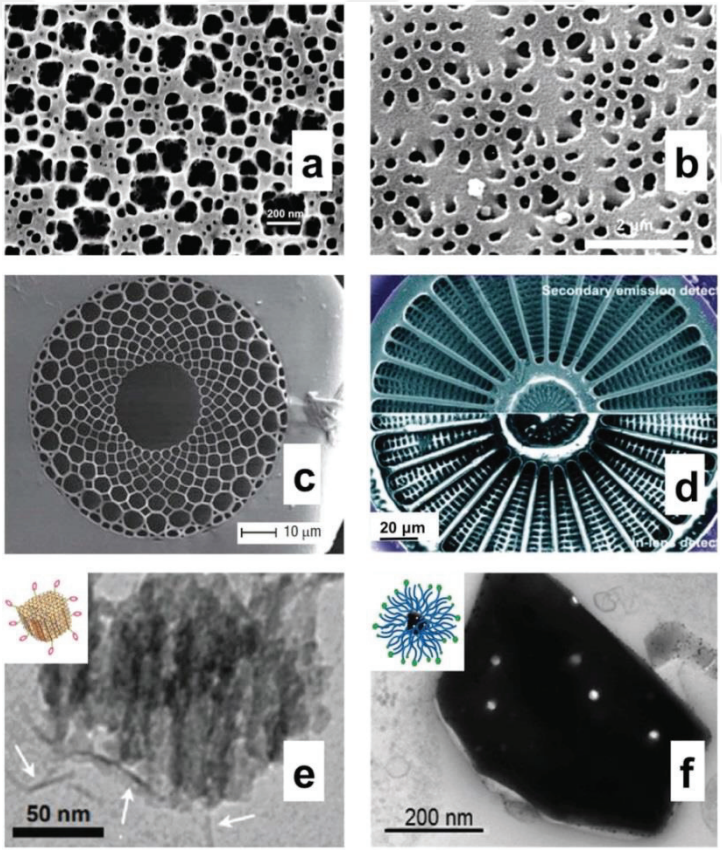

Figure 3.5. Comparative images of synthetic silica and diatom structures. a) Macroporous silica, b) detail of diatom Coscinodiscus wailesii, c) chirped photonic-crystal fiber, d) valve of diatom Arachodiscus wailesii, e) graphene oxide-modified porous silicon nanoparticles and f) Diatomite nanoparticles [138].

3.2. Potential Applications of Diatom Frustules

The frustules of diatoms are deposited on the ocean floor after the end of their cellular activities, and form a natural deposit known as diatomaceous earth (diatomite or Kieselguhr). Diatomaceous earth (DE) is a cheap material, abundant and has diverse applications in the heat and sound insulation, chemical reactions, sensors, explosives, filtration, absorption and abrasion [11, 17, 128, 140-143]. High porosity, low density, low thermal conductivity, and a high melting point (1400 to 1750 °C depending on impurities) are the qualities that make DE excellent for industrial usage. Diatomaceous Earth (DE) filtration is a process that uses diatoms or diatomaceous earth—the skeletal remains of small, single-celled organisms—as the filter media. DE filtration relies upon on a layer of DE placed on a filter element or septum and is frequently referred to as pre-coat filtration. DE filters are simple to operate and are effective in removing cysts, algae, and asbestos from water [144].

Diatoms provide raw materials for industry, environmental technologies, nutraceutical and feeds and microorganisms for genetic engineering (detailed in Figure 3.6). Diatoms are used in bioreactors, hybrid biosensors, drug delivery, water purification, immunoisolation, immunodiagnostic and immunosensors, nanotechnology, waste degradation and phytoremediation of heavy metals, nanomedicine, photonic devices and microfluids (Figure 3.7) [145-155]. The nano-sized, porous silica capsule can be exploited for drug carrier or release, where the drug molecules can be loaded on the internal and external surfaces of the diatoms [156]. Diatoms offer a possible alternative to non-renewable energy sources as a feedstock (Figure 3.9) [157]. Diatoms are possible to develop the quality of biodiesel by optimizing the content of various acids that impact biodiesel properties such as level of emissions, cetane number, oxidative stability, cold flow, lubricity and viscosity [158]. Also, diatoms have environmental metabarcoding approach which is based on DNA diversity in a natural environmental such as flora and fauna [159]. The precise taxonomic identification of the diatoms included in the eDNA sample is next made using the sequencing data generated from diatom metabarcoding. These results are then compared with those from the traditional morphological database to confirm their efficacy. To measure diatom diversity at the genus and species levels, the diatoms metabarcoding tool has been greatly improved. A long-term study has been done on the use of microalgae for wastewater treatment, which might be put to use in conjunction

with both small- and large-scale companies. Diatoms can utilise the extra industrial waste that is dumped in the aquatic system as a source of nutrients. Many wastewater types, including aquaculture (Figure 3.10) [160], brewery [161], and textile [162] have been investigated for phytoremediation capability. Diatoms are edible and can be utilized to make substances like vitamins, antioxidants, animal feed, and vegetarian protein supplements. Diatoms that contain carotenoids like fucoxanthin have been shown to possess a number of photosynthetic pigments [155]. Furthermore, the extracts of Nitzschia laevis, Nitzschia inconspicua, Navicula saprophila, and Phaeodactylum tricornutum contain a notable quantity of DHA and EPA and can be utilized as dietary supplements for both humans and animals.

Diatom frustules were also previously examined as temporary scaffolds in processing microscale structures of zirconia [13, 14], gold [15] and MgO and TiO_2 [16] and also for the improvement of nano-devices that can be engineered for energy harvesting [163, 164], anode composite material in Li-ion batteries [165] and thermal and theranostic applications, ranging from subcellular imaging to drug delivery [138, 166]. Moreover, as the cracks moved around silica particles that were around 40 nm in size, a great deal of energy was reportedly required to shatter the frustules and a large region of the fracture [9].

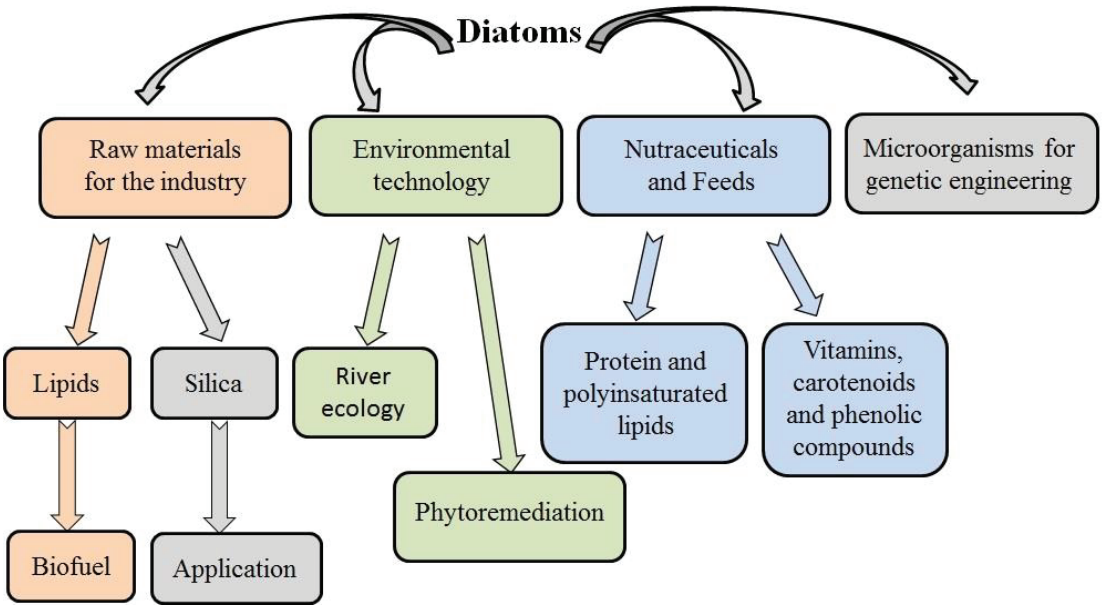

Figure 3.6. The different applications of diatoms in the green industry (modified [12]).

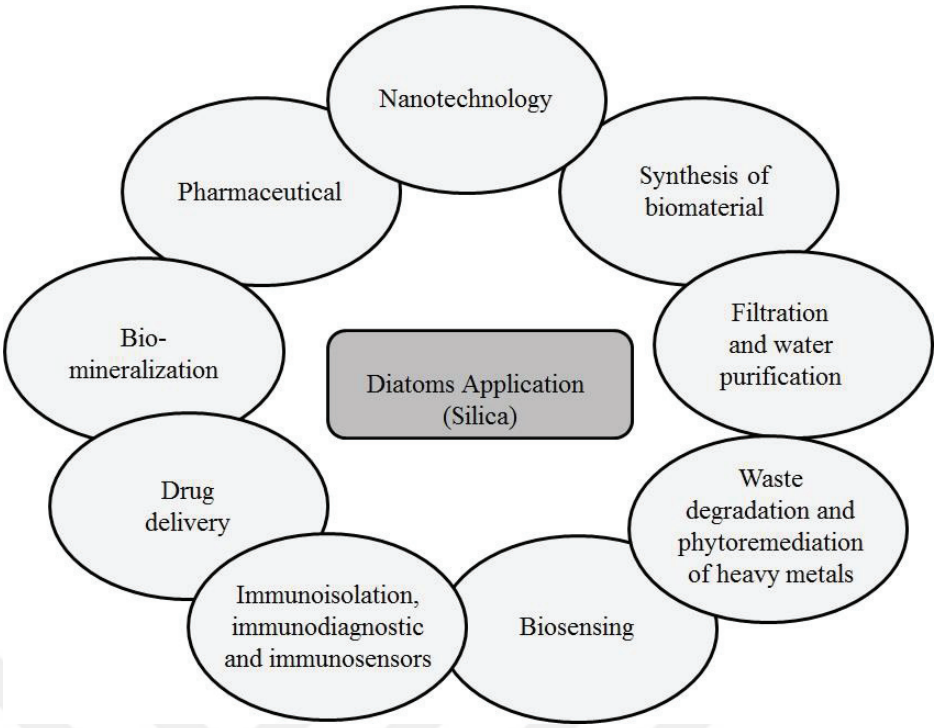

Figure 3.7. Applications of diatoms in different fields (modified [156]).

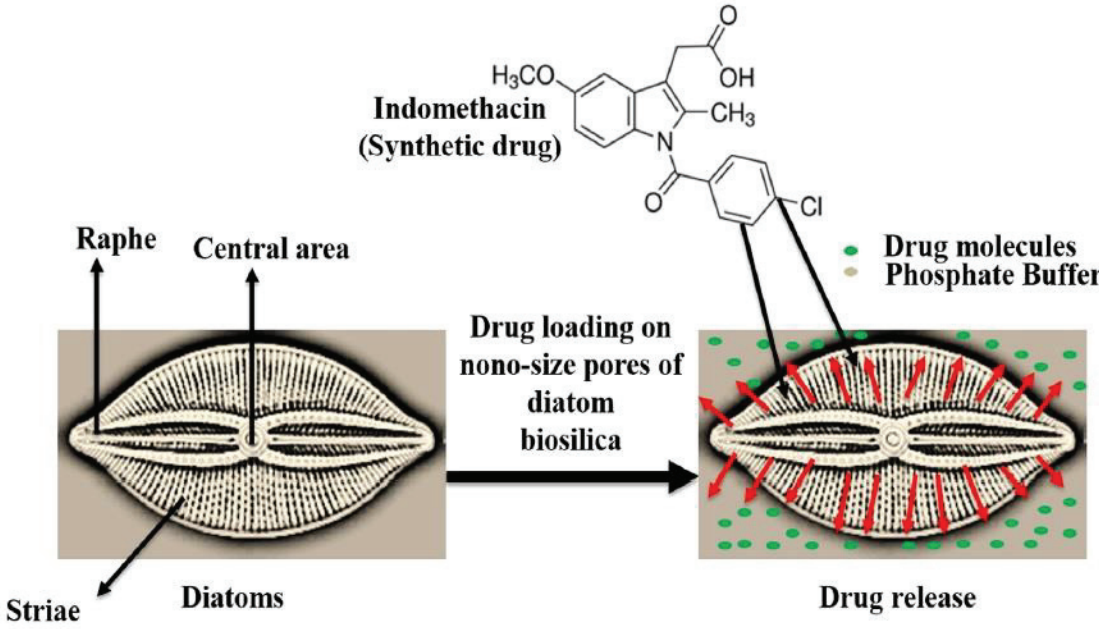

Figure 3.8. The mechanism of drug release from the porous diatom micro-shell [156].

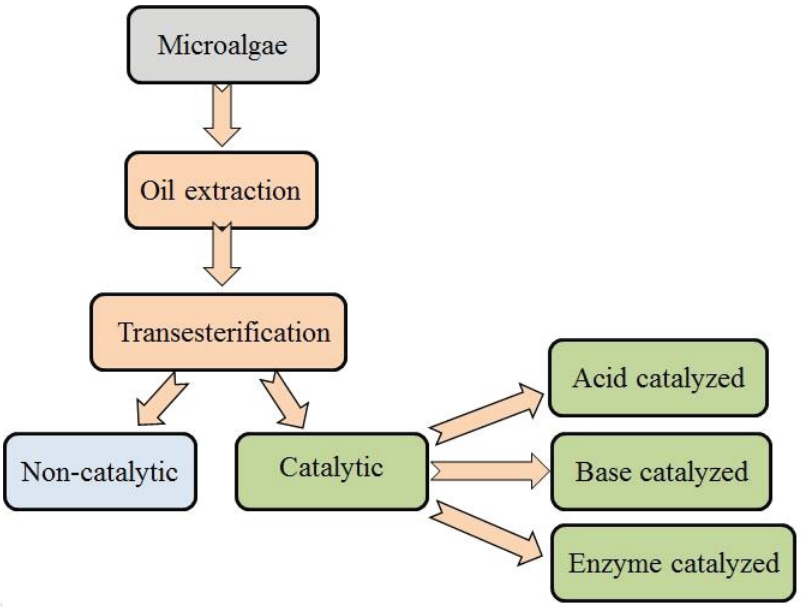

Figure 3.9. Biodiesel production steps from microalgae (modified [158]).

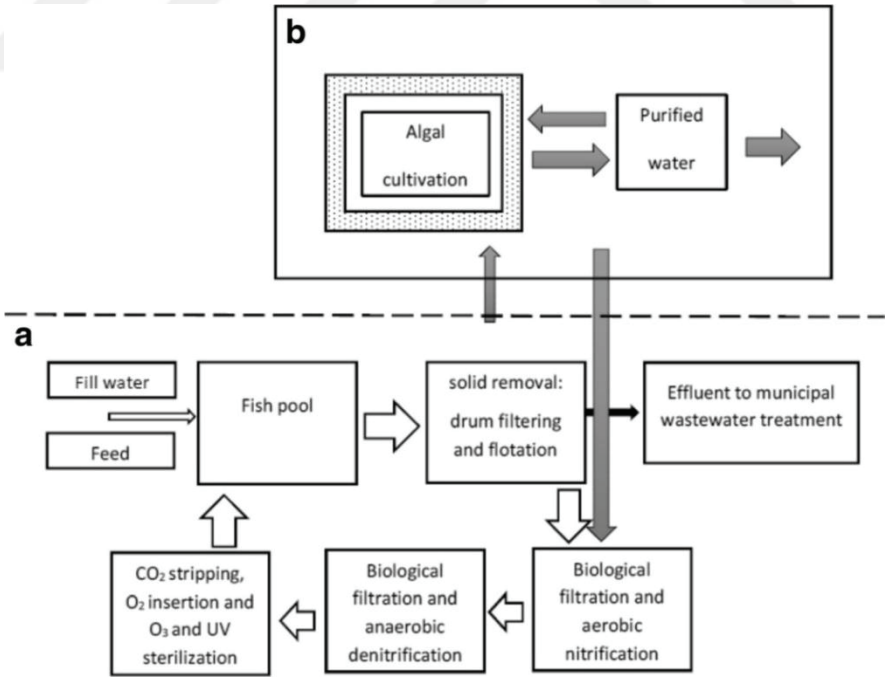

Figure 3.10. a) Recirculating aquaculture systems used for pike perch and catfish farming and b) potential algal cultivation unit connected to the recirculating aquaculture systems [160].

3.3. Mechanical Properties of Diatom Frustules Filled Composites

The natural and heat-treated frustules were previously studied as reinforcement/filler in polymeric matrices, lightweight concrete [167, 168] and also recently in an Al matrix (Figure 3.11) [169]. The compression stress-strain curves of hot-extruded Al-diatom frustules composites with various diatom frustules contents are shown in Figure 3.12(a). The samples with 3wt% diatom frustules exhibit the maximum strength (185.2 MPa) at 13.5% strain. While the ductility is apparently undermined with increasing diatom frustules contents (Figure 3.12(b)). The frustules as a reinforcing phase have a relatively high surface area (11.777 and 22 m^2 g^{-1} [170, 171]) and the thermoset resins can infiltrate easily through the regularly arrayed nano and micro pores of the frustules [14].

The effect of heat treatment and acid leaching on the shape of diatom frustules and the enlargement of frustules were also investigated in previous studies [172-178]. The inclusion of diatom frustules increased the matrix strengthening at a particular heat treatment temperature. This was attributed to the growth of the nanocrystalline grains within the frustules and the alteration in the crystal structure (Figure 3.13(a)) [179]. Also, the effect of diatom frustules shape and size on the compression stress-strain behavior of a polymer matrix at a quasi-static strain rate was determined [180]. For that, pennate-type in-house cultured Achnanthes Taeniata frustules and commercial diatomaceous earth frustules were used as fillers in an epoxy matrix. Although, both frustule additions increased the compressive strength of neat epoxy, the effect further increased with the Achnanthes Taeniata frustule addition (Figure 3.13(b)). Centric type diatom frustules obtained from DE (15 wt%) filter material was used as filler in an epoxy resin in order to assess the possible effects on the compressive behavior at quasi-static and high strain rates [181]. The result showed that 15 wt% frustule filling of epoxy increased both modulus and yield strength values at quasi-static and high strain rates without significantly reducing the failure strain. The effects of calcined diatom and natural diatom frustules filling (0–12 vol%) on the quasi-static tensile and quasi-static and high strain rate compression behavior of an epoxy matrix were studied experimentally [182]. Results of compression tests revealed that epoxy frustule filling boosted elastic modulus and yield strength values at quasi-static and high strain rates. While ND frustule filling had a stronger strengthening impact and a higher sensitivity to strain rate (Figure 3.14).

Sintering DE were also examined experimentally [183]. The bending strength of cold sintered diatomite exceeded 40 MPa. The failure stress increased up to ≈80 MPa after post-annealing at 800°C, whereas conventionally pressed samples sintered at 800 °C fail under ≈1 MPa. Also, DE is also useful in producing lightweight aggregates. So, the mechanical properties and absorption of lightweight concrete using DE were investigated [167]. The lightweight concrete made with lightweight aggregate from diatomaceous earth was pelleted and classified as a structural lightweight concrete with compressive strength above 25 MPa. The addition of 5% sawdust to the mixture improved the mechanical properties of the lightweight concrete produced as observed in the higher compressive strength, modulus of elasticity, splitting tensile strength, and flexural strength. Moreover, Portland cement (PC) in mortar and concrete was mixed with highly-reactive pozzolanic DE up to 40 [168].

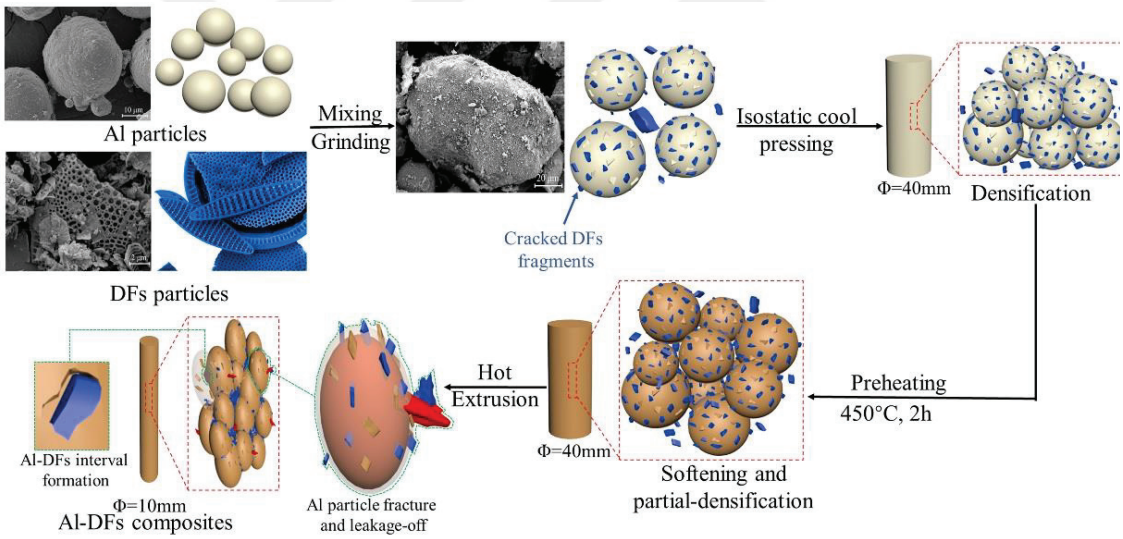

Figure 3.11. Schematic manufacturing of Aluminum-Diatom frustules composites alloys [169].

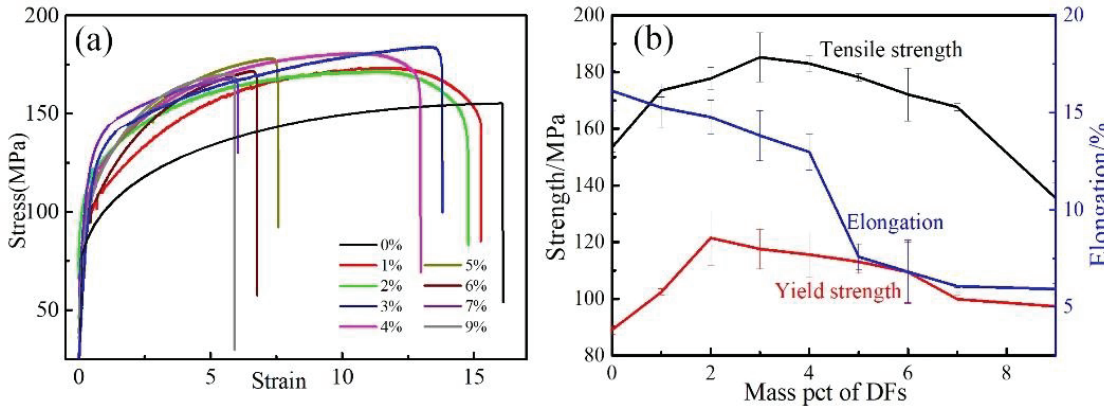

Figure 3.12. Mechanical properties of pure Al and Al-diatom frustules composites [169].

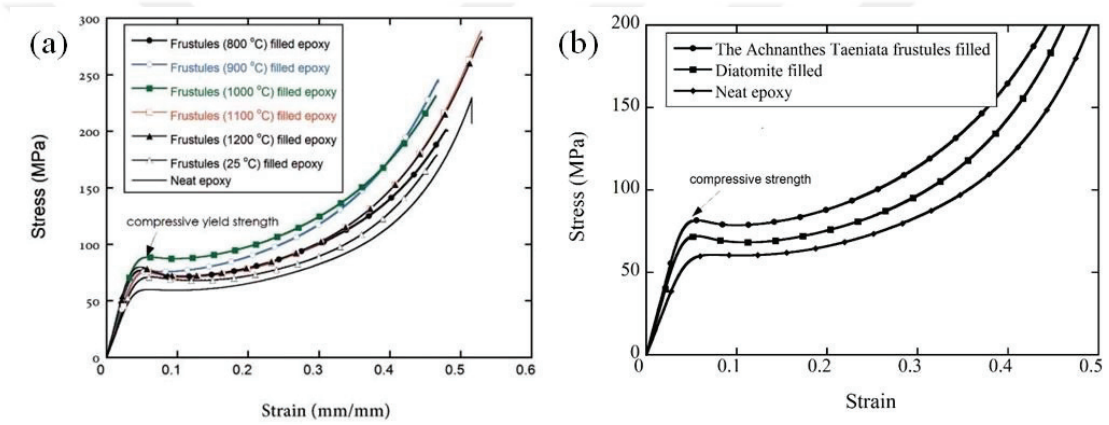

Figure 3.13. Compression stress–strain curves of (a) as-received and heat-treated frustules filled epoxy and neat epoxy [179], (b) neat epoxy, *Achnanthes Taeniata* frustule filled epoxy and diatomite filled epoxy [180].

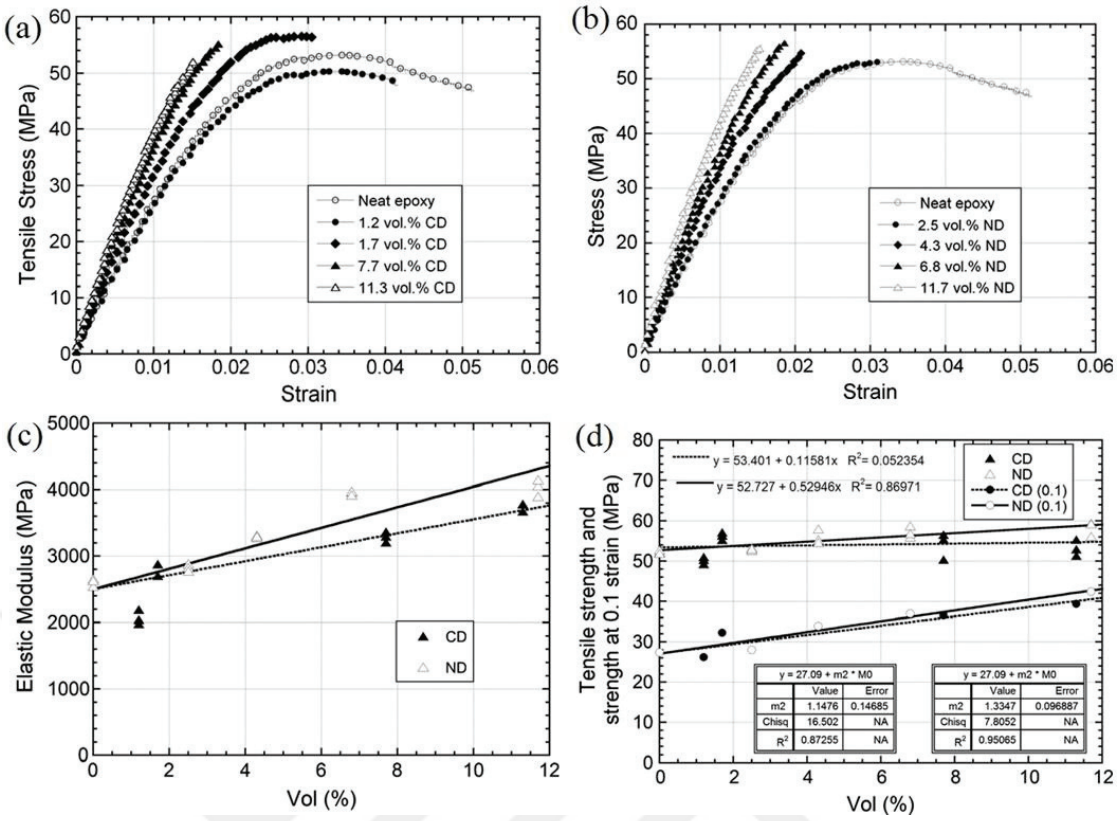

Figure 3.14. Tensile stress-strain curves for (a) CD and (b) ND filled epoxy, as well as variations in (c) elastic moduli and (d) tensile strength at 0.1 strain for various frustule volume percentages [182].

3.4. Motivation of Thesis

It is well known that the mechanical properties of composites can be significantly influenced by the geometrical characteristics of filler. For instance, the elastic modulus of the matrix has a lesser impact on the composite stiffness than the particle volume percent. The toughness and strength are increased by the strong particle matrix adherence. As it directly influences the particle matrix adherence, the surface area of filler material is also crucial for enhancing the mechanical properties of polymer matrices. Small filler sizes and extremely rough surfaces are typically associated with high surface area. Until now, the studies have improved the properties of silica/polymer nanocomposites, their preparation, characterization, mechanical properties and applications examples of which can be found in the refs. [184-192]. Nano-silica is generally synthesized by the sol-gel method which includes complex processes [52]. Diatom frustules can be utilized as a reinforcing

filler in polymeric composites because of their complex morphology and high surface area/volume ratio. This thesis is aimed to produce nano-size silica powder from diatom frustules and to use these powders as reinforcement in a polymer structure. A combined process of heat-treatment and acid leaching was selected, since the amorphous silica phase dissolves more rapidly than the crystal phase in hydrofluoric acid [18]. After a leaching process, the leachate was filtered to separate nano-size silica particles. Then, the filtered frustule was ball milled to obtain nano-size particles. Both powders (under filter and ball milled over filter) can be directly added to a matrix. Ball milled over filter powder was directly added to an epoxy matrix and the mechanical behavior of natural nano-structured diatom frustule added epoxy was experimentally investigated.

CHAPTER 4

EXPERIMENTAL STUDIES AND MODELS

4.1. Materials and Methods

The natural diatom frustules (diatomaceous earth) was received from Alfa Aesar, Johnson Matthey Co., England. The as-received frustules were previously characterized and the results of the characterization studies are given in several different publications [41, 137, 174, 177, 178, 183, 193].

The particle size analysis of natural diatom frustules and the silica powders was performed in a Malvern Master-sizer 2000 device. The X-Ray Diffraction (XRD) analysis of frustules and powders were performed in a Philips X'Pert Pro device (Cu-Kα radiation, 1.54 A°, 40 kV and (5–70°)). The amorphous and crystal phase percentages of frustules and powders were determined using Panalytical X'Pert Pro High Score Plus and Origin software. The elemental composition of natural diatoms was determined by an energy dispersive X-Ray Fluorescence spectrometer (XRF) (Spectro IQ II). The chemical bonding was studied by a Perkin Elmer Fourier Transform Infrared (FTIR) System Spectrum BX Spectroscopy. The morphological and surface topography features of frustules and the fracture surfaces of tested silica/epoxy composites were examined in an FEI Quanta 205 FEG SEM in secondary and back scattered electron modes.

The crystallinity was calculated using the following relation

$$\text{Crystallinity} = \frac{\text{Area of crystalline peaks}}{\text{Area of crystalline} + \text{amorphous peaks}} \times 100 \qquad (4.1)$$

4.2. Nano Silica Powder Processing of Frustules

Four different routes were used to process nano-silica powder from the as-received diatom frustules: (i) heat treatment, (ii) ball milling (500 rpm, 1 h) and (iii) hydrochloric (HCl) and hydrofluoric acid (HF) leaching. The schematic of the HF acid leaching processing steps is shown in Figure 4.1. The as-received frustules were heat-treated in a box furnace between 900 and 1200 °C at 100 °C intervals for 2 h. The selection of the lowest heat treatment temperature was based on a previous study, which demonstrated that the first cristobalite phase appeared at/after about 900 °C [178]. The as-received and filtered acid leached heat-treated frustules were ball milled in a Retsch PM 200 device at 500 rpm for 1 h in order to determine the effect of ball milling on the powder size. Milling was done in a 125 ml capacity agate pot using agate balls in 10 mm diameter. The ratio of frustules to balls was chosen 1:2. The as-received frustules and 900-1200 °C heat-treated frustules were leached in a HF-solution with 1, 3, 5, and 7 N concentrations in a polypropylene flask at room temperature (Isolab Laborgeräte GmbH). As shown in Figure 4.1, the leach solution was then filtered in a vacuum filtration system using a 1000 nm filter paper. The filtered frustule (above filter) was then dried in an oven together with the filter paper at 110 °C for 2 h. The filtered frustule was then ball milled at 500 rpm for 1 h. The particle size analysis of the nano powders (filter solution and ball milled above filter) was performed in water by using a Malvern Panalytical Zeta-sizer Nano Range particle size analyzer.

The schematic of HCl acid leaching processing steps is shown in Figure 4.2. The as-received frustules and 900-1200 °C heat-treated frustules were leached in a solution of 10% (3.18N) and 20% (6.36N) of HCl (100 ml) in a glass flask at room temperature (Isolab Laborgeräte GmbH). As-received and heat-treated frustules were kept at 100 ºC 4 h, cooled and diluted with 60 ºC warm distilled water. As shown in Figure 4.2, the leach solution was then filtered in a vacuum filtration system using a 1000 nm filter paper. Finally, filter paper was burned at 700 ºC for 1 h.

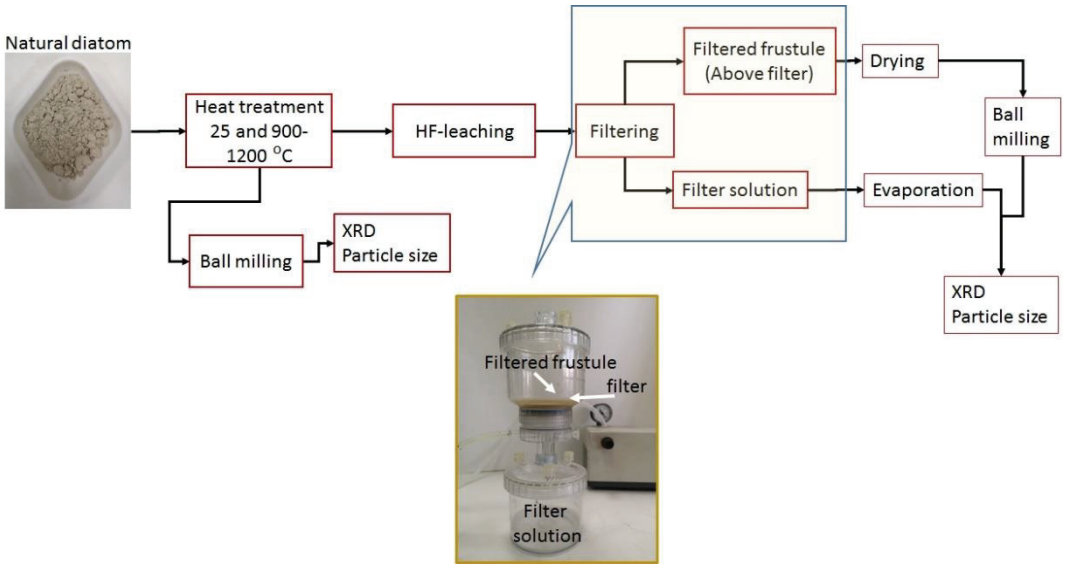

Figure 4.1. Schematic of HF acid leaching processing steps.

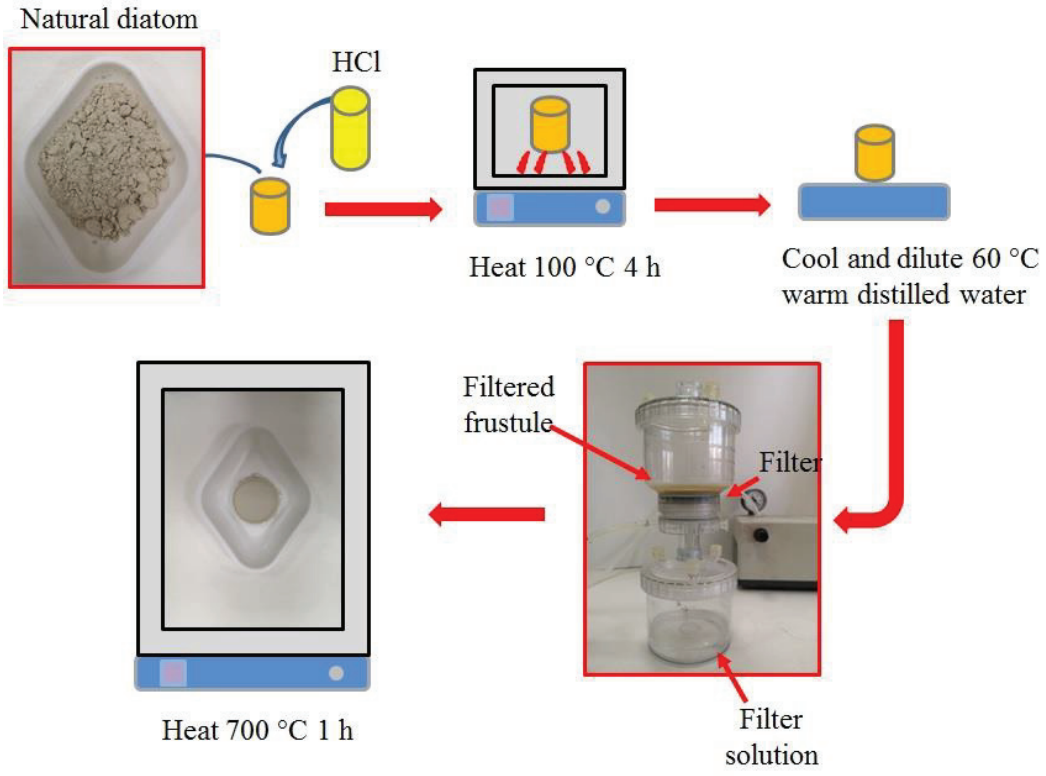

Figure 4.2. Schematic of HCl acid leaching processing steps.

4.3. Nano Silica Filled Epoxy Composite Processing and Testing

The diglycidyl ether of bisphenol-A (DGEBA) is the most commonly used epoxy resin as it has numerous desirable qualities, including fluidity, little shrinkage during curing, and simplicity of processing. Bisphenol A epoxy resin with hardener was used as a matrix (Epores 11564 and Epohard 13486). The resin and powder were mixed by disperser (Arzum AR1023) at 100 rpm 5 min. In order to prevent the production of gas bubbles, the hardener was added to the solution mixture under vacuum. Amounts of solution mixtures are tabulated in Table 4.1. Finally, the mixture was poured into a Teflon mold. As shown in Figure 4.3, the tensile test specimens were made using a rectangular Teflon mold and cured at room temperature for 24 h, followed by a post-curing process at 50 °C for 24 h in an oven. The tests were carried out in an AG-I Shimadzu quasi-static mechanical testing machine using epoxy tensile test specimens that were manufactured in accordance with ASTM D638M-91a standards (Type IV). The test setup and devices employed in the system are shown in Figure 4.4. An external digital camera was employed during the testing to record the deformation. Two-gauge markers were put onto the upper and lower bounds of the gauge length to make that zone visible to the extensometer in order to measure the change in the gauge length. At least three tests were conducted with a strain rate of $1x10^{-3}$ s^{-1}, and the tested and fractured specimens were kept in a desiccator until microscopic examination.

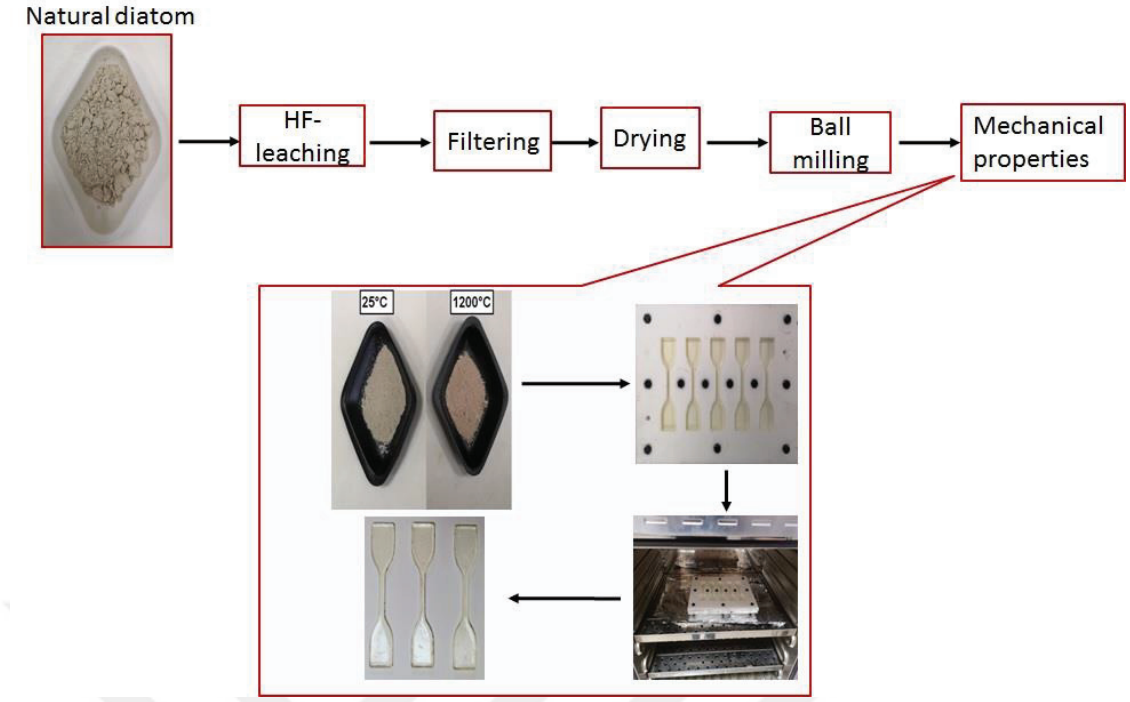

Figure 4.3. Schematic of nano-silica filled epoxy composite processing and testing.

Table 4.1. The solution mixture of the 1200 °C heat-treated, HF-treated (1 N HF 15 min) and ball milled (500 rpm 1 h) diatom frustules.

Powder amount (mg)	Fiber density (g/cm^3)	Matrix density (g/cm^3)	Fiber volume (cm^3)	Molding volume (cm^3)	Epoxy (g)	Hardener (g)	Vol (%)	Wt (%)
128.15	2.33	1.15	0.055	11	9.44	3.21	0.5	1.165
256.3	2.33	1.15	0.11	11	9.44	3.21	1	2.33
512.6	2.33	1.15	0.22	11	9.44	3.21	2	4.66

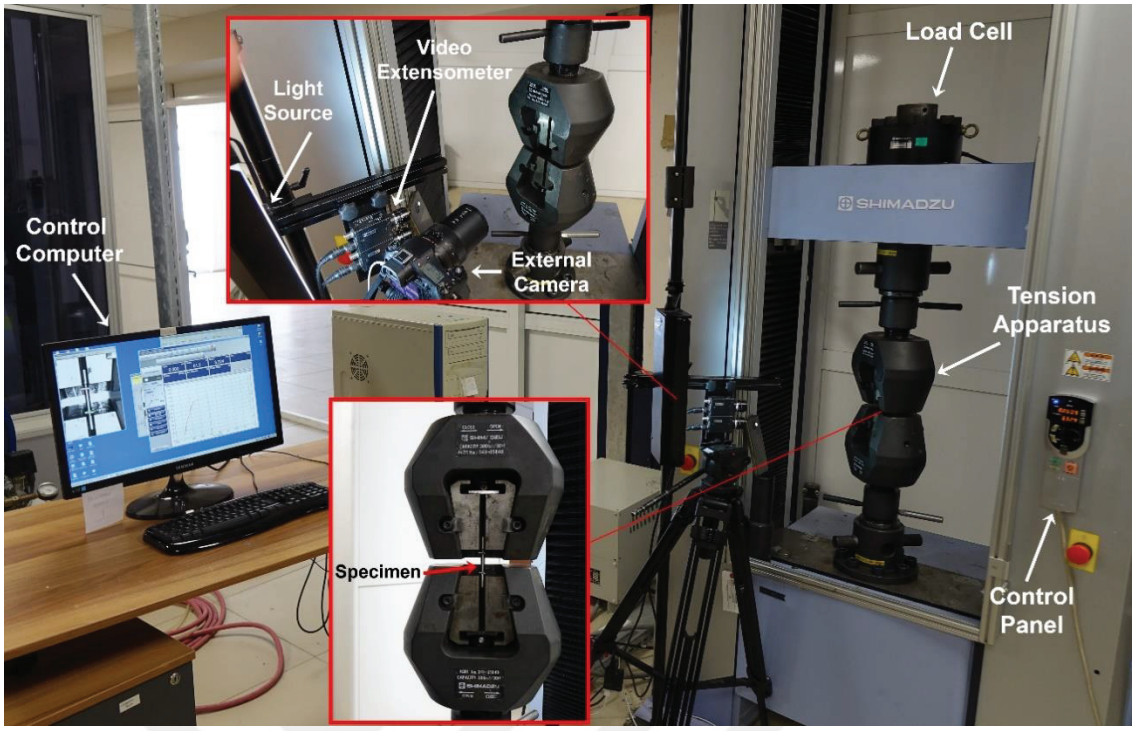

Figure 4.4. Quasi-static tension test setup.

The engineering stress (σ_{eng}) in the tensile tests was calculated using

$$\sigma_{eng} = \frac{P}{A_0} \tag{4.2}$$

where, A_0 is the initial cross-sectional area of the specimen and P is the applied load. The engineering strain (ε_{eng}) was calculated as

$$\varepsilon_{eng} = \frac{l_f - l_0}{l_0} = \frac{\Delta l}{l_0} \tag{4.3}$$

Where, l_f is the final gauge length and l_0 is the initial of the specimen. The true stress (σ_{true}) and true strain (ε_{true}) were sequentially defined as

$$\varepsilon_{true} = \ln \frac{l_i}{l_0} \tag{4.5}$$

$$\sigma_{true} = \frac{P}{A_i} \tag{4.4}$$

In above equation, l_i and A_i are length of the specimen the instantaneous and cross-sectional area. The engineering stress-strain data were transformed into true stress-strain data by taking into account no volume change in plastic deformation as

$$A_0 l_0 = A_i l_i \tag{4.6}$$

Then equation 4.6 is written as

$$\sigma_{true} = \sigma_{eng}(1 + \varepsilon_{eng}) \tag{4.7}$$

And, equation 4.7 is written as

$$\varepsilon_{true} = \ln(1 + \varepsilon_{eng}) \tag{4.8}$$

The true strain rate ($\dot{\varepsilon}_{true}$) was calculated using the following relation

$$\dot{\varepsilon}_{true} = \frac{d\varepsilon_{true}}{dt} \tag{4.9}$$

where, *t* is the time.

4.4. Theory of Composite Models

Composite models have been investigated for predicting the mechanical and thermal features of particulate and short fiber composites. Two basic models are the law of mixtures and Eshelby's model.

4.4.1. Law of Mixtures

It is considered a composite with N various reinforcing elements dispersed throughout a matrix. Assume that the elastic modulus and volume fraction of matrix material are E and V_0 and each fiber has a modulus of E_i and the volume fraction of fibers is V_i(i=1,2,3,…..N), respectively. The modulus of composites E_c is considered by

$$E_c = \sum_{i=0}^{N} V_i E_i \tag{4.10}$$

where

$$\sum_{i=0}^{N} V_i = 1 \tag{4.11}$$

The average strain $\bar{\varepsilon}$ can be explained by assuming that the externally imposed strain E_a is is equal to the shear strains in all phases, including the matrix. Since the stress in the i th phase, σ_i, is given by $E_i\bar{\gamma}$, the average stress in the composite $\bar{\sigma}$ can be approached by

$$\bar{\sigma} = \sum_{i=0}^{N} V_i \sigma_i = \sum_{i=0}^{N} V_i E_i \bar{\varepsilon} \tag{4.12}$$

On the other hand, the average stress $\bar{\sigma}$ is related to the applied strain $\varepsilon_a (= \bar{\varepsilon})$ by

$$\bar{\sigma} = E_c \bar{\varepsilon} \tag{4.13}$$

From equations (4.12) and (4.13) one can be acquired eq. (4.10). If the moduli E_c and E_i are replaced by the strength of composite (σ_c) and reinforcing materials (σ_i), composite strength can be obtained by

$$\sigma_c = \sum_{i=0}^{N} V_i \sigma_i \tag{4.14}$$

In this case of two-phase system, one kind of reinforced element and matrix, Eqn. (4.14) can be written as

$$\begin{aligned} \sigma_c &= V_0 \sigma_0 + V_1 \sigma_1 \\ &= V_m \sigma_m + V_f \sigma_f \end{aligned} \tag{4.15}$$

The fiber and matrix are demonstrated as *f* and *m*, respectively. Because there are differences in the strains between the fiber and the matrix, the value estimated by low of mixtures is an upper bound [194].

4.4.2. Eshelby Model

The elastic stress field surrounding an ellipsoidal particle in a finite matrix served as the basis for the Eshelby model [195]. The Eshelby model provides a solid method for predicting the Young's modulus of short fiber composites, even though it cannot be utilized to forecast stress transfer. The Cartesian coordinates, X_1, X_2, and X_3, are utilized, and X_3 is the axis of symmetry of the ellipsoidal inclusion. A stress, σ_0, is applied to the composite in the X_3 direction. In this case, the remote applied strains, ε_{ij}^{a}, become

$$\varepsilon_{11}^{a} = \varepsilon_{22}^{a} = \frac{-\nu_m \sigma_0}{E_m} \tag{4.16.a}$$

$$\varepsilon_{33}^{a} = \frac{\sigma_0}{E_m} \tag{4.16.b}$$

where ν is Poisson's ratio. Without the inclusion, the system experiences uniform deformation due to the applied strain. In the absence of the inclusion, the deformation throughout the system is uniform ε_{ij}^{a}. However, the inclusion's presence perturbs the deformation, and the strain brought on by this disruption is known as the constrained strain, ε_{ij}^{c}. An equivalent inclusion that shares the matrix elastic constants and experiences an equivalent transformation strain takes the place of the real inclusion, ε_{ij}^{t}, in order to overcome this issue. The displacement and stress within the equivalent and true inclusions must, however, be identical for this substitution to work, such that [196]

$$K_e(\varepsilon^c + \varepsilon^a) = K_m(\varepsilon^c + \varepsilon^a - \varepsilon^t) \tag{4.17.a}$$

$$G_e\left('\varepsilon_{ij}^{c} + '\varepsilon_{ij}^{a}\right) = G_m\left('\varepsilon_{ij}^{c} + '\varepsilon_{ij}^{a} - '\varepsilon_{ij}^{t}\right) \tag{4.17.b}$$

The ellipsoidal inclusion is indicated by the subscript "e," the dilatational and deviatoric strains are indicated by the subscript ε and $'\varepsilon_{ij}$, respectively, and *K* and *G* are the bulk modulus and shear modulus, respectively. When the volume fraction of inclusions is finite, there are two parts to the constrained strain in the inclusion, such that [197]

$$\varepsilon_{ij}^{c} = \varepsilon_{ij}^{c\prime} + \varepsilon_{ij}^{c\prime\prime} \tag{4.18}$$

In above equation, $\varepsilon_{ij}^{c\prime}$ is the constrained strain component a single inclusion can be connected to the transformation strain by when it is embedded in an infinite matrix [198]

$$\varepsilon_{ij}^{c\prime} = S_{ijkl}\varepsilon_{kl}^{t} \tag{4.19}$$

where, S_{ijkl} is the Eshelby tensor and is a function of the aspect ratio of the inclusion and Poisson's ratio of the matrix. The second constrained strain component, $\varepsilon_{ij}^{c\prime\prime}$ is introduced to account for the effect of the presence of other inclusions on an inclusion, and can be related to the transformation strain by [199]

$$(1-f)\varepsilon_{ij}^{c\prime\prime} + f\left(\varepsilon_{ij}^{c} - \varepsilon_{ij}^{t}\right) = 0 \tag{4.20}$$

The solutions of the strain components, ε_{ij}^{c} and ε_{ij}^{t} can be obtained by solving Eqs. (4.16) -(4.20). The stress/strain relationship can be used to calculate the stress in the ellipsoidal inclusion in the loading direction, σ_e, such that [195]

$$\sigma_e = \frac{v_e E_e(\varepsilon^c + \varepsilon^a)}{(1+v_e)(1-2v_e)} + \frac{E_e(\varepsilon_{33}^c + \varepsilon_{33}^a)}{1+v_e} \tag{4.21}$$

The composite's effective Young's modulus in the loading direction, E_o, can be obtained by dividing the applied stress with the average strain in the composite in the loading direction, such that [197]

$$E_0 = \frac{\sigma_q}{\varepsilon_{33}^a + f\varepsilon_{33}^t} \tag{4.22}$$

It is noted that formulations of the solutions of ε_{ij}^{c} and ε_{ij}^{t} (and hence σ_e and E_o) are lengthy and have been obtained by Tandon and Weng [199, 200].

4.5. Numerical Modelling

Solid structure modeling, mesh application, pre-processing of the simulation, the solution, and numerical result confirmation are the steps of numerical modeling that are shown in Figure 4.5. The 3D modeling of the geometries was performed in Solidworks and then saved as IGES files that could be accessed with Hypermesh meshing software. Quad elements were used to mesh the composite samples. To specify material properties, contacts, boundary conditions, termination time, test conditions, and mass scaling for quasi-static testing. The meshed structures were saved as. k files and exported to LS-PrePost software. The solution was used in LS-DYNA SOLVER, and the numerical and experimental results were compared. MAT_ISOTROPY_ELASTIC (MAT_001) and MAT_PIECEWISE_LINEAR_PLASTICITY (MAT_024) (LSTC, 2016) is an elasto-plastic material model, used in the numerical modelling.

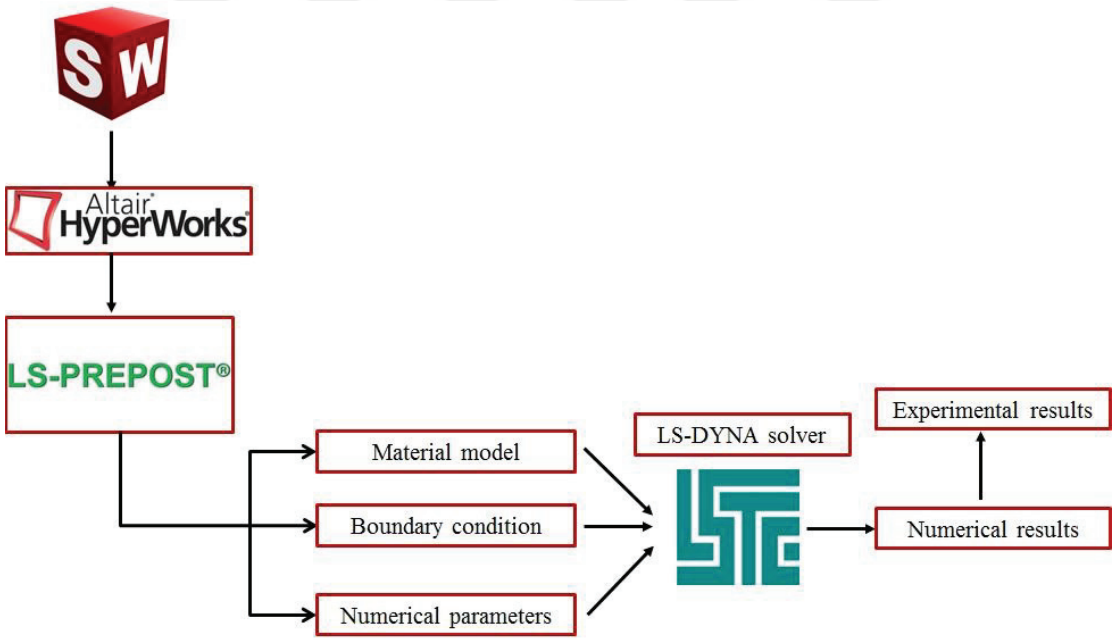

Figure 4.5. Steps in numerical model.

4.5.1. Unit Cell Model

The matrix is supposed to contain spherical, elastic, and uniformly dispersed silica nanoparticles. A particle in a cylinder-shaped matrix phase is utilized to model the entire composite structure as the unit cell (Figure 4.6). Only one quarter of the axisymmetric unit cell was utilized in the model calculations due to symmetry. Figure 4.7 shows the model's geometrical parameters which are the particle radius, unit cell cylinder radius, and height.

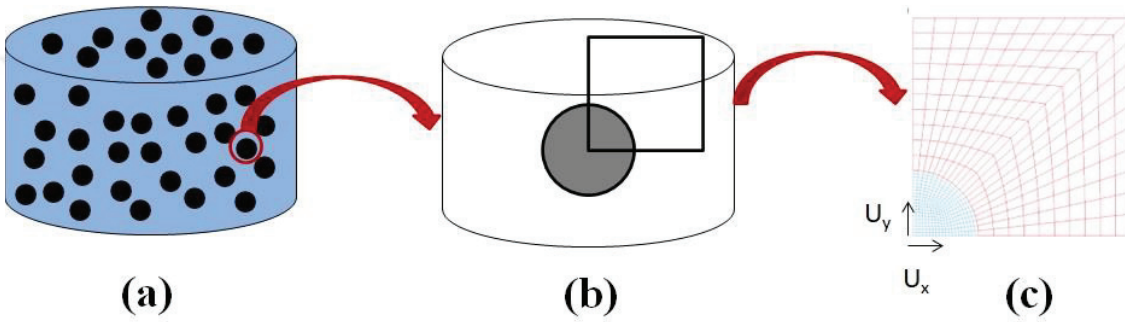

Figure 4.6. The axisymmetric unit cell model showing a) composite, b) unit cell and c) a quarter of the unit cell.

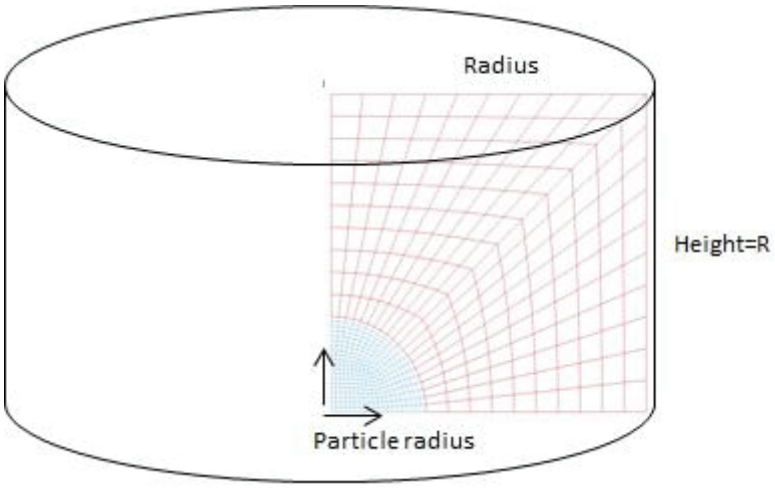

Figure 4.7. Geometrical parameters of the model.

The effect of reinforcement volume fraction on the stress-strain behavior of the silica nanoparticles was investigated using 2 volume percent of silica nanocomposites. In the composite, it is assumed that the particles are spherical and evenly dispersed. The square shape of the particle packing geometry was adopted. It was assumed that the unit cell would be 5 cm in length. The particle radius was calculated using the following equation:

$$r = \left(\frac{R^3 6f}{4}\right)^{1/3} \tag{4.23}$$

In above, R is the length of the unit cell, r is the particle radius, and f is the particle volume fraction. The cylinder's height and diameter are equal since the particle packing geometry is square.

Quadrilateral axisymmetric elements were used in the meshing of the unit cell. Two mesh sizes were investigated: coarse meshing includes 500 elements (300 silica and 200 epoxy) 0.75 mm length and fine meshing includes 2000 elements (1200 silica +and 800 epoxy) 0.375 mm length. Figure 4.8 displays the meshing unit cells with boundary conditions. The unit cell's left edge was fixed on the x-direction, with dx=0, and its bottom edge was fixed on the y-direction, with dy=0, due to the symmetry. For geometric fitting, the top edge's y-direction constraint was dy/y=0. Additionally, the unit cell's right edge was fixed at dx=0 in the x direction.

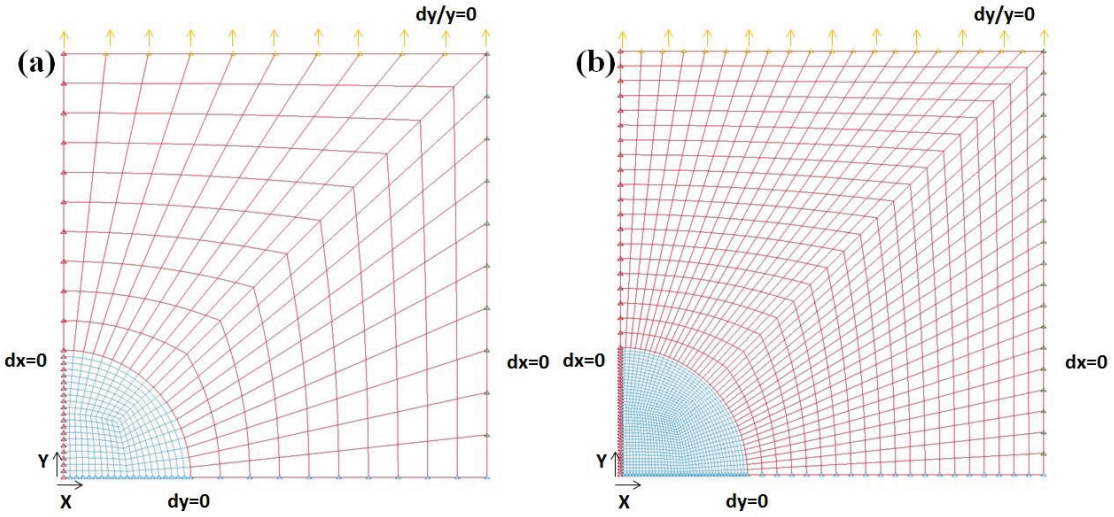

Figure 4.8. Meshed unit cell model and boundary conditions (a) coarse and (b) fine meshing applied.

The model was subjected to a simulation of uniaxial loading by having an incremental y-direction displacement imposed. The deformation of the composite was modeled using the effective plastic strain of plastic flow of the epoxy matrix and the elastic properties of the silica reinforcement. The elastic modulus and the density of the silica reinforcement were taken as 65 GPa and 2.32 g/cm^3, respectively. The Poisson's ratios of silica were taken 0.001 and 0.17. Also, the elastic modulus, density and Poisson's ratio of the epoxy matrix were taken as 4.23 GPa, 1.15 g/cm^3, 0.33, respectively. The macroscopic stress was calculated using,

$$\sigma_{Ci} = \frac{\sum_{j=1}^{N} \sigma_j}{N} \tag{4.24}$$

Where N is the total number of gauss points, σ_j is the element stress at the gauss points and σ_{Ci} is the average composite stress at ith increment. Macroscopic strain was calculated using,

$$\varepsilon_i = ln\frac{l_i}{l_0} \tag{4.25}$$

where, *l* is the final and lo is the initial length of the unit cell and *i* is the increment number.

CHAPTER 5

EXPERIMENTAL RESULTS

5.1. Characterization of Natural Diatom Frustules

The X-Ray Florescence spectrometer (XRF) analysis showed that the natural diatom frustules were composed of 90.08% of SiO_2 and with minor quantities of other oxides as tabulated in Table 5.1. The highest amount of other oxides was Al_2O_3 with an amount of ~5.5%. The XRD pattern of the as-received frustules shown in Figure 5.1(a) indicated that the structure was mainly composed of Opal-A and quartz (SiO_2, Ref. 82-0511).

Table 5.1. Chemical composition of diatom frustules.

Constituents	Natural Diatom (wt%)
SiO_2	90.08
Al_2O_3	5.53
Fe_2O_3	1.52
CaO	0.51
MgO	1.03
TiO_2	0.21
Na_2O	<0.02
P_2O_5	0.23
MnO	<0.002
K_2O	0.48
Cr_2O_3	0.089
Loss on ignition	**1**

The XRD patterns of the heat-treated frustules are shown in Figure 5.1(b) at different heat-treatment temperatures. As is seen in the same figure, the peak intensity of quartz at approximately $2\theta=26°$ declines as the heat treatment temperature of natural

diatom frustules rises to 900 °C, signaling the beginning of the transformation of the amorphous phase into crystal structure. The XRD pattern of natural diatom heat-treated at 1200 °C displays a crystal structure (Figure 5.1(b)). The percent crystallinity of the as-received frustule is calculated 9.3% and the crystallinity increases to 19.9, 33.5, 38.8 and 46.2% as the heat-treatment temperature sequentially increases to 900, 1000, 1100 and 1200 °C, respectively. The FTIR chart of the as-received frustules as seen in Figure 5.1(c) has three distinctive broad bands at 1066, 803, and 541 cm^{-1}. The Si-O-Si anti-symmetric stretching mode occurs at 1076-1100 cm^{-1}, the symmetric Si-O-Si stretching mode at 750-850 cm^{-1} and the bands at 618 and 450 cm^{-1} are specific to the Si-O-Si framework.

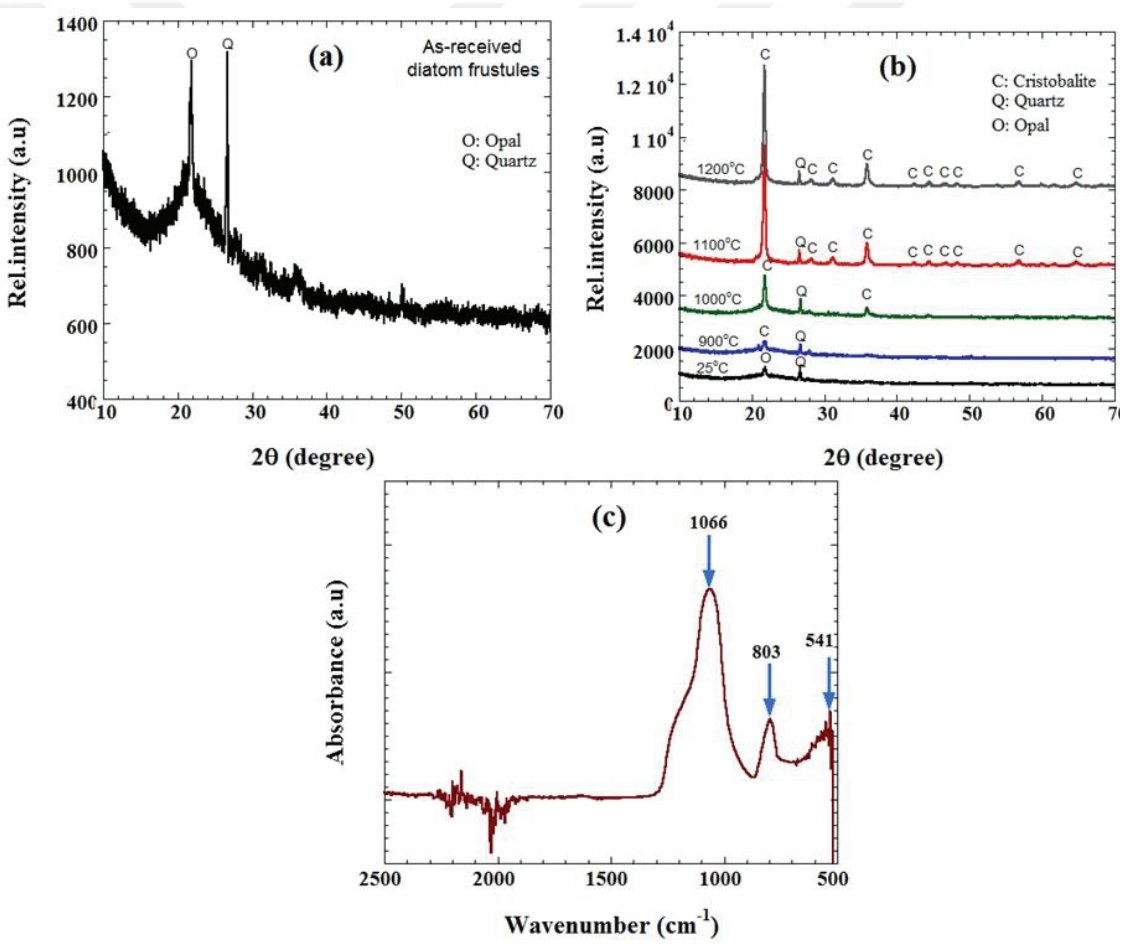

Figure 5.1. X-ray diffraction pattern of (a) as-received, (b) heat-treated frustules and (c) FTIR chart of natural diatom frustules.

Figures 5.2(a-f) are the SEM micrographs of the as-received diatom frustules at different magnifications. The multilevel pore sizes of a valve are clearly seen in the high magnification SEM pictures in Figures 5.2(d-f). The valve seen in these figures is an areola, which includes four densely porous membranes: cribellum, the sieve membrane (outer), loculate wall structure and the pore membrane (inner). As seen in Figure 5.2(f), the cribellum has different sizes of pores (the outermost is around 100 nm and the inner is about 50 nm in size). The external foramina ranges from 1.2 to 2 μm, the diagonal of the hexagonal cavity is approximately 2.6 μm, and the size of the internal foramina varies between 0.8 and 1 μm (Figure 5.2(f)).

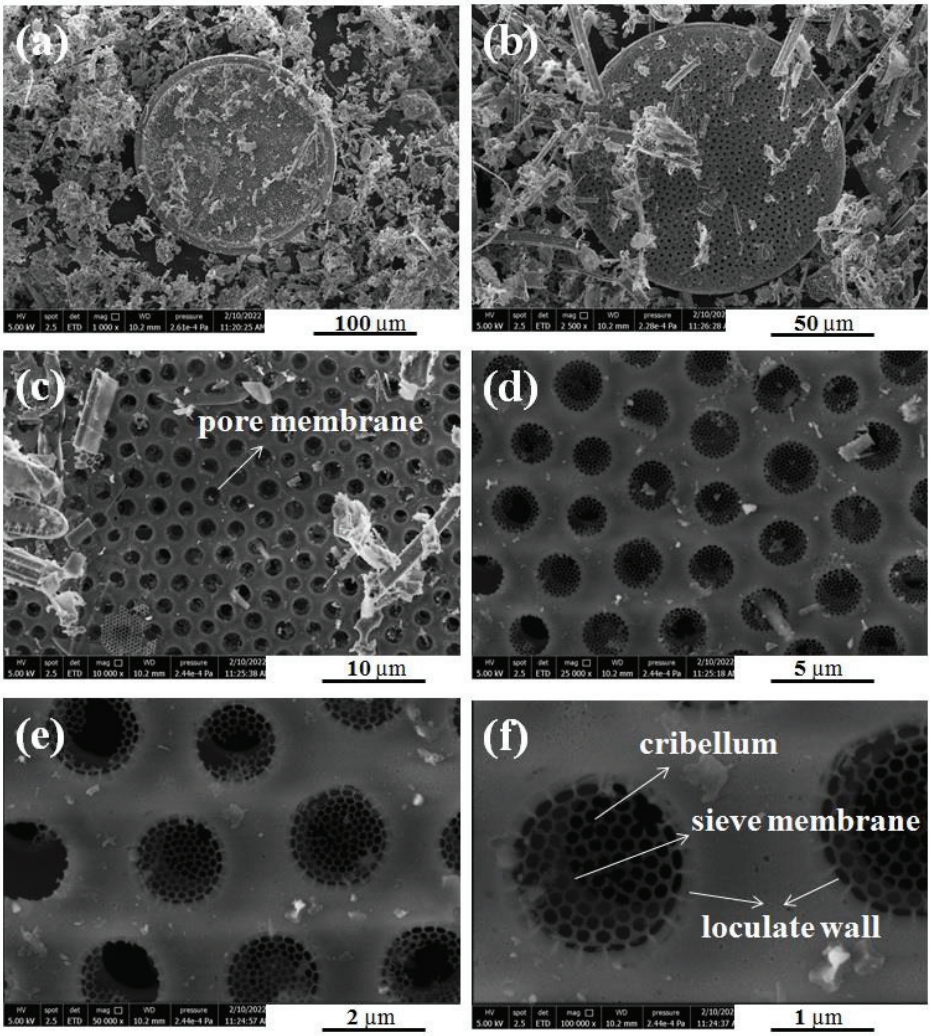

Figure 5.2. The SEM pictures of as-received natural diatom frustules at (a,b) low, (c,d) intermediate and (e,f) high magnifications.

The particle size distribution of as-received and heat-treated diatom frustules is shown in Figures 5.3(a and b). Ninety percent of the sizes of the as-received natural diatom frustules is less than 44.4 µm, 50% less than 15.6 µm and 10% less than 3.8 µm, as tabulated in Table 5.2. The mean particle sizes of heat-treated frustule ranges 14.7-13.7 between 900-1200 °C as tabulated in same table.

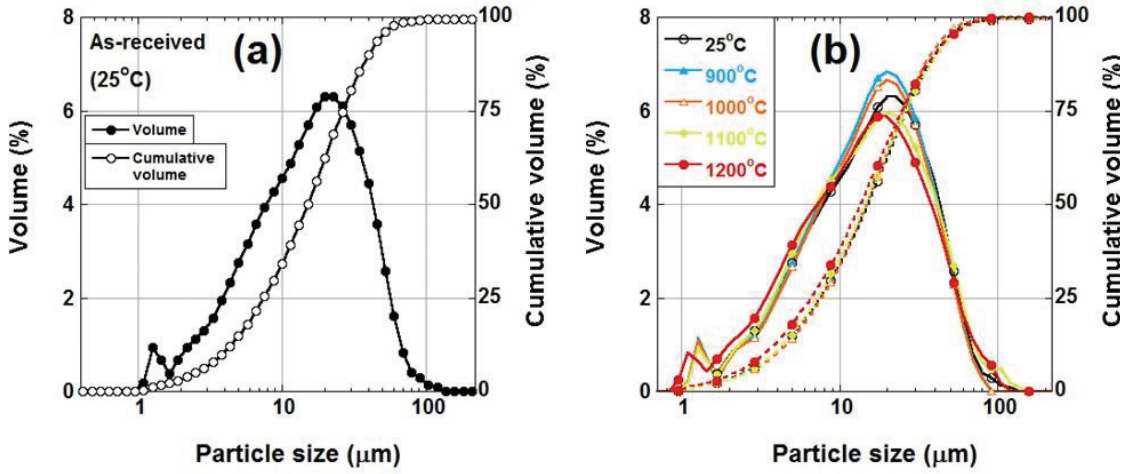

Figure 5.3. Particle size distribution of (a) as-received and (b) heat-treated diatom frustules.

Table 5.2. Particle size distribution of as received and heat-treated natural diatom frustules.

Frustule	D(0.1) (µm)	D(0.5) (µm)	D(0.9) (µm)
25 °C (as-received)	3.8	15.6	44.4
900 °C	3.7	14.7	38.9
1000 °C	3.6	14.5	39.1
1100 °C	3.5	14.4	40.2
1200 °C	3.3	13.7	41.4

5.2. Ball Milling of Natural Diatom Frustules

The particle size distributions of the as-received and heat-treated natural diatom frustules (900 and 1200 °C) before ball milling and after ball milling are shown in Figures 5.4(a-c), respectively. BB and AB in the same figures refer to before ball milling and after ball milling, respectively. The particle sizes of powders before ball milling range 1-100 μm and ball milling shifts the particle distribution to lower particle sizes, as seen in the same figures. For example, 90% of the sizes of the as-received natural diatom frustules is less than 44.4 μm, 50% less than 15.6 μm and 10% less than 3.8 μm before ball milling (see Table 5.3). After ball milling, these values were almost reduced to half and sequentially 20.9, 7.2 and 1.9 μm. Similar size reductions are also seen in the heat-treated frustules as shown in Figures 5.4(b) and (c). The mean particle sizes of the powders with the heat-treatment temperature before and after ball milling are depicted in Figure 5.4(d), together with the percent crystallinity. As is seen in the same figure, the mean particle sizes before and after ball milling tend to decrease slightly with increasing heat treatment temperatures. The mean particle size of the as-received frustule decreases from 15.6 μm to 14.7, 14.5, 14.4, and 13.7 μm after heat-treatment sequentially at 900, 1000, 1100, and 1200 °C and from 7.2 μm sequentially to 7.6, 7.6, 7.4, and 6.7 μm after ball milling. Percent crystallinity, on the other side, increases from 9.2% at room temperature to 19.9, 33.5, 38.7 and 46.2% after the heat-treatment at 900, 1000, 1100, and 1200 °C, respectively.

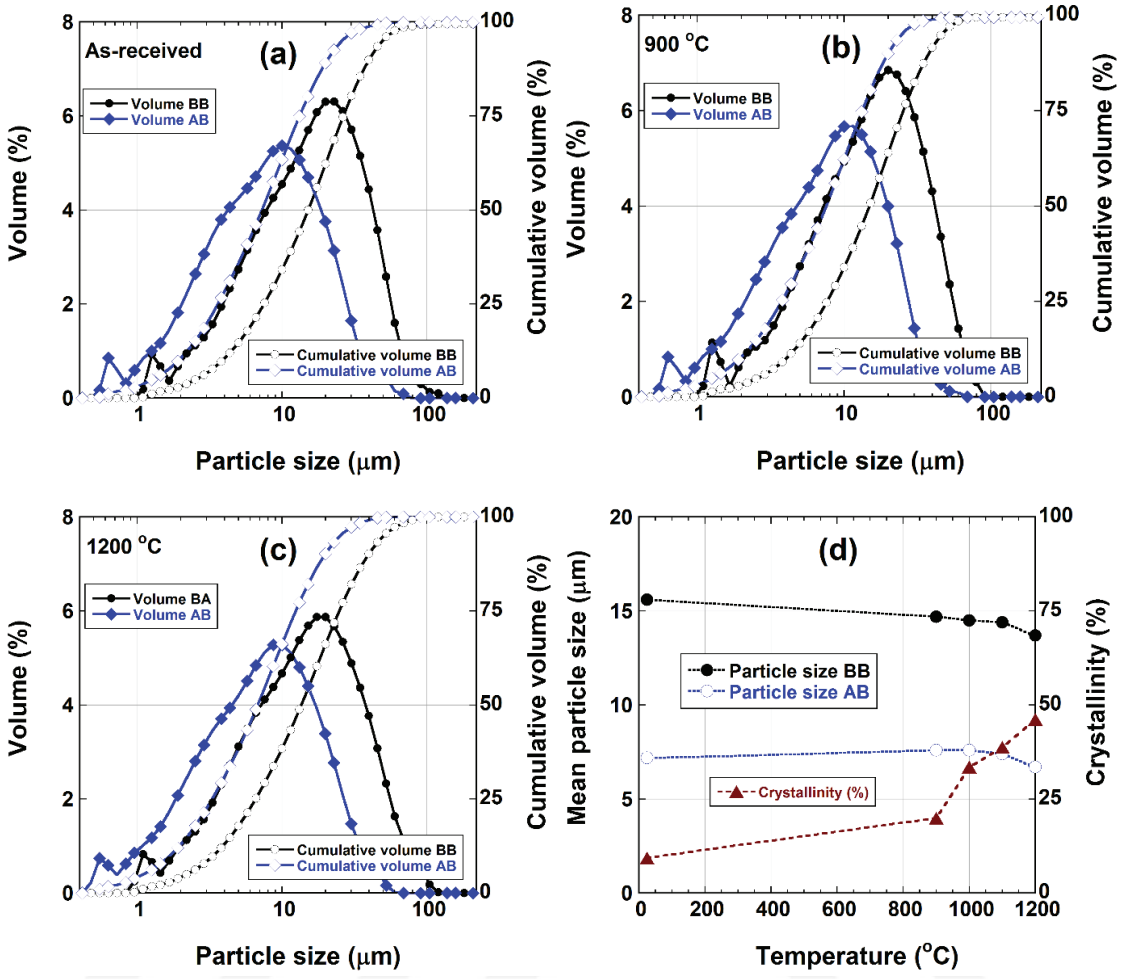

Figure 5.4. Effect of ball milling on the particle size (a) as-received and heat-treated frustules at (b) 900 and (c) 1200 °C and (d) variation of mean particle size and crystalline with the heat treatment temperature.

Table 5.3. Particle size distribution of as received and heat-treated natural diatom frustules (500 rpm 1 h ball milling).

Frustule	Ball milling time (h)	D(0.1) (μm)	D(0.5) (μm)	D(0.9) (μm)
25 °C (as-received)	0	3.8	15.6	44.4
	1	1.9	7.2	20.9
900 °C	0	3.7	14.7	38.9
	1	1.9	7.6	20
1000 °C	0	3.6	14.5	39.1
	1	1.9	7.6	20
1100 °C	0	3.5	14.4	40.2
	1	2	7.4	18.7
1200 °C	0	3.3	13.7	41.4
	1	1.6	6.7	20.7

5.3. Hydrochloric Acid Leaching

Figures 5.5(a and b) illustrate the particle size distribution of 10% (3.18 N) and 20% (6.36 N) HCl (100 ml) acid leached frustules heat treated at 25, 900, 1000, 1100 and 1200 ºC, respectively. The powder sizes corresponding to D0.1, D0.5 and D0.9 of HCl-treated frustules are further tabulated in Table 5.4, together with the heat-treatment temperatures. With the increase of the heat treatment temperature from 25 to 1200 °C, the mean powder size decreases from 14.2 to 10.6 µm after leaching with 10% HCl solution and from 12.5 µm to 9.5 µm after leaching with 20% HCl solution. As shown in Figures 5.6(a and b), the mean particle size of the as-received and heat-treated frustules is almost reduced to half by applying ball milling and the values are tabulated in Table 5.5.

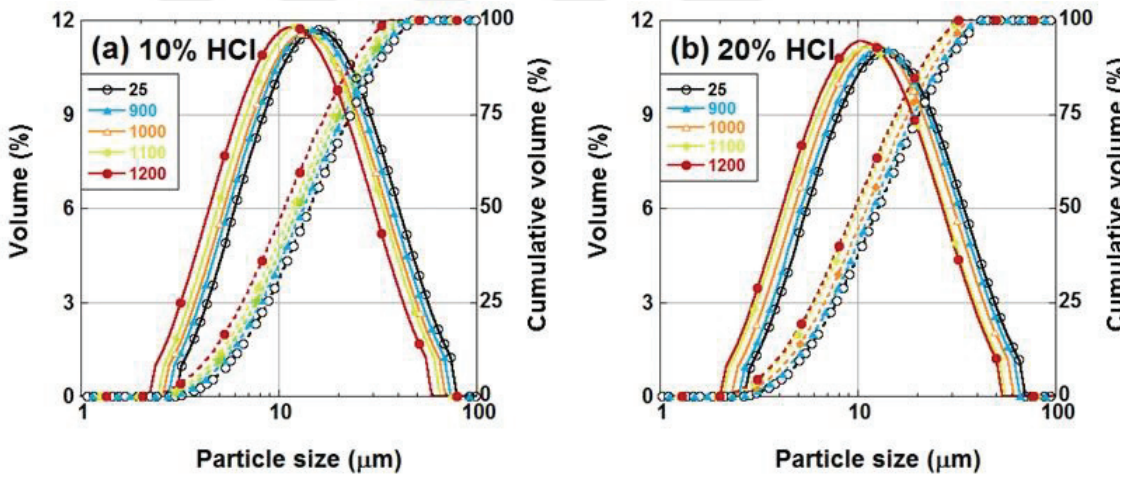

Figure 5.5. The particle size distribution of (a) 10% (3.18 N) and (b) 20% (6.36 N) HCl (100 ml) acid leached frustules heat-treated at 25, 900, 1000, 1100 and 1200 ºC.

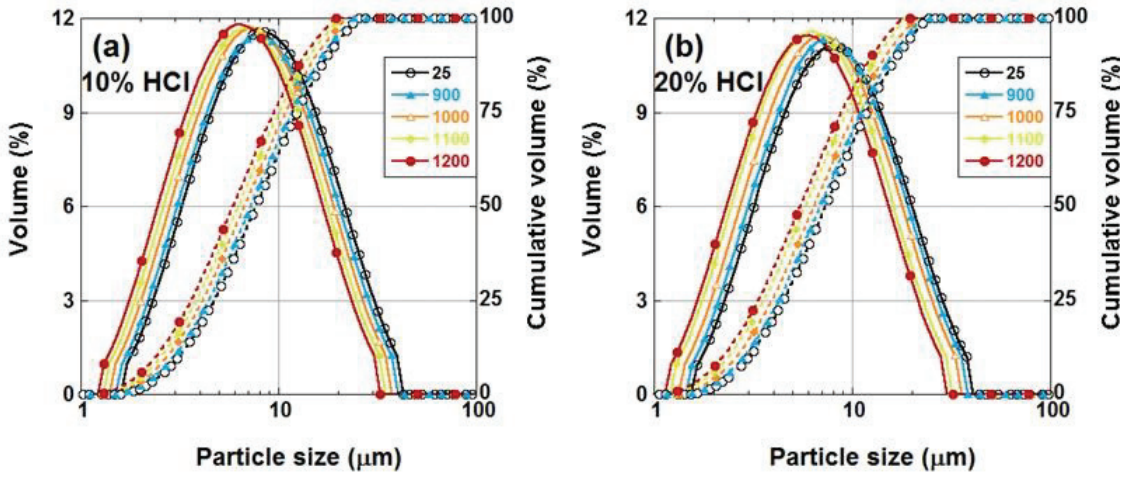

Figure 5.6. The particle size distribution of (a) 10% (3.18 N) and (b) 20% (6.36 N) HCl (100 ml) acid leached and ball milled (500 rpm , 1 h) frustule heat treated at 25, 900, 1000, 1100 and 1200 ºC.

Table 5.4. The particle size distribution of 10% HCl acid leached diatom frustules.

Samples	Particle size distribution					
10% (3.18 N) HCl	No ball milling			500 rpm, 1 h ball milling		
	D (0.1) nm	D (0.5) nm	D (0.9) nm	D (0.1) nm	D (0.5) nm	D (0.9) nm
25 °C (as-received)	5.9	14.2	31.4	3.3	7.5	18.4
900 °C	5.6	13.4	39.9	2.9	7.4	17.1
1000 °C	5.1	12.7	28.2	2.8	6.8	15.5
1100 °C	4.8	11.8	26.8	2.6	6.4	14.9
1200 °C	4.2	10.6	25.4	2.5	5.8	13.7

Table 5.5. The particle size distribution of 20% HCl acid leached diatom frustules.

Samples	Particle size distribution					
20% (6.36 N) HCl	No ball milling			500 rpm, 1 h ball milling		
	D (0.1) nm	D (0.5) nm	D (0.9) nm	D (0.1) nm	D (0.5) nm	D (0.9) nm
25 °C (as-received)	5.3	12.5	29.6	3.1	7.1	17.1
900 °C	4.8	12.1	28.7	2.9	6.8	16.3
1000 °C	4.5	11.5	25.9	2.7	6.4	14.4
1100 °C	4.3	10.0	23.5	2.6	5.8	13.7
1200 °C	3.4	9.5	22.3	2.3	5.3	12.7

The weight percentage of dissolved and undissolved under-filter frustules is shown in Figure 5.7 as a function of the heat-treatment temperature and acid concentration. About 12% of the as-received frustule passes under filter after 10% (3.18 N) HCl acid leaching and this value increases to ~14% when the acid concentration increases to 20% (6.36 N). The effect of heat-treatment is also seen on the weight of the under-filter frustule. For example, leaching 900 °C heat-treated frustules at 10% (3.18 N) HCl increases the under filter weight from ~13% to ~15%. In the under filter solution with 10% (3.18 N) HCl acid leaching, undissolved frustule particles were weighed after sequential washing and drying and ~8% of the as-received frustule, ~9% of the frustule heat-treated at 900 °C, ~11% of the frustule heat-treated at 1000 °C, ~13% of the frustule heat-treated at 1100 °C and ~18% of the frustule heat-treated at 1200 °C were found not dissolved in the under filter solution.

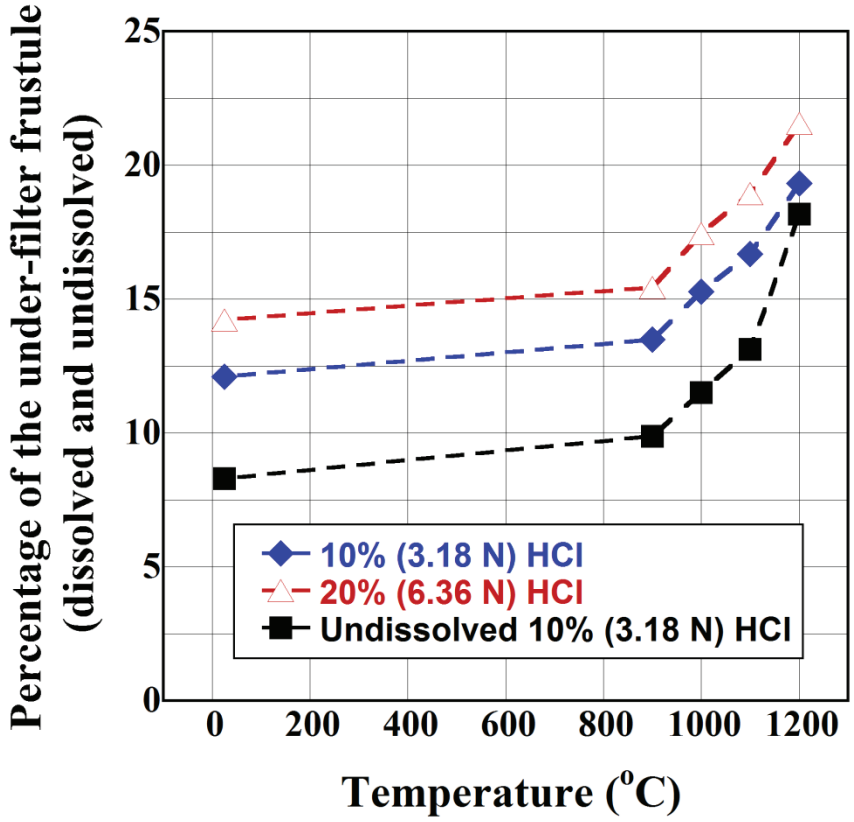

Figure 5.7. The weight percentage of dissolved and undissolved under-filter frustules.

5.4. Hydrofluoric Acid Leaching

Figures 5.8(a-e) demonstrate the XRD spectra of the filtered frustules heat-treated at 25, 900, 1000, 1100 and 1200 ºC using 1 N, 3 N, 5 N, and 7 N solution for 15 min and the percentage of the crystalline silica, respectively. The increased peak intensities at increasing heat-treatment temperatures in the same figures refer to the increased crystallinity. Both HF-leaching and heat treatment are seen, in the same figures, effective in increasing the crystallinity. For example, the percentage of crystal phase of natural frustule (Figure 5.8(f)) increases from 9.2% to about 12, 29, 35 and 42% when leached sequentially by 1, 3, 5, and 7 N HF solution for 15 min. This also confirms a higher rate of amorphous phase dissolution with acid leaching of the as-received frustule. On the other side, the increased percent crystallinity of heat-treated frustule without HF-leaching shows a further increase after acid leaching (Figure 5.8(f)). The crystal phase percentage of the filtered acid leached frustules also increases with increasing acid concentration; the crystallinity reaches 50-60% when the acid concentration is increased to 7 N as seen in Figure 5.8(f).

Figures 5.9(a-h) show the XRD spectra of the filtered frustules leached with 1, 3, 5 and 7 N solution by 15, 30 and 60 min acid leaching, respectively. The percentage of crystal phase of natural frustule increases from 9.2% to about 12, 27 and 36% when leached sequentially by 1 N HF solution at 15, 30, and 60 min, respectively. The crystal phase percentage of the filtered acid leached frustules also increases with increasing leaching times; the crystallinity reaches ~60% when the acid concentration is increased to 7 N for 60 min in 900 ºC heat-treated frustules.

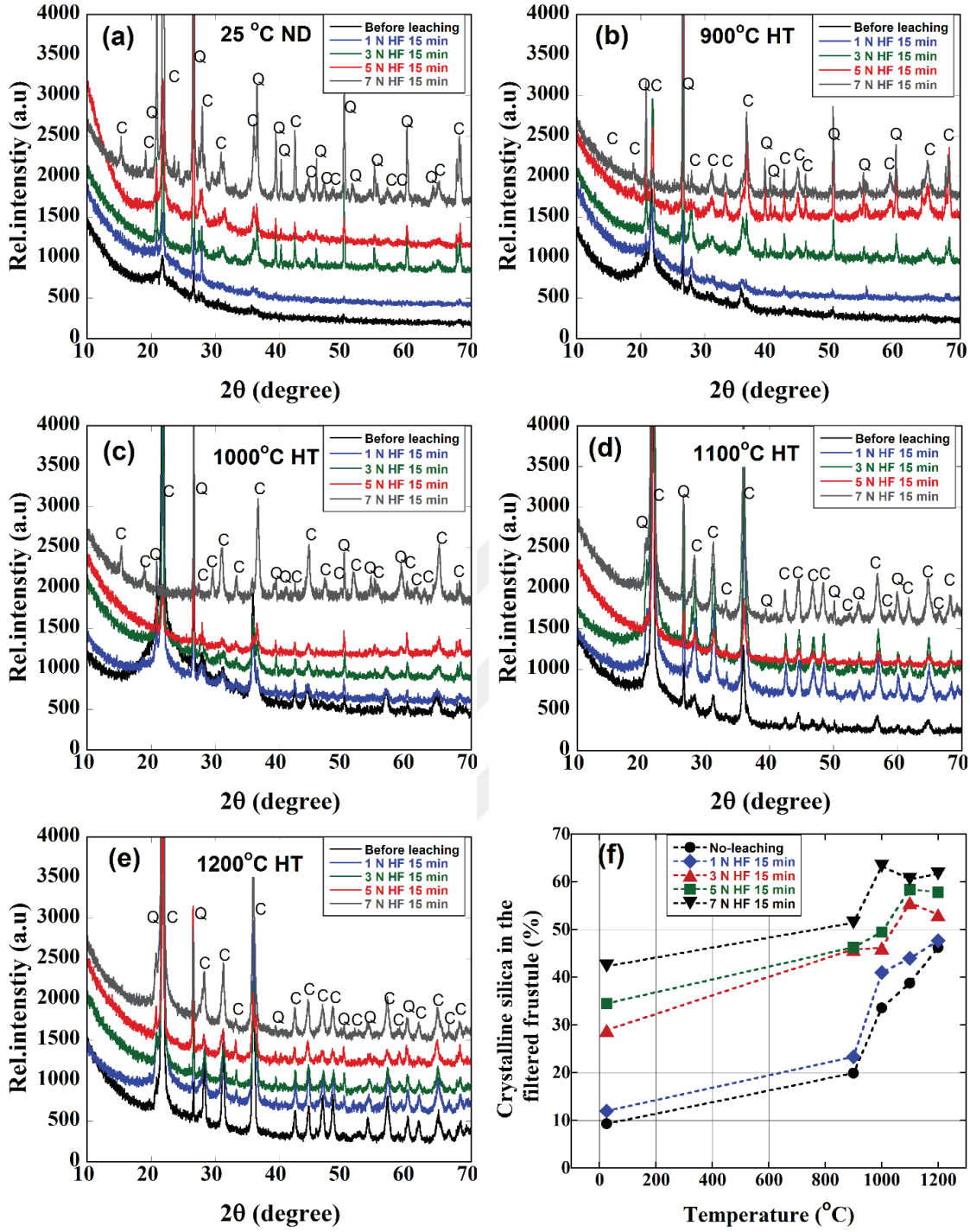

Figure 5.8. XRD spectra of the filtered frustule heat-treated at (a) 25 ºC, (b) 900 ºC, (c) 1000 ºC, (d) 1100 ºC, and (e) 1200 ºC (1 N, 3 N, 5 N, and 7 N 15 min) (Q: Quartz, C: Cristobalite) and (f) the percentage of the crystalline silica.

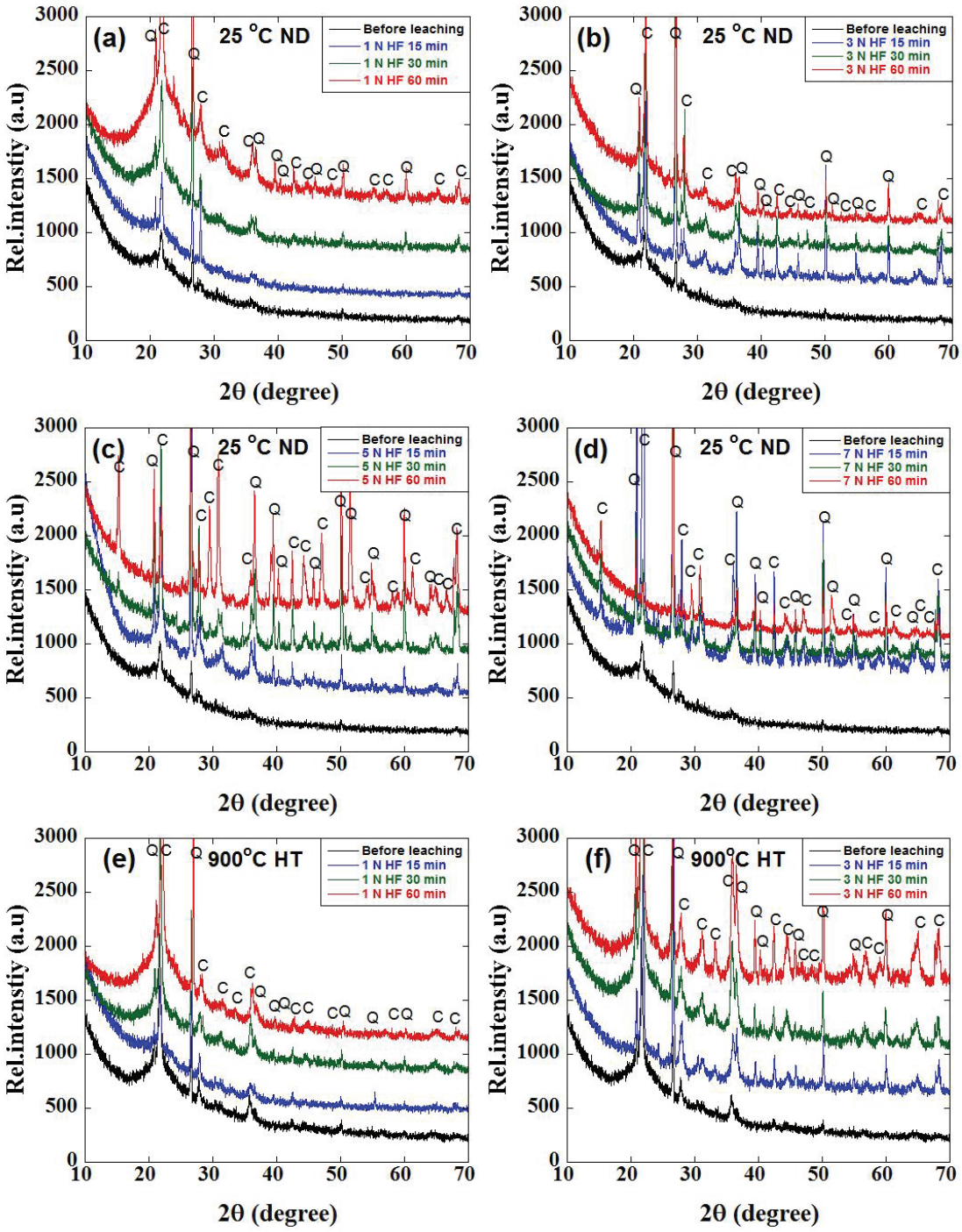

(cont. on next page)

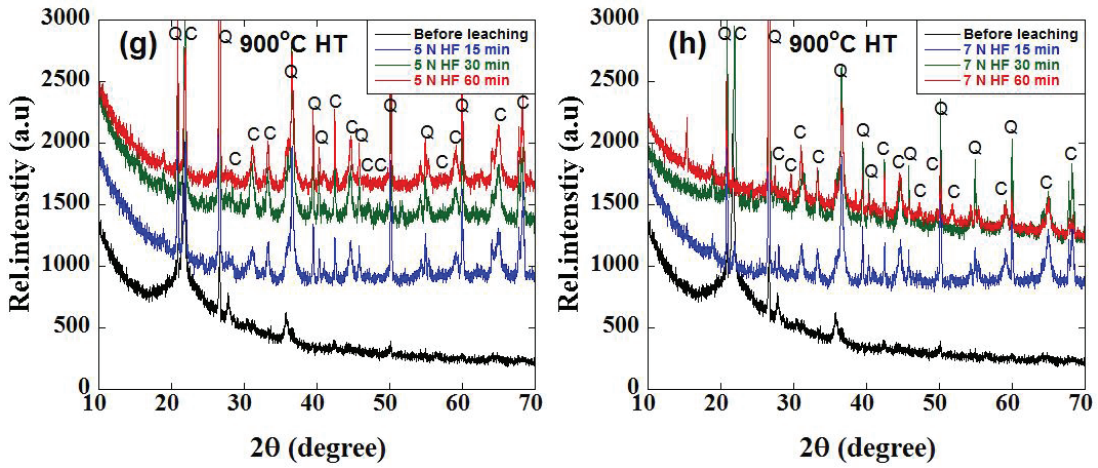

Figure 5.9. XRD spectra of the filtered frustule at (a) 1 N, (b) 3 N, (c) 5 N and (d) 7 N (15, 30 and 60 min) acid leached as-received and (e) 1 N, (f) 3 N, (g) 5 N and (h) 7 N (15, 30 and 60 min) acid leached 900 ºC heat-treated frustules.

The weight percentage of dissolved and undissolved under-filter frustules are shown in Figure 5.10(a) as function of the heat-treatment temperature and acid concentration for 15 min leaching. A strong dependence of the under filter frustule weight percentage on the acid concentration is evident in the same figure; for example, 38% of the as-received frustule passes under filter after 1 N HF acid leaching and this value increases to 85% when the acid concentration increased to 7 N. The effect of heat-treatment is also seen in the weight of the under filter frustule. For example, leaching 900 °C heat-treated frustules at 1 N HF for 15 min increases the under filter weight from 38% to 59%, while heat treatment above this temperature decreases the weight of the under filter frustule, even below that of the as-received frustule in 1100 and 1200 °C heat-treated frustules. In the under filter solution with 1 N HF 15 min leaching, undissolved frustule particles were weighed after sequential washing and drying and ~25% of the as-received frustule, ~39% of the frustule heat-treated at 900 °C and 2.64% of the frustule heat-treated at 1200 °C were found not dissolved in the under filter solution. The effect of the starting frustule weight (1000, 3000, and 5000 mg) on the weight percentage of dissolved and undissolved under-filter frustules for the as-received frustule is shown in Figure 5.10(b). As seen in the same figure, more than 80% of the starting as-received frustules pass under filter at 3, 5 and 7 N HF solutions when the weight of the starting frustule is 1000 mg, while increasing the weight of the starting frustule decreases the weight percentage under filter frustules. The leaching experiments were continued using a 3000 mg starting frustule weight.

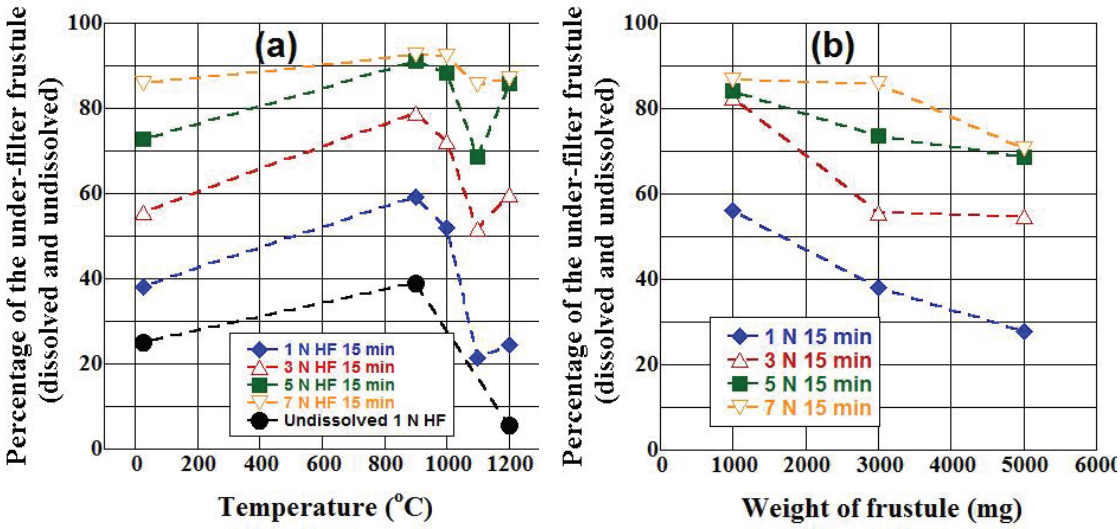

Figure 5.10. The weight percentage of dissolved and undissolved under-filter frustules (a) at different heat treatment temperatures and acid concentrations (3000 mg) and (b) the effect of the weight of starting frustule.

The effect of leaching time on the percentage of the under-filter frustule is shown in Figures 5.11(a) and (b) for the as-received and 900 °C heat-treated frustules, respectively. Increasing leaching time from 15 to 30 min increases the percentage of the under filter as-received frustules (Figure 5.11(a)). After 30 min, the percentage however reaches a steady value, 90% or over. The percentage of the under filter of the 900 °C heat-treated frustules, as seen in Figure 5.11(a) is over 90%, when leached by 5 and 7 N HF solution. As is noted in the same figure, the heat-treated frustule shows lesser passage to under filter in 1 and 3 N HF solution leaching. The percent crystalline phase in the filtered frustule also increases with increasing leaching time regardless of acid concentration, as depicted in Figure 5.11(b). This proves a higher rate of passage of amorphous phase to under filter.

Figures 5.12(a-e) show the SEM pictures of an as-received 1N HF-leached (15 min) frustule at five different magnifications. The shallow small-size pits seen on the ridges of regular circular holes as marked by the arrows in Figures 5.12(d) and (e) are likely due to the dissolution or separation of nano-silica particles by acid leaching. The number and size of these surface pits increase significantly in the 1N HF leached (15 min) 900 °C heat-treated frustules as clearly seen in the SEM pictures in Figures 5.13(a-e). These are also consistent with the increased weight percentage of the under filter frustules in the 900 °C heat-treated frustule (59%) as compared with the as-received frustules (39%), as also noted in Figure 5.10(a). Gradually, the size and number of the surface pits

decrease when the heat-treatment temperature increases to 1000 and 1100 °C as seen in Figures 5.14(a-e) and Figures 5.15(a-e), respectively. The weight percentages of the under filter frustules also decrease to ~52% and ~21% for 1000 and 1100 °C heat treatments, respectively. The cracks seen on the surface of frustules (Figure 5.15(e) confirms the increased rates of crystal phase transformation at these temperatures. Note that in Figure 5.15(e) and Figure 5.14(e), the pit sizes are smaller in the 1100 °C heat-treated frustules than the 1000 °C heat-treated frustules. This is in accord with lower percentages of under filter frustules of 1100 °C heat-treated frustules than that 1100 °C heat-treated frustules. On the other side, large crystal grains are seen after 1 N HF leaching for 15 min in the frustules heat-treated at 1200 °C, Figures 5.16(a-e). At the same time, the percentage of under filter in these frustules (~24%) is very much similar with the frustules heat-treated at 1100 °C.

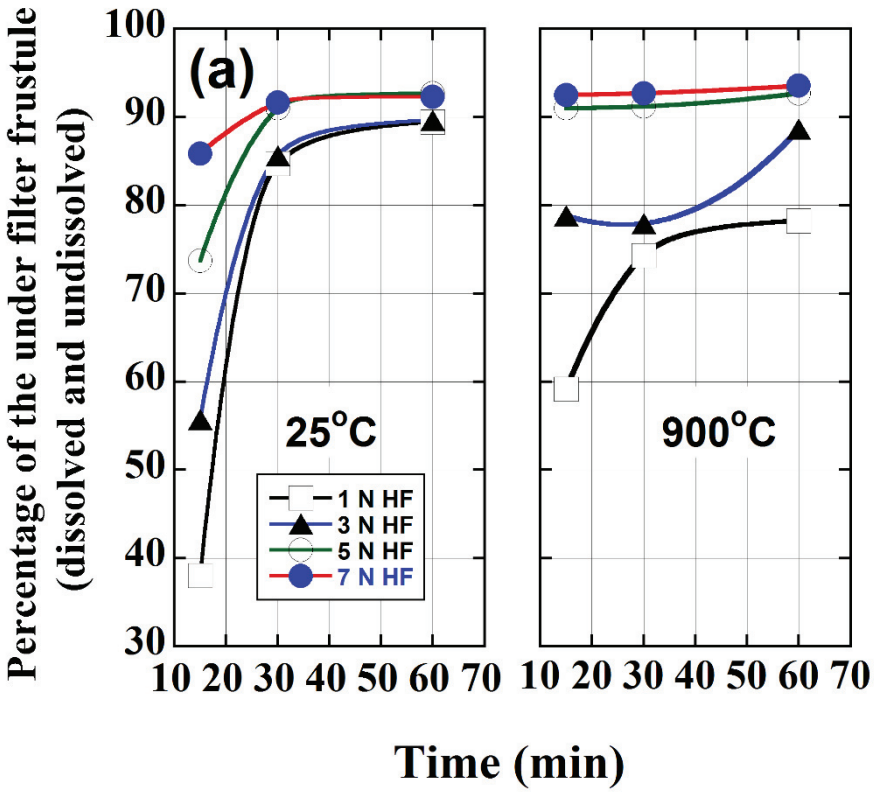

(cont. on next page)

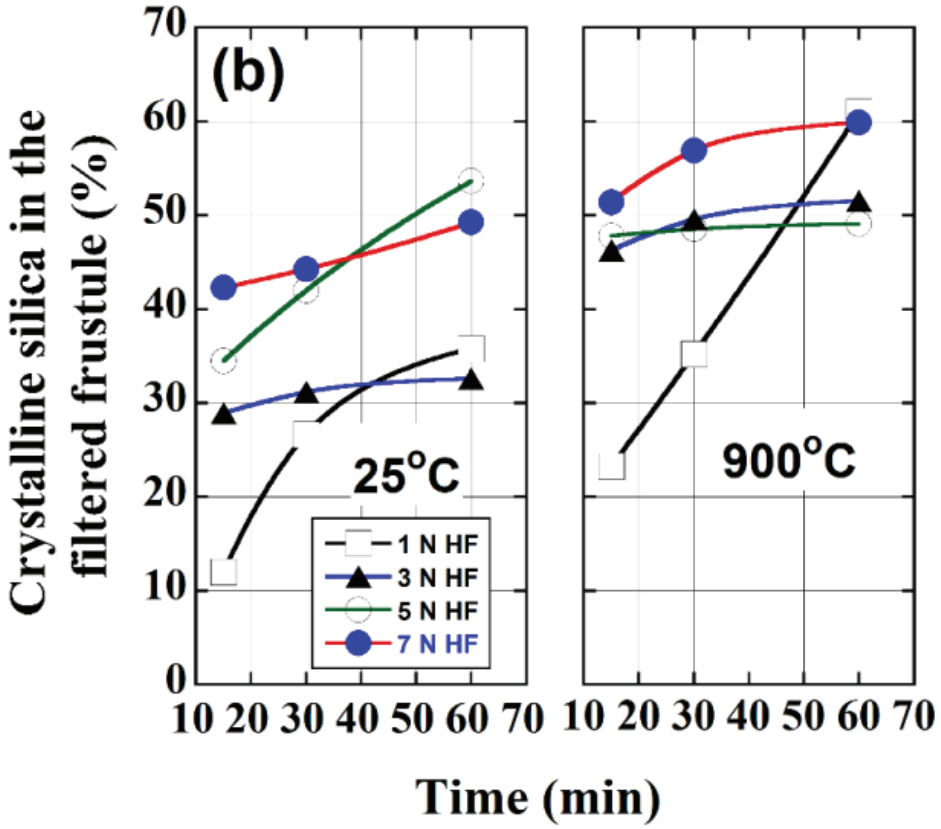

Figure 5.11. (a) The weight percentage of under-filter and (b) the crystallinity in the filtered as-received and 900 °C heat-treated frustules leached at different acid solutions for 15, 30 and 60 min.

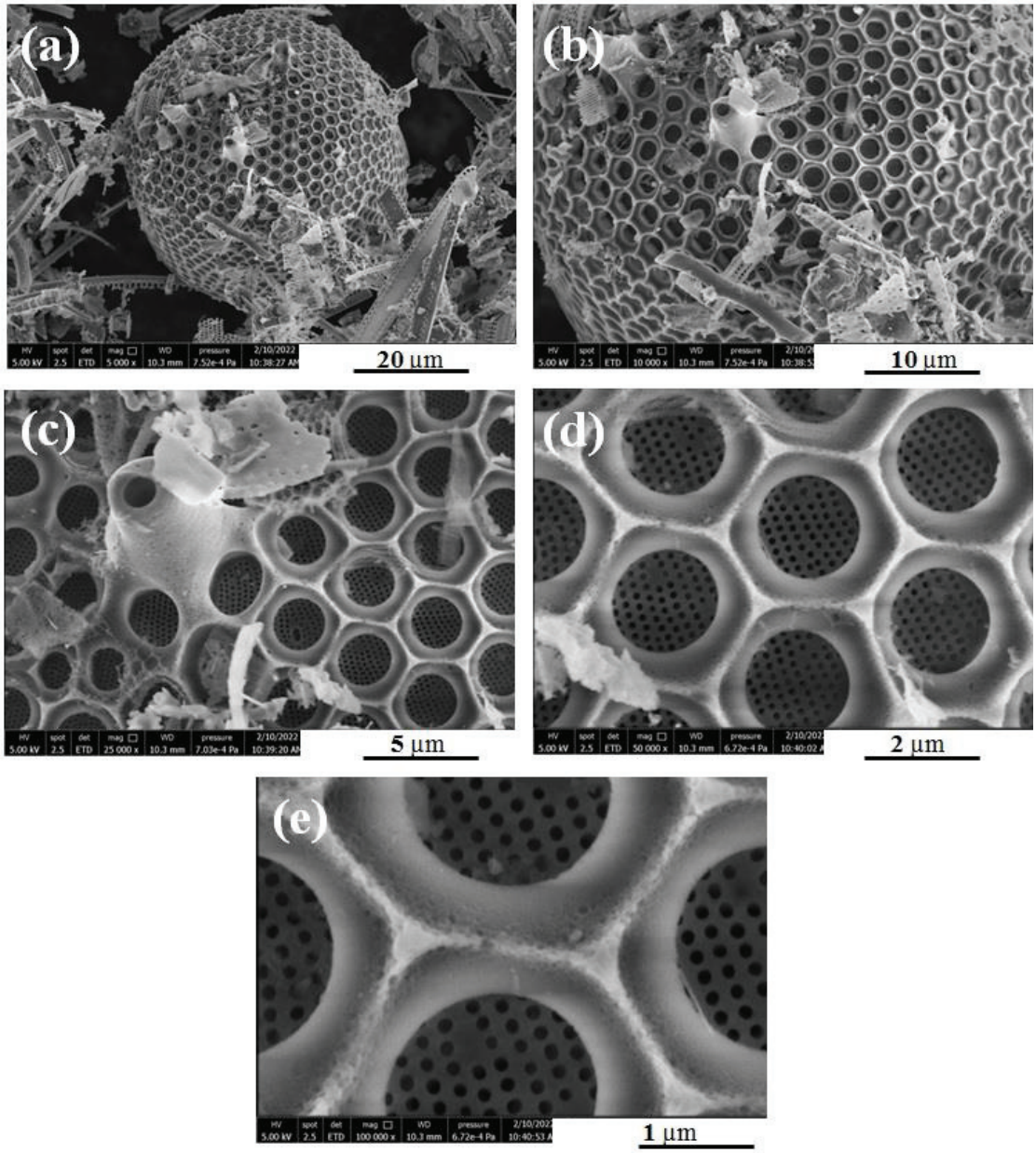

Figure 5.12. The SEM pictures of the as-received frustules 1N HF-treated (15 min) showing the structure (a,b) low, (c) intermediate and (d,e) high magnification.

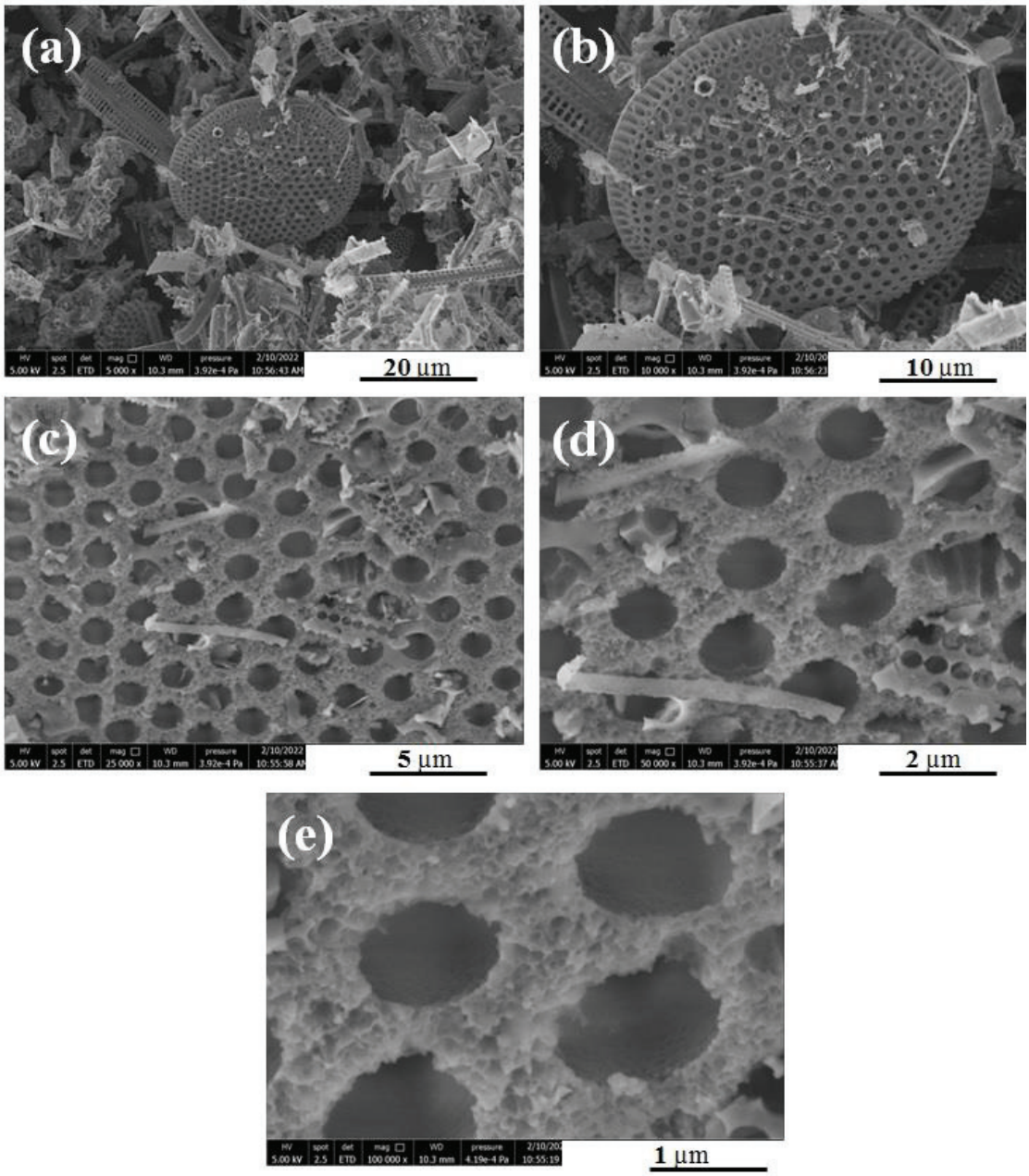

Figure 5.13. The SEM pictures of the 900 °C heat and 1N HF-treated (15 min) showing the structure (a,b) low, (c) intermediate and (d,e) high magnification.

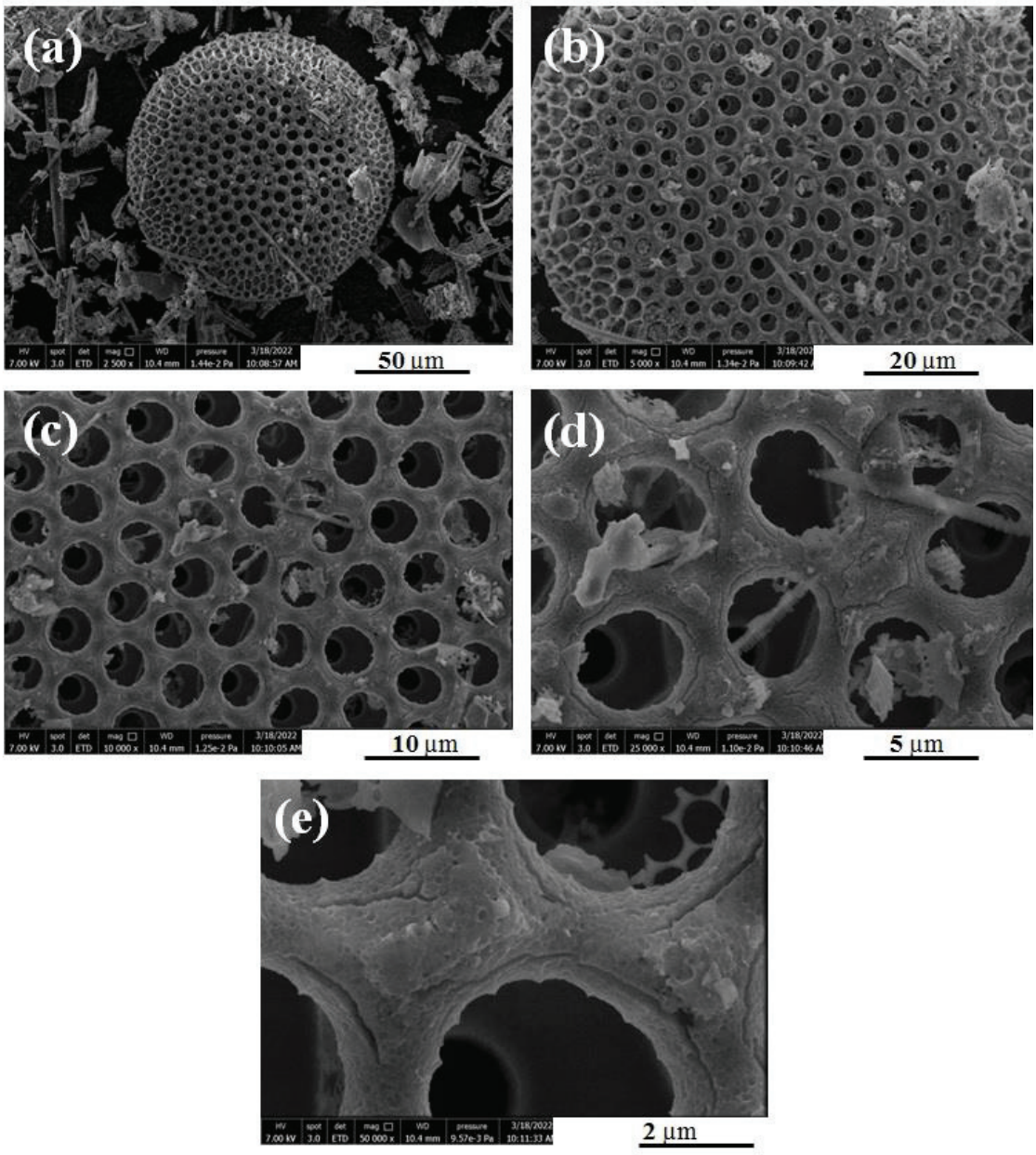

Figure 5.14. The SEM pictures of the 1000 °C heat and 1N HF-treated (15 min) showing the structure (a,b) low, (c,d) intermediate and (e) high magnification.

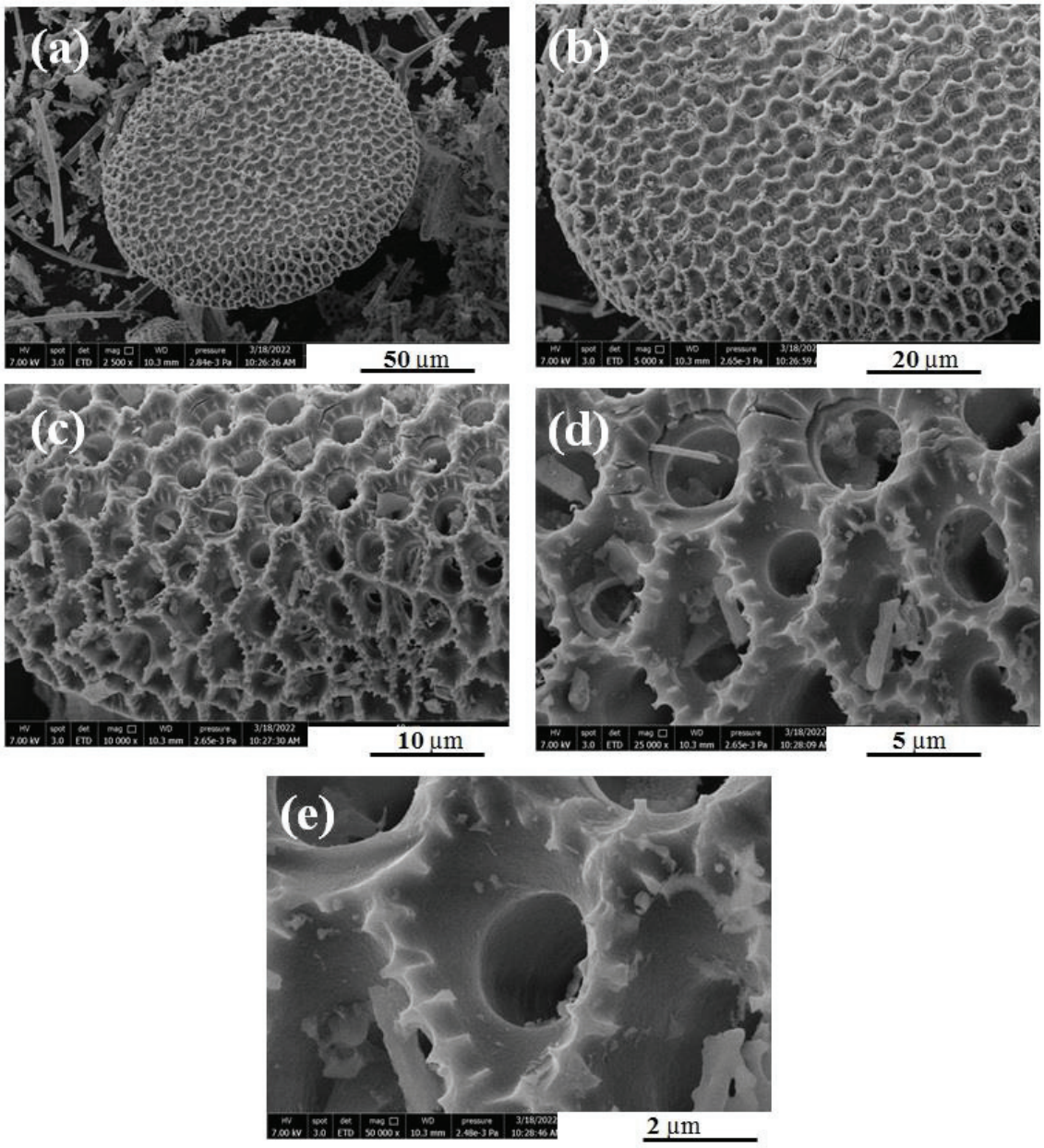

Figure 5.15. The SEM pictures of the 1100 °C heat and 1N HF-treated (15 min) showing the structure (a,b) low, (c,d) intermediate and (e) high magnification.

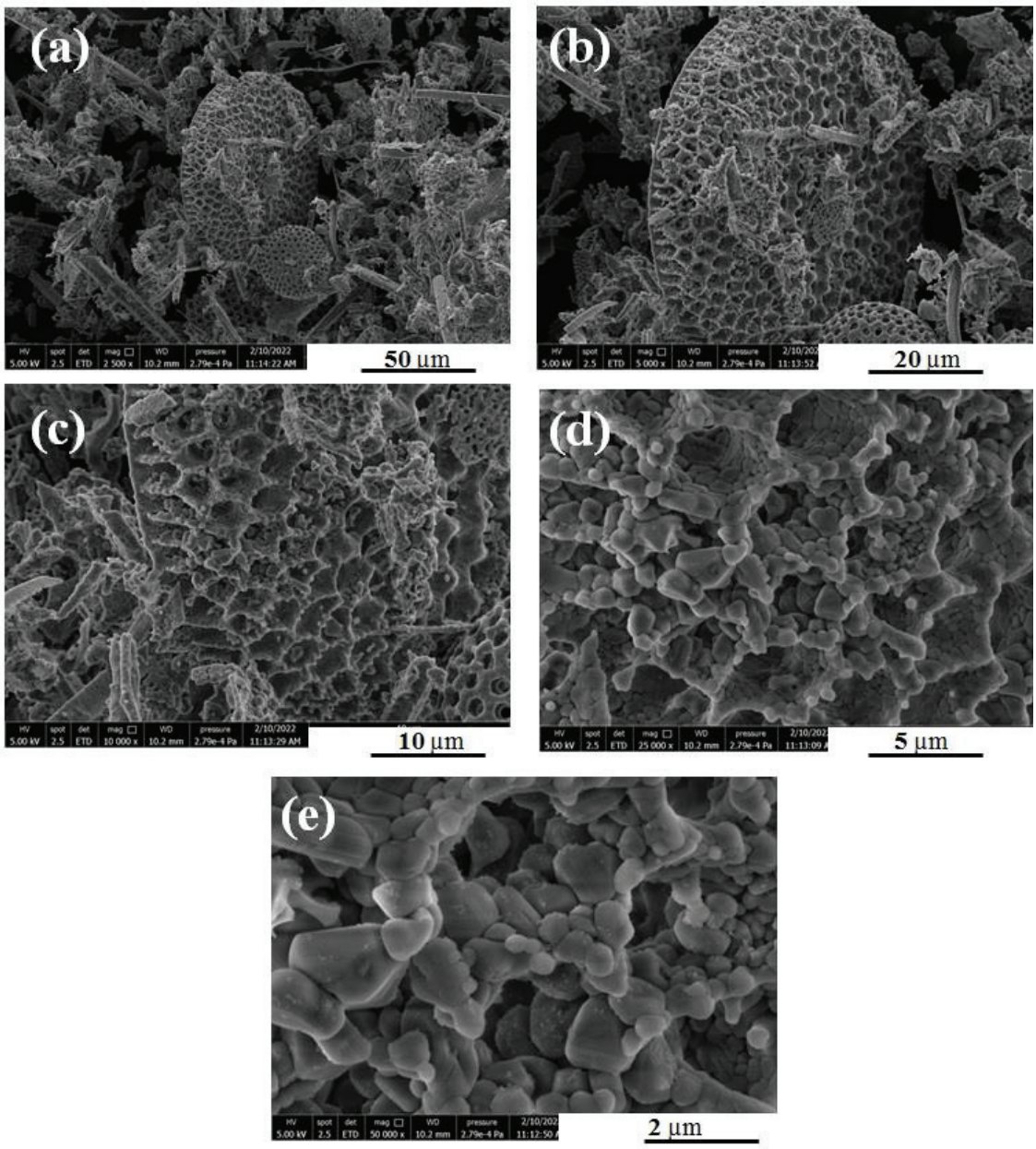

Figure 5.16. The SEM pictures of the 1200 °C heat and 1N HF-treated (15 min) showing the structure (a,b) low, (c,d) intermediate and (e) high magnification.

The pictures of silica powders after ball milling acid-leached and filtered as-received and 900, 1000, 1100 and 1200 °C heat-treated frustules are shown sequentially in Figures 5.17(a-e). The powders are composed of both small and large nano size particles, while smaller particle size is notable in the powders obtained from heat-treated frustules as seen in the same pictures. The particle size distribution and cumulative volume curves of the powders are shown in Figure 5.17(f). As the heat-treatment temperature increases, the mean particle size decreases and the particle distribution becomes narrower. The powder sizes corresponding to D0.1, D0.5 and D0.9 of the ball milled HF-treated frustules are further tabulated in Table 5.6, together with the heat-treatment temperature and the corresponding percent crystallinity. With the increase of the heat treatment temperature from 25 to 1200 °C, the mean powder size decreases from 774 nm to 547 nm and the crystallinity increases from 12% to 48%. Figure 5.18(a) shows the pictures of the ball milled acid-leached and heat-treated frustules. The color of the as-received frustule is light gray, while the heat-treatment changes the color into light brown. The color does not change with acid leaching and ball milling. The color change is likely due to the oxidation of iron oxide into Fe_2O_3 during the open-air heat-treatment process. Also, the XRD spectrum of the filtered and ball milled frustule is illustrated in Figure 5.18(b). Crystallinity increases from 12% (as-received) to 48% 1200 °C heat-treated diatom frustules.

Table 5.6. The particle sizes of the ball milled HF-treated frustules (1 N HF 15 min + 500 rpm 1 h ball milling).

Frustule	D(0.1) (nm)	D(0.5) (nm)	D(0.9) (nm)	CR (%)
25 °C (as-received)	322	774	1794	12
900 °C	318	760	1785	23
1000 °C	287	668	1494	41
1100 °C	316	644	1291	44
1200 °C	268	547	719	48

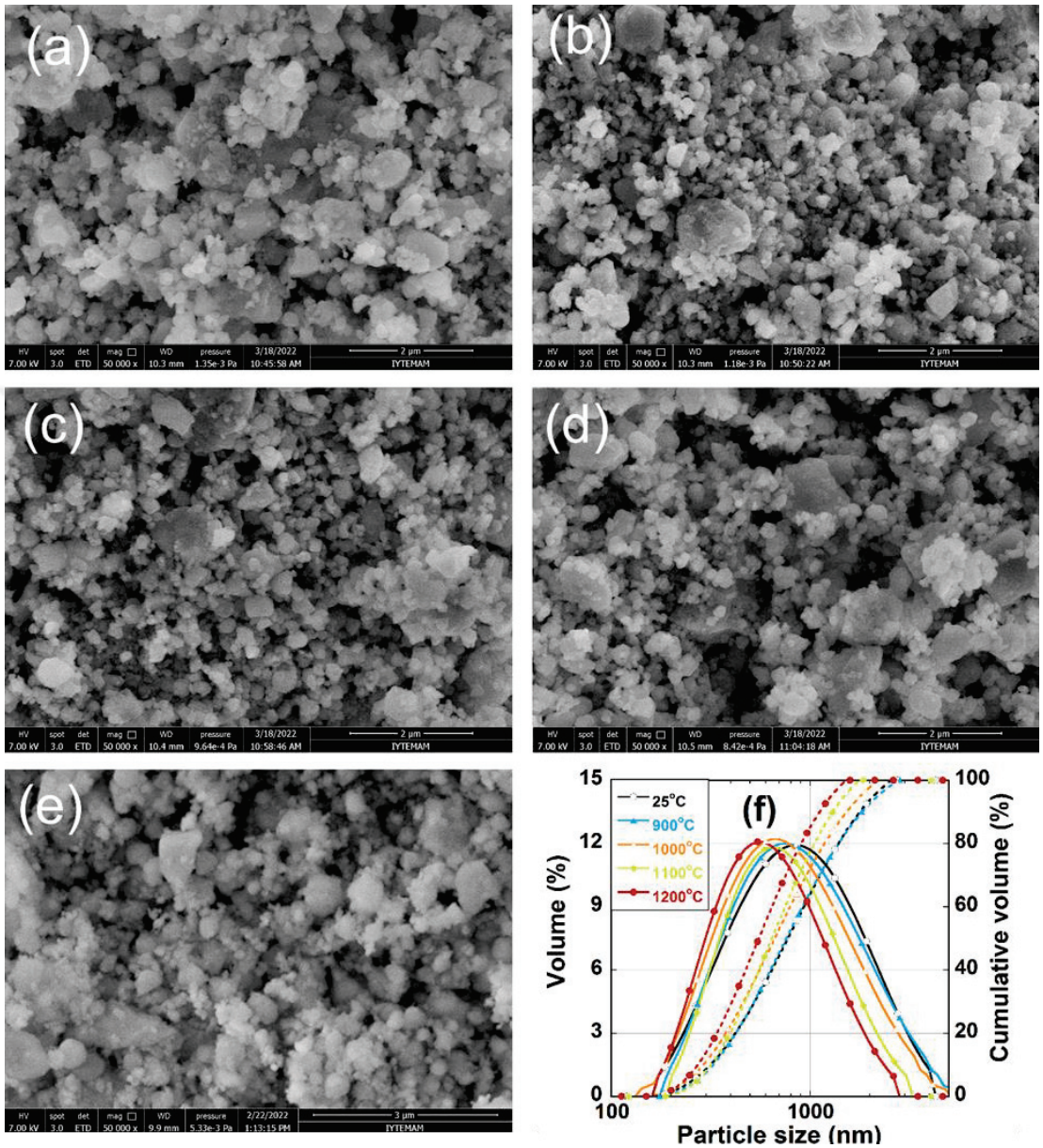

Figure 5.17. The SEM pictures of the 1N HF-treated (15 min) and ball milled (500 rpm 1 h) frustule powders (a) as-received and heat-treated at (b) 900, (c) 1000, (d) 1100 and (e) 1200 °C low and (f) particle size distribution.

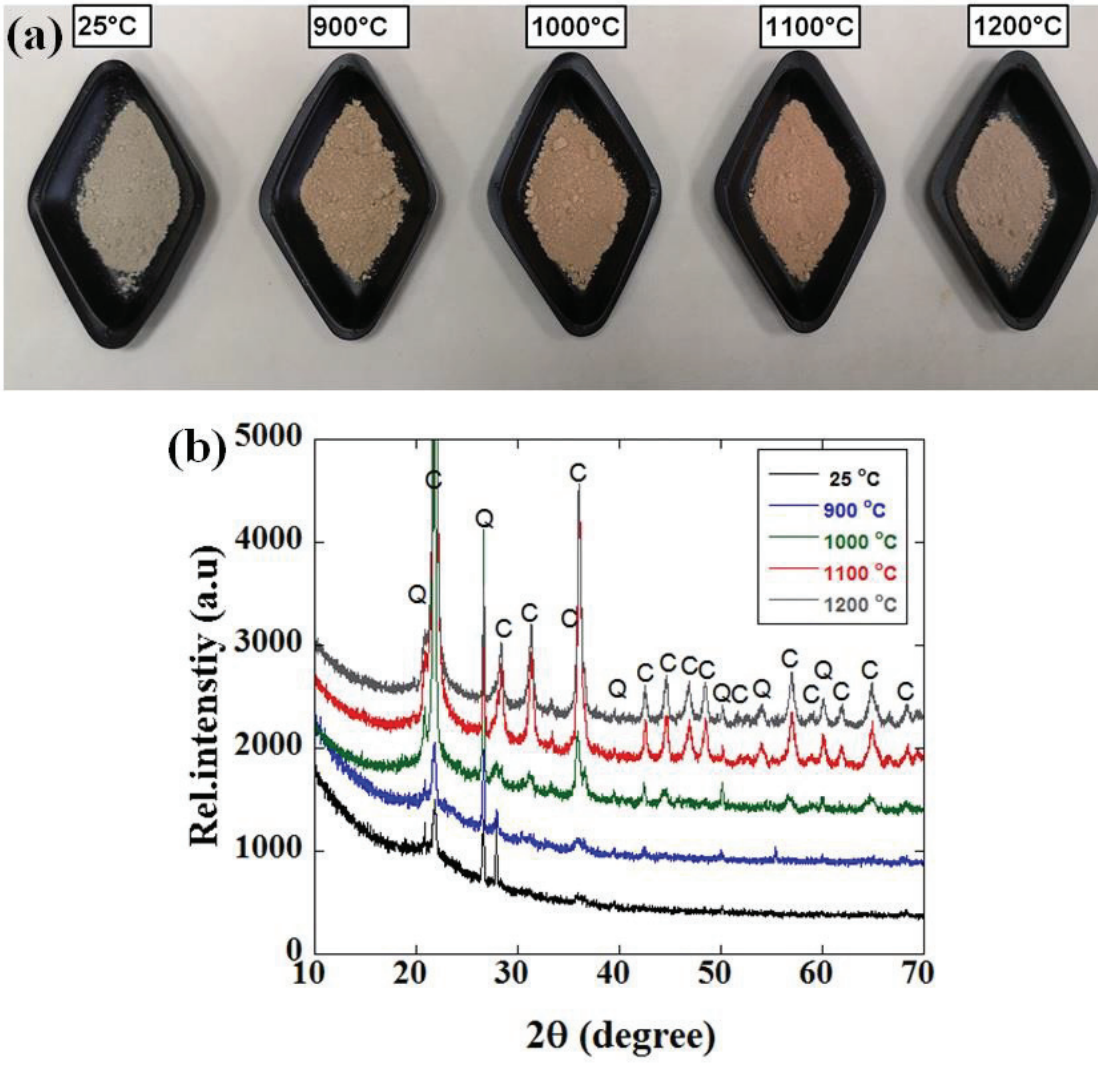

Figure 5.18. (a) The pictures of the heat-treated, acid leached (1 N), ball milled frustule powders and (b) XRD spectrum of frustule powders (Q: Quartz, C: Cristobalite).

The effects of acid leaching and heat treatment on the mean particle sizes of the frustules are shown in Table 5.7. The mean particle size of the as-received and heat-treated frustules is almost reduced to half by applying ball milling (without acid leaching), while ball milling the filtered acid-leached frustules reduces the mean particle sizes significantly; the reduction is more than twenty times. Figure 5.19 shows the under filter frustule particle sizes of the as-received and 900 °C heat-treated frustules at increasing acid concentrations and the values are tabulated in Table 5.8, together with the percent frustules passing under filter. The mean particle size as seen in the same table is smaller in the frustules heat-treated at 900 °C than the as-received frustules. This proves a higher

reactivity of the frustules heat-treated at 900 °C to the HF leaching than as-received frustules. Table 5.9 tabulates the weights and weight percentages of the above and under filter acid leached frustules (3000 mg, 1 N HF 15 min). Although, a marginal effect of heat treatment temperature on the mean particle size is seen (Table 5.7), the weight percentages of the frustules passing under filter is significantly affected by the heat treatment temperature as tabulated in Table 5.9. The weight percentage of the under filter is higher in the frustules heat-treated at 900 °C than the as-received frustules. But the under filter weight percentage decreases significantly in 1100 and 1200 °C heat-treated frustules, ~21-25%. This is almost half that of the as-received frustules (38%) and 1/3 of the frustules heat-treated at 900 and 1000 °C (59-51%). As is noted, the highest amount of above-filter is seen in 1100 and 1200 °C heat-treated frustules and the lowest in 900 °C heat-treated frustules. The weight of the above filter as-received leached frustules is noted in the same table higher than those 900 and 1000 °C heat-treated frustules. Although the amount of crystal phase in 1000 °C heat-treated frustules are almost in the same order with 1100 and 1200 °C heat-treated frustules, the under filter weight percentage of 1000 °C heat-treated frustules is higher. The weight of dissolved frustules is noted to be very much similar for the all heat-treated frustules and lower than that of as-received powder. Note that 2-3 wt% of the under filter powder particles of 1100 and 1200 °C heat-treated frustules are undissolved in the HF solution. While, the highest undissolved under filter powder is obtained in 900 °C heat-treated frustules. The crystallinity of under filter not dissolved powder is also tabulated in the last column of Table 5.9. Except for the as-received frustules, the crystallinities of under filter powders of heat-treated frustules are lower than those of above filter acid leached frustules. This also confirms a higher rate of amorphous silica dissolution during acid leaching. While, the evaporation of under filter acid+water solution resulted in the formation of SiF_4 precipitates (seen in the XRD of under filter powder) (Figure 5.20).

Table 5.7. The mean particle sizes of the ball milled frustules without and with acid leaching (1 N HF 15 min + 500 rpm 1 h ball milling).

Frustule	(µm)	Ball milling (µm)	Acid leaching and ball milling (nm)	CR (%)
25 °C (as-received)	15.6	7.2	774	12
900 °C	14.7	7.6	760	23
1000 °C	14.5	7.6	668	41
1100 °C	14.4	7.4	644	44
1200 °C	13.7	6.7	547	48

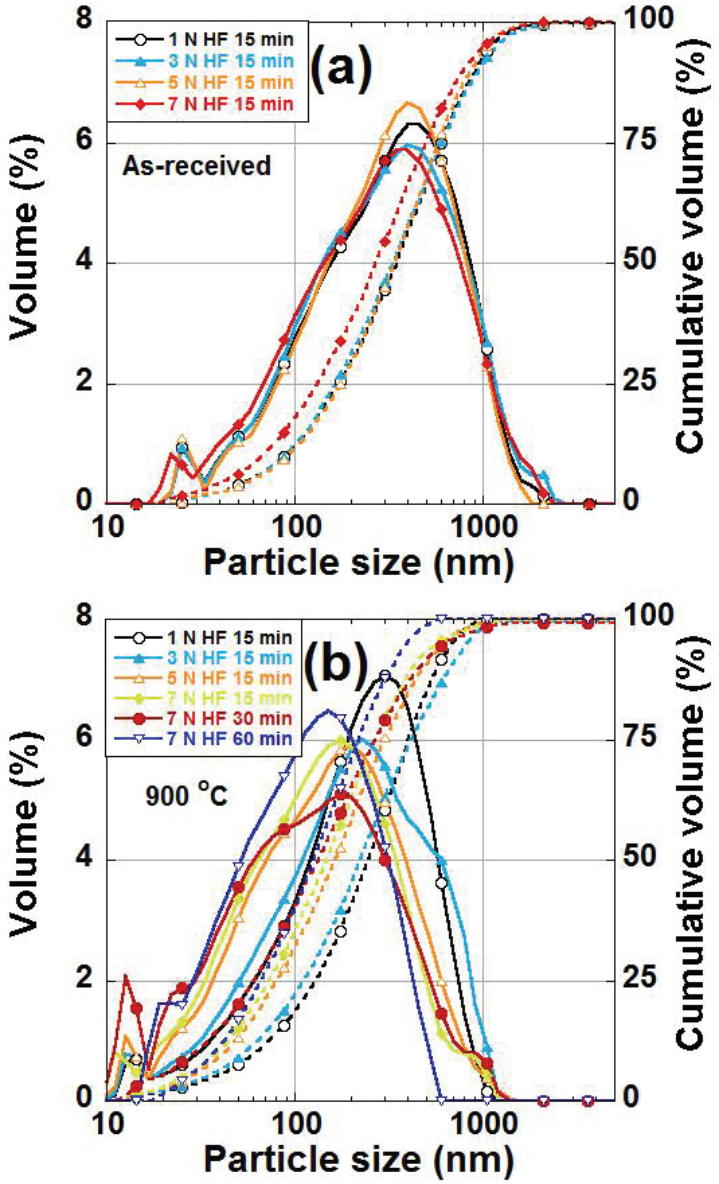

Figure 5.19. The under filter frustule particle sizes of the (a) as-received and (b) 900 °C heat-treated frustules at increasing acid concentrations.

Table 5.8. The particle sizes of the frustules powder of filter solution of as-received and 900 °C heat-treated frustules leaching with different concentration of HF and leaching times.

25°C (as-received)	D (0.1) (nm)	D (0.5) (nm)	D(0.9) (nm)	Under filter (%)
1N HF 15 min	105	347	870	38
3N HF 15 min	102	337	810	55
5N HF 15 min	100	325	768	75
7N HF 15 min	78	271	712	85
900 ºC	**D (0.1) (nm)**	**D (0.5) (nm)**	**D (0.9) (nm)**	**Under filter (%)**
1N HF 15 min	72	245	694	59
3N HF 15 min	66	221	539	80
5N HF 15 min	64	158	430	91
7N HF 15 min	56	145	416	93
7N HF 30 min	45	127	388	93
7N HF 60 min	38	111	275	94

Table 5.9. The weights and weight percentages of the above and under filter acid leached frustules (3000 mg, 1 N HF 15 min).

Heat treatment (°C)	Above filter (mg and %)	Under filter (mg and %)	Under filter not dissolved (mg and %)	Under filter dissolved (mg and %)	Under filter not dissolved powder CR (%)
25°C	1860 (62%)	1140 (38%)	769 (25.6%)	371 (12.4%)	13.71
900°C	1226 (40.85%)	1774(59.15%)	1177 (39.2%)	597 (19.95%)	15.27
1000°C	1442(48.05%)	1558 (51.95%)	935 (31.19%)	623 (20.76%)	19.45
1100°C	2355 (78.5%)	645 (21.50%)	99 (3.3%)	546 (18.2%)	33.20
1200°C	2265 (75.5%)	735 (24.5%)	79 (2.64%)	656 (21.86%)	35.46

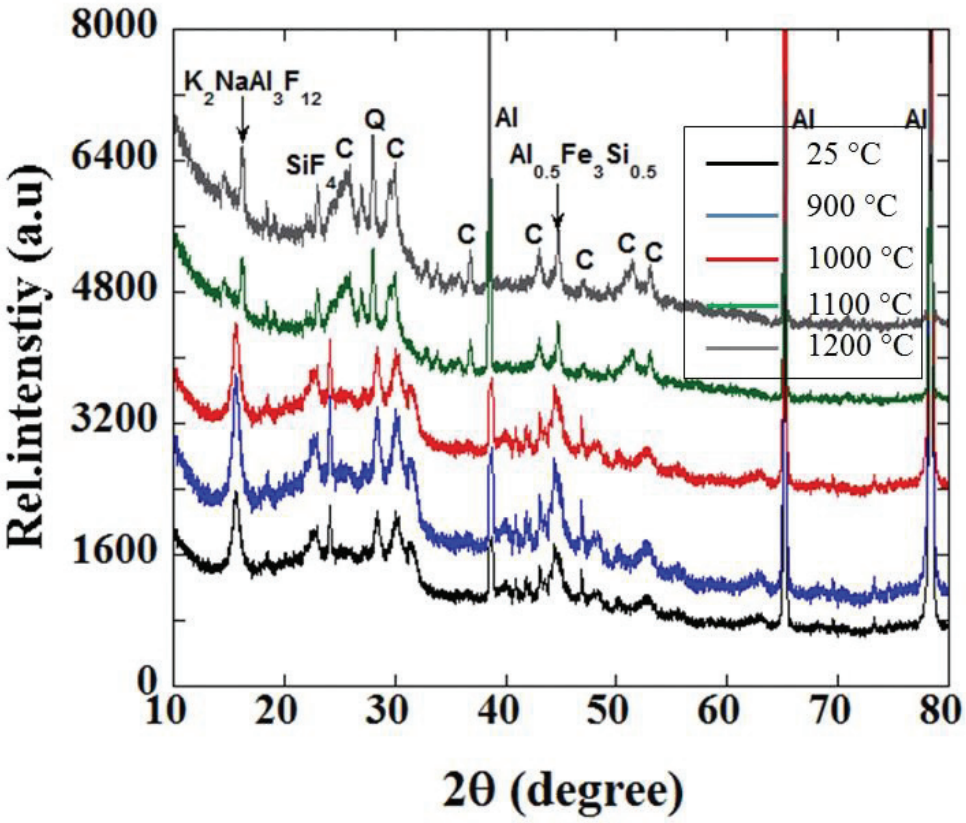

Figure 5.20. The XRD spectrum of under filter powder.

5.5. Mechanical Behavior of Nano-Structured Frustules Filled Epoxy

Figures 5.21(a-c) show the pictures of neat epoxy and 0.5, 1 and 2 vol% silica-epoxy composite tensile test specimens inside the Teflon mold, after curing at 50 °C for 24 h and after the tensile test, respectively. These specimens were prepared using the silica powders obtained by balling (500 rpm 1 h) HF-leached (1 N HF 15 min) 1200 °C heat-treated frustules. Three quasi-static stress-strain curves of neat epoxy and 0.5, 1 and 2 vol% of silica-epoxy composites are shown together in Figure 5.22. The tensile stress-strain curves in the same figure are seen much repeatable, proving the attainment of a homogeneous microstructure in each test specimen. The stress-strain curves are composed of two distinct regions: elastic and inelastic regions (Figure 5.22). The elastic regions continue until about 0.01 strain for both neat epoxy and composite and the inelastic deformation continues until failure strain. Both, elastic modulus, yield strength and tensile strength increases as the vol% of silica particles increases as seen in Figures

5.23(a and b). The failure strain also increases as the vol% of silica particle increases. The modulus of the epoxy resin increases from 4.23 GPa to 5.50 GPa with the addition of 2 vol% frustules (Figure 5.23(a)). The increase in elastic modulus is about 30%. The tensile strength of epoxy increases from ~79 MPa (neat epoxy) to ~108 MPa in the 2 vol% silica composite, corresponding to a 37% increase (Figure 5.23(b)). The increase in yield strength is about 50%. The fracture strain increases from 0.028 for neat epoxy to 0.0305 for 2 vol% of silica composite. The elastic moduli of 2 vol% silica composites are also calculated using rule of mixtures and the Eshelby model. As is seen in Figure 5.23(b), rule of mixtures shows very good agreement with the experimental elastic modulus for 2 vol% composite.

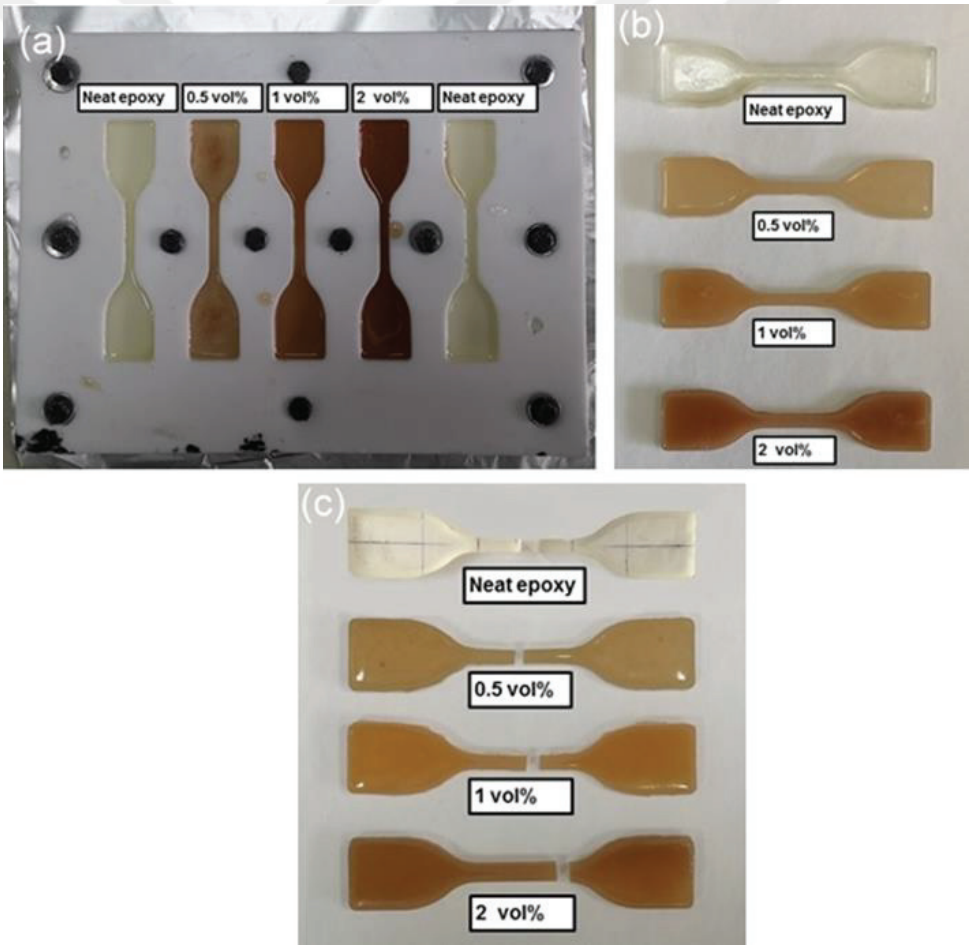

Figure 5.21. The pictures of neat epoxy and 0.5, 1 and 2 vol% silica-epoxy composite tensile test specimens (a) inside the Teflon mold, (b) after curing at 50 °C for 24 h and (c) after the tensile test, respectively.

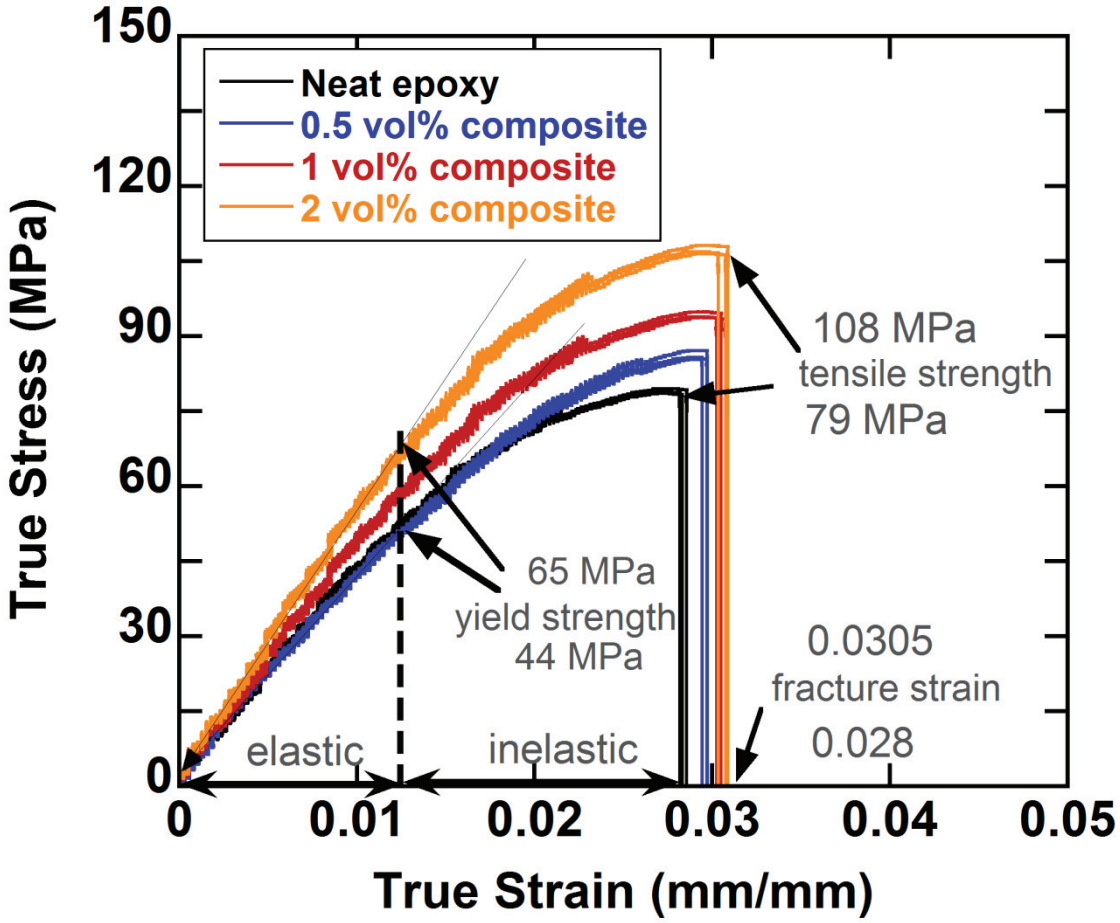

Figure 5.22. The tensile stress-strain curves of HF leached (1 N HF 15 min) and ball milled (500 rpm 1 h) 1200 °C heat-treated frustules filled epoxy samples.

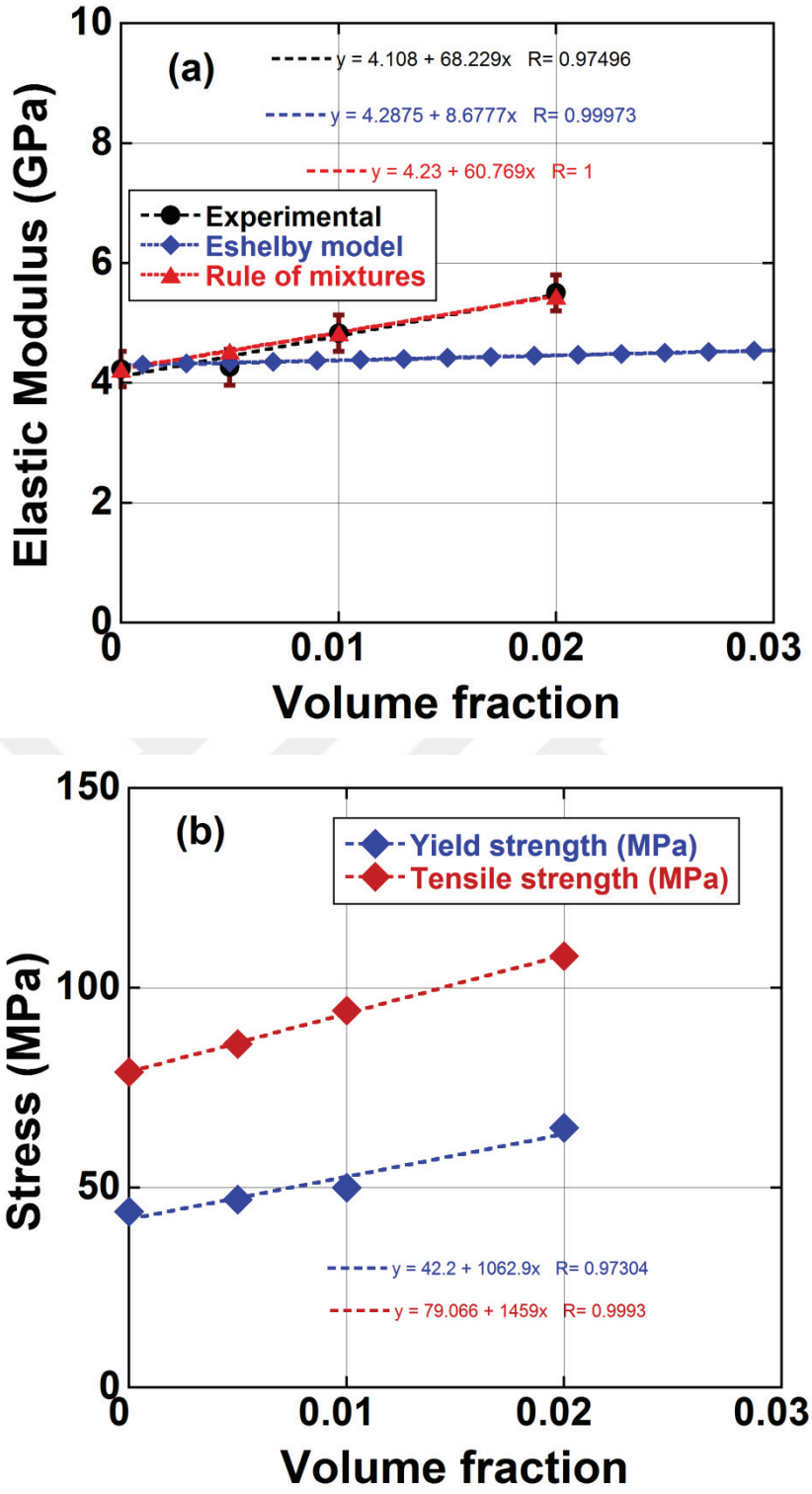

Figure 5.23. (a) Elastic modulus and (b) yield and tensile strength of HF leached (1 N HF 15 min) and ball milled (500 rpm 1 h) 1200 °C heat-treated frustules filled epoxy samples.

5.6. Fracture Surface Analysis

The tensile fracture SEM surface micrographs of neat epoxy are shown in Figures 5.24(a-d). The fracture surface of neat epoxy is similar to the typical flat fracture surface of a brittle thermosetting matrix. The crack starting zone is noticeably smooth and the facture surface consists of riverbed lines in the crack propagation zone (Figure 5.24(a)). The crack propagating traces are all in the direct radiation directions and there are numerous minor lines as shown in Figures 5.24(a-d). This is because neat epoxy with no fillers shows a typical brittle material behavior.

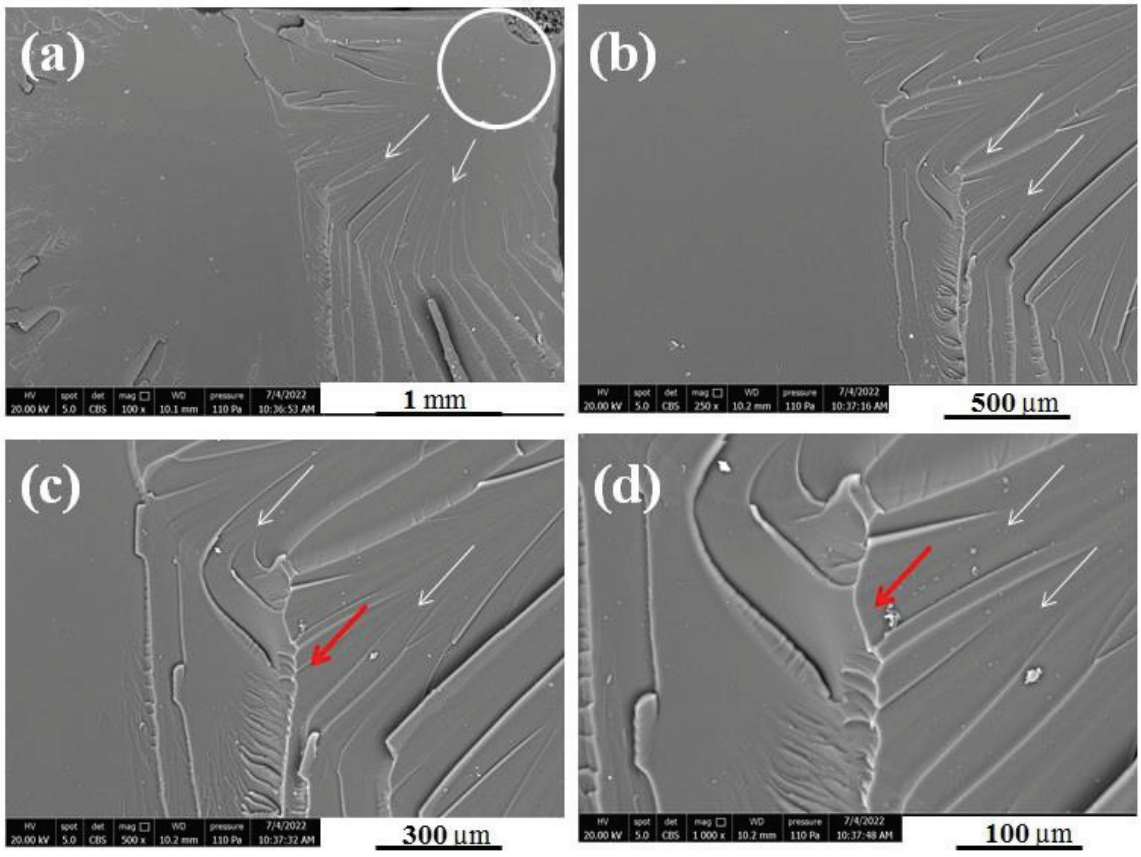

Figure 5.24. The SEM images of the neat epoxy fracture surfaces.

The appearance of the fracture surface varies from wavy in neat epoxy to ribbed (jagged) form in the composite as the frustule content increases. The micrographs in Figures 5.25(b-d) show that the dispersion of nano-silica powder in epoxy matrix is relatively uniform, no noticeable powder agglomeration is seen. This further demonstrates the effective frustule mixing in the matrix. The appearance of debonded (small black holes) and non debonded silica particles (white) on the fracture surface also show that these nano particles played a main role on the crack formation and progression in the composite. A completely embedded silica party in the epoxy matrix with a good adhesion to the epoxy matrix is seen particularly in Figure 5.25(d).

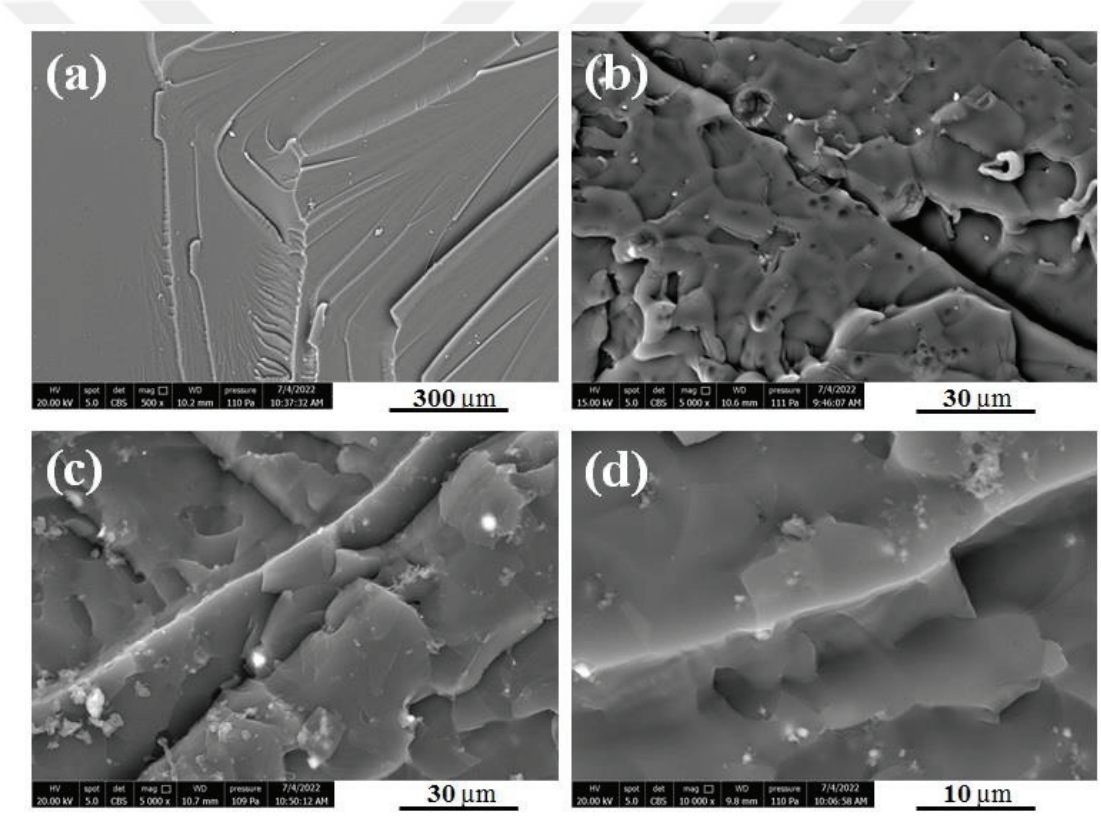

Figure 5.25. The SEM images of fracture surfaces of (a) neat epoxy, (b) 0.5 vol%, (c) 1 vol%, and (d) 2 vol% nano-structured frustules filled epoxy samples.

Figures 5.26(a-f) shows a main crack growth in a nano-structured diatom frustules through a shear band region at ~135° to the loading axis. The interfacial crack propagation was along the interface of the 1200 °C heat-treated, HF leached and ball

milled 0.5 vol% nano-structured frustules sides and cracks extend from the interface to the matrix in Figure 5.26(c) and (d).

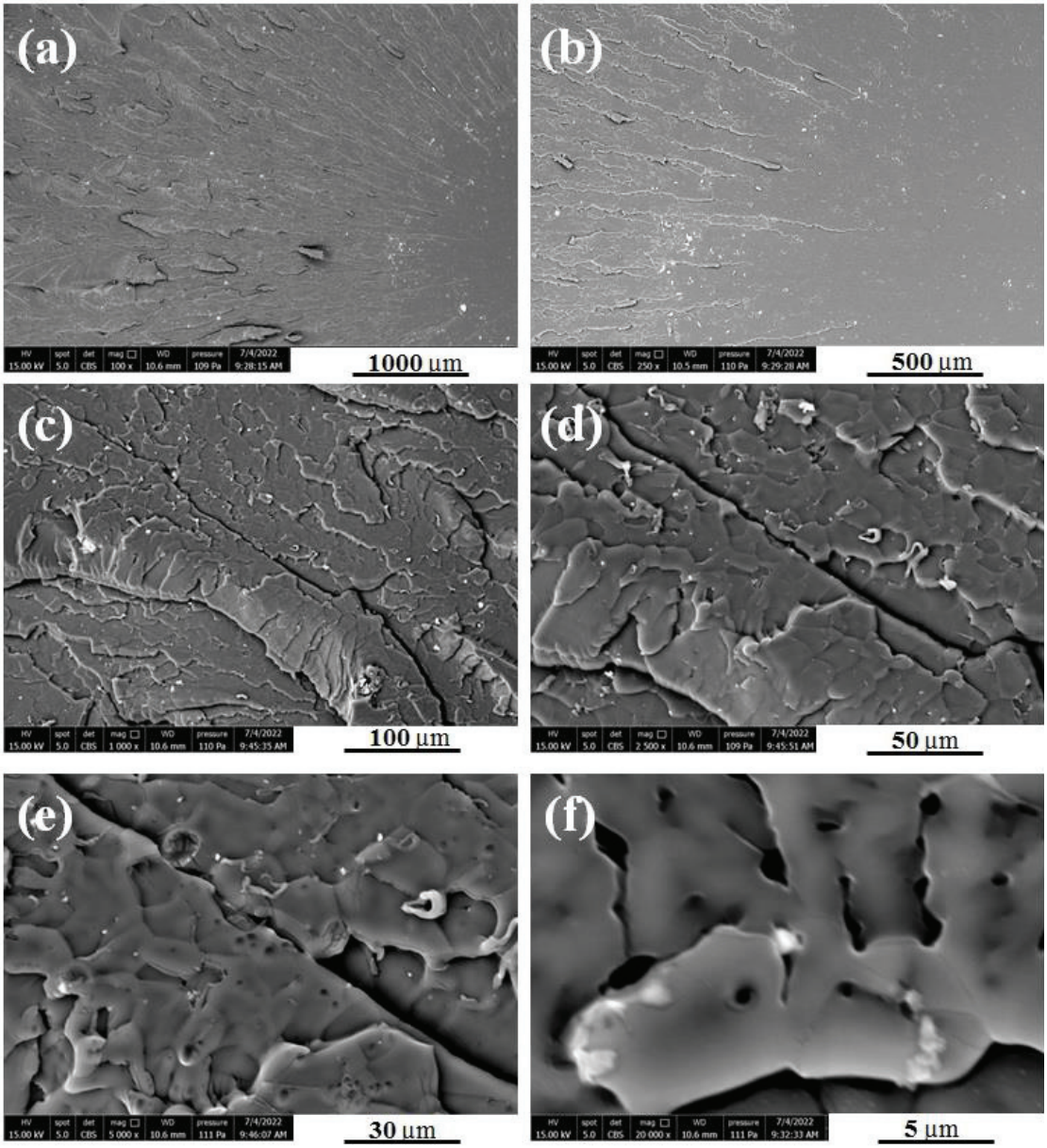

Figure 5.26. The SEM pictures of HF leached, ball milled and 1200 °C heat-treated 0.5 vol% (1.165 wt%) nano-structured frustules filled epoxy samples.

While the volume percentage of frustules increases, the concentration on the fracture surfaces of nano-silica increases (Figures 5.27(a-f) and 5.28(a-f)). Significantly higher content of nano-structured frustules led to induce massive sub-cracks or micro-cracks, as shown in Figures 5.27(f) and 5.28(f), which could encounter more flaws during crack propagation in the nanocomposite.

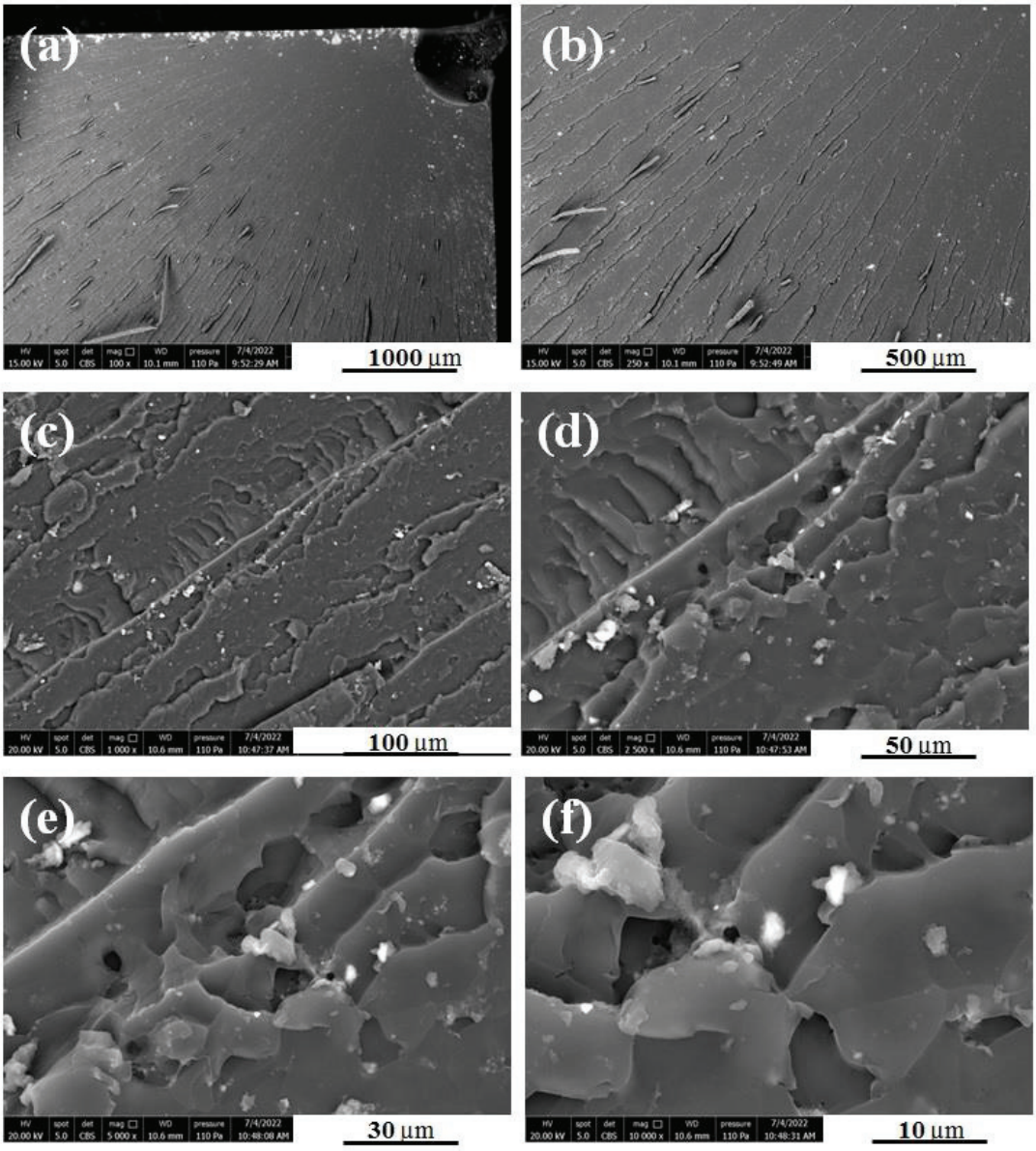

Figure 5.27. The SEM pictures of HF leached, ball milled and 1200 °C heat-treated 1 vol% (2.33 wt%) nano-structured frustules filled epoxy samples.

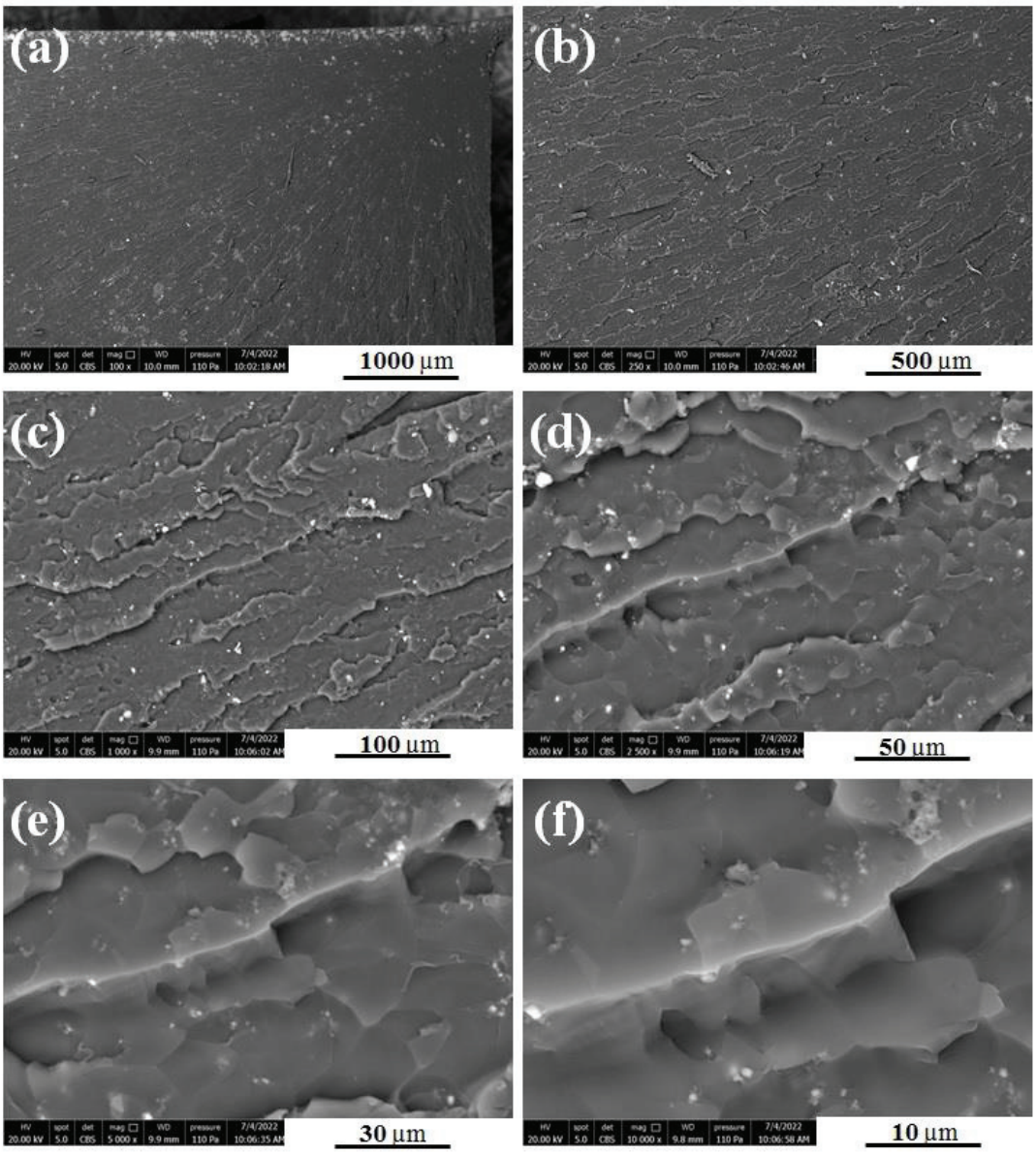

Figure 5.28. The SEM pictures of HF leached, ball milled and 1200 °C heat-treated 2 vol% (4.66 wt%) nano-structured frustules filled epoxy samples.

Figure 5.29(a) shows the fracture surface of 0.5 vol% silica added composite. On the fracture surface, a partially debonded silica particle is seen. The corresponding energy dispersive X-ray spectroscopy analysis and the composition of this silica nano particle are shown in Figures 5.29(b and c). The elemental mapping results indicate the existence of Si, O and Al. The particle is composed of 45.53 wt% of Si, 53.09 wt% O and 1.3 wt% Al. The elemental mapping of the fracture surface of the 2 vol% silica added composite is shown in Figure 5.30. The nano-silica powder (light blue), carbon (red), and oxygen (green) are clearly seen in the same figure. Figure 5.31 shows the fracture surfaces of a

0.5 vol% nano-structured diatom frustules filled epoxy sample. The measured powder size of silica on the fracture surface is shown in the same figure. The particle size ranges 425-685 nm, which fairly complies with the mean particle size in Table 5.6.

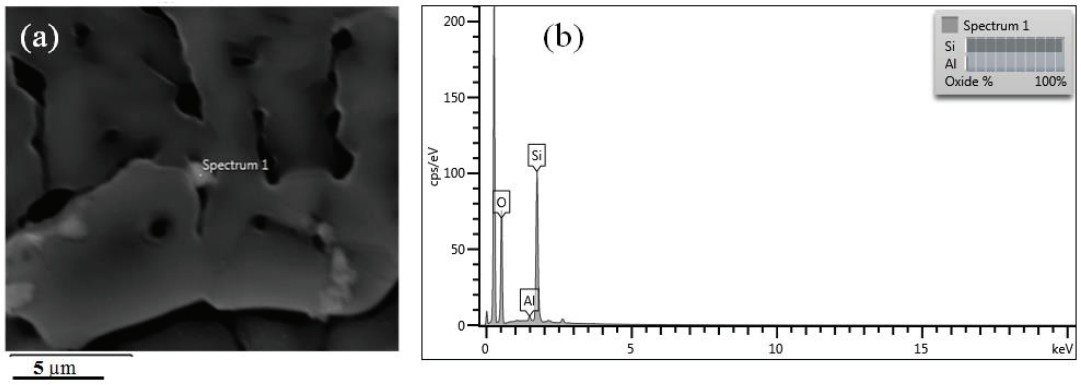

(c)

Element	Wt (%)	Atomic (%)
O	53.09	66.50
Si	45.53	32.48
Al	1.38	1.02
Total:	100.00	100.00

Figure 5.29. (a) Cross-sectional SEM image, (b) the corresponding energy dispersive X-ray spectroscopy (EDX) and (c) mapping results of acid leached (1 N, 15 min), ball milled (500 rpm, 1 h) and 1200 °C heat-treated 0.5 vol% nano-structured frustules filled epoxy sample.

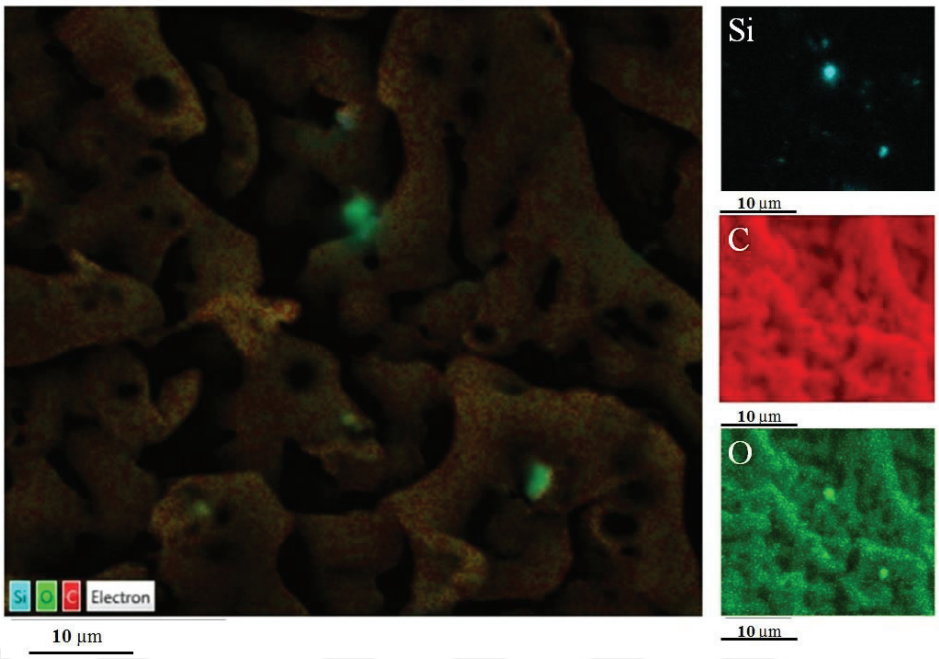

Figure 5.30. A cross-section SEM image of colorized energy dispersive X-ray spectroscopy (EDX).

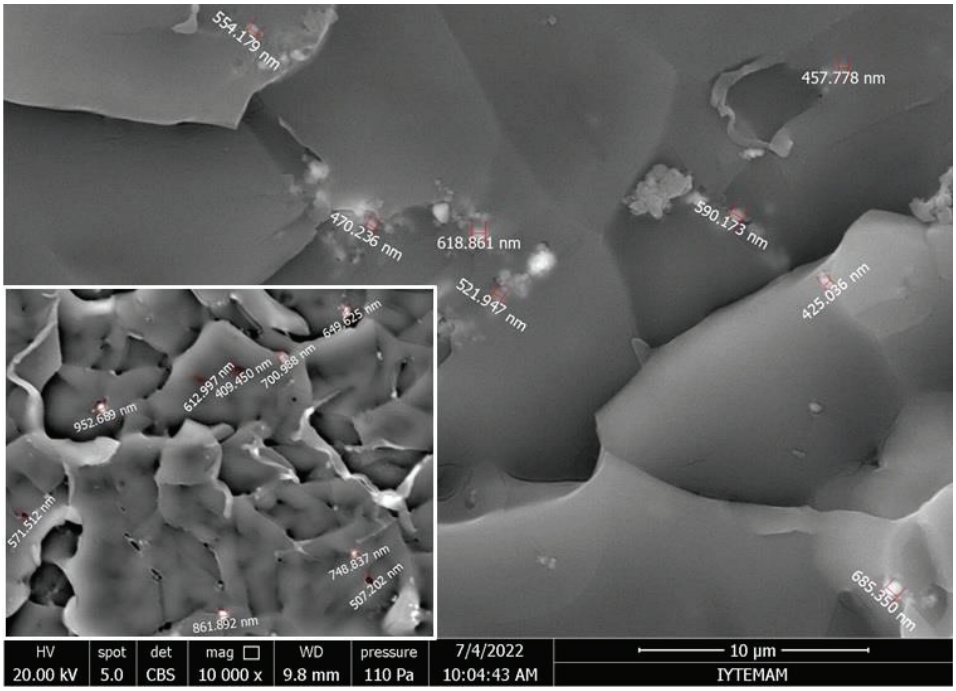

Figure 5.31. The fracture surfaces of 2 vol% acid leached (1 N, 15 min), ball milled (500 rpm, 1 h) and 1200 °C heat-treated nano-structured frustules filled epoxy sample.

5.7. Numerical Modelling

Figures 5.32(a and b) shows the composite, computational, and experimental flow stress-strain curves. As it is seen in these figures within the studied Poisson's ratio, the experimental flow stresses are higher than those of numerical ones. Numerical analyzes show that the elastic and inelastic regions are similar to the experimental 2 vol% silica filled composite. Furthermore, the tensile strength of composites increases from ~88 MPa (Poisson's ratio: 0.17) to ~90 MPa (Poisson's ratio: 0.001). Furthermore, the effect of mesh size is investigated. As seen in Figures 5.32(a and b), as the mesh size increases, the model predicts lower stress valleys and elastic and inelastic regions become more similar. The mesh size has an obvious effect on the peak stresses in the composite. The best agreement between the numerical and experimental results of the stress-strain curves was achieved in the fine mesh model. Rupture starts at 54000 times 90 MPa and 0.0213 strain in the 0.001 and 0.17 Poisson's ratios in the coarse mesh model and rupture starts at 52000 times 85 MPa and 0.0205 strain in the 0.001 Poisson's ratios. Beside, rupture starts at 50000 times 83 MPa and 0.0198 strain in the 0.17 Poisson's ratios.

Using the unit cell model, it is also possible to contour the effective plastic strain within the unit cell. Strain distributions in the y-direction for the different Poisson's ratios (0.001 and 0.17) coarse and fine models are shown sequentially in Figures 5.33, 5.34, 5.35, and 5.36. There is no difference in 0.005 strain value between 0.001 and 0.17 Poisson's ratios. At the beginning, stress occurs at the top of the left edge in the spherical silica particles as seen in Figure 5.33(b). Stress increases continue on this side and lastly, rupture starts in this field. There is little difference between Poisson's ratios in the coarse mesh model. Figures 5.35 and 5.36 show a more sensitivity between silica and epoxy interphase. Experimental studies and numerical modeling have an agreement in the elastic and inelastic regions.

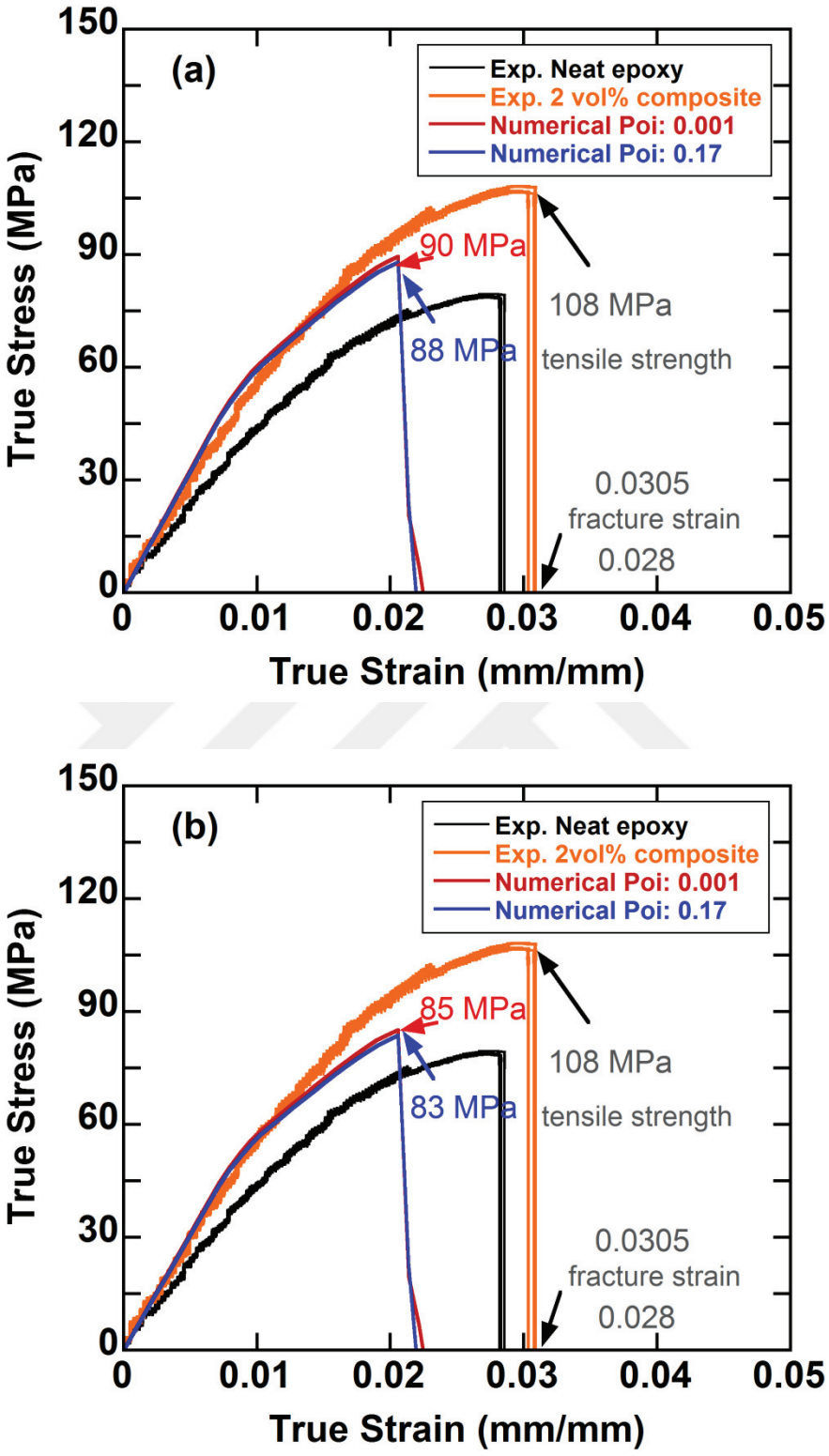

Figure 5.32. The numerical analyzes of (a) coarse and (b) fine meshed silica filled epoxy composites.

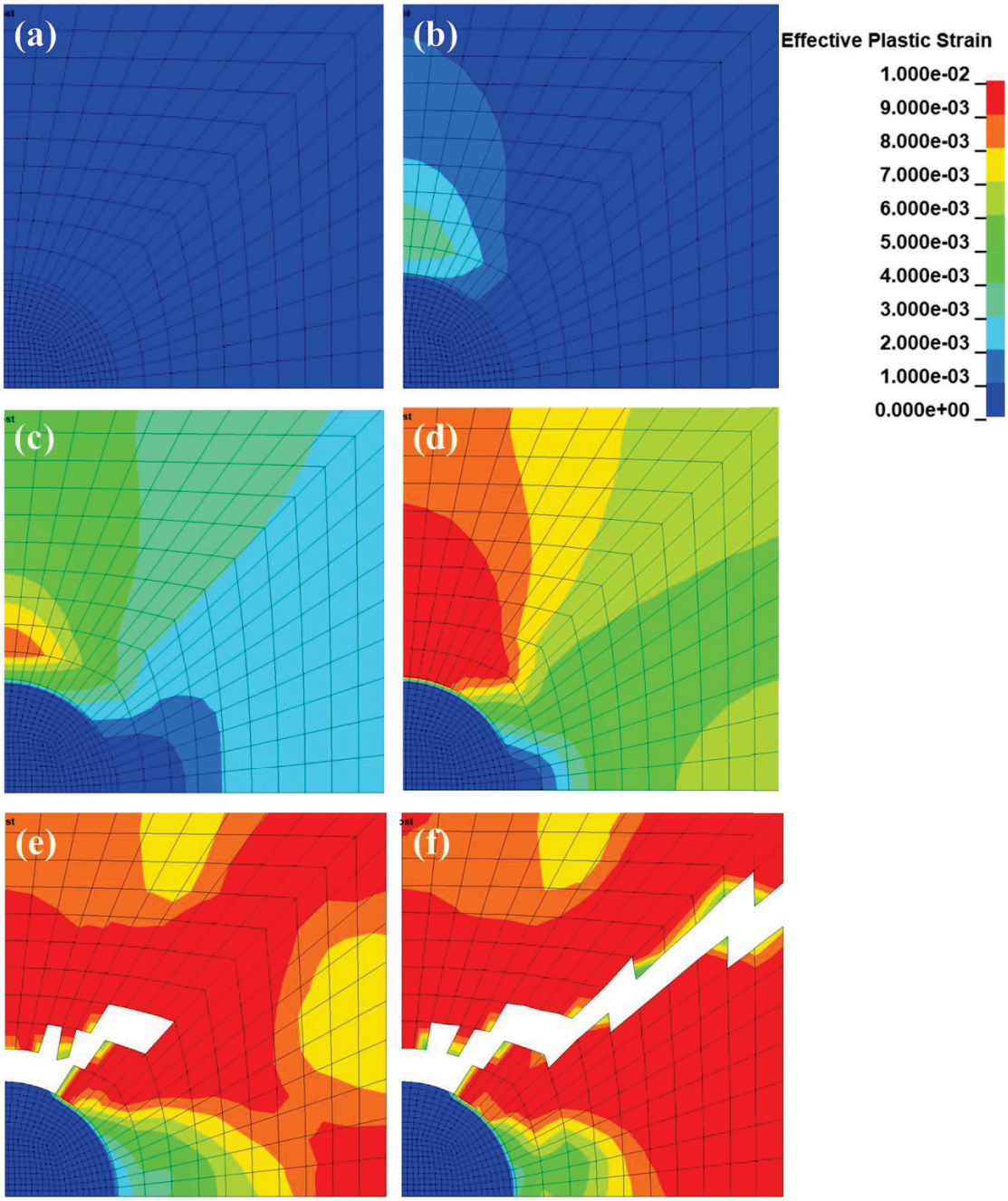

Figure 5.33. The 0.001 Poisson's ratio coarse meshed (a) 0.005, (b) 0.010, (c) 0.015, (d) 0.0205, (e) 0.0213 and (f) 0.0253 strain of silica filled epoxy composites.

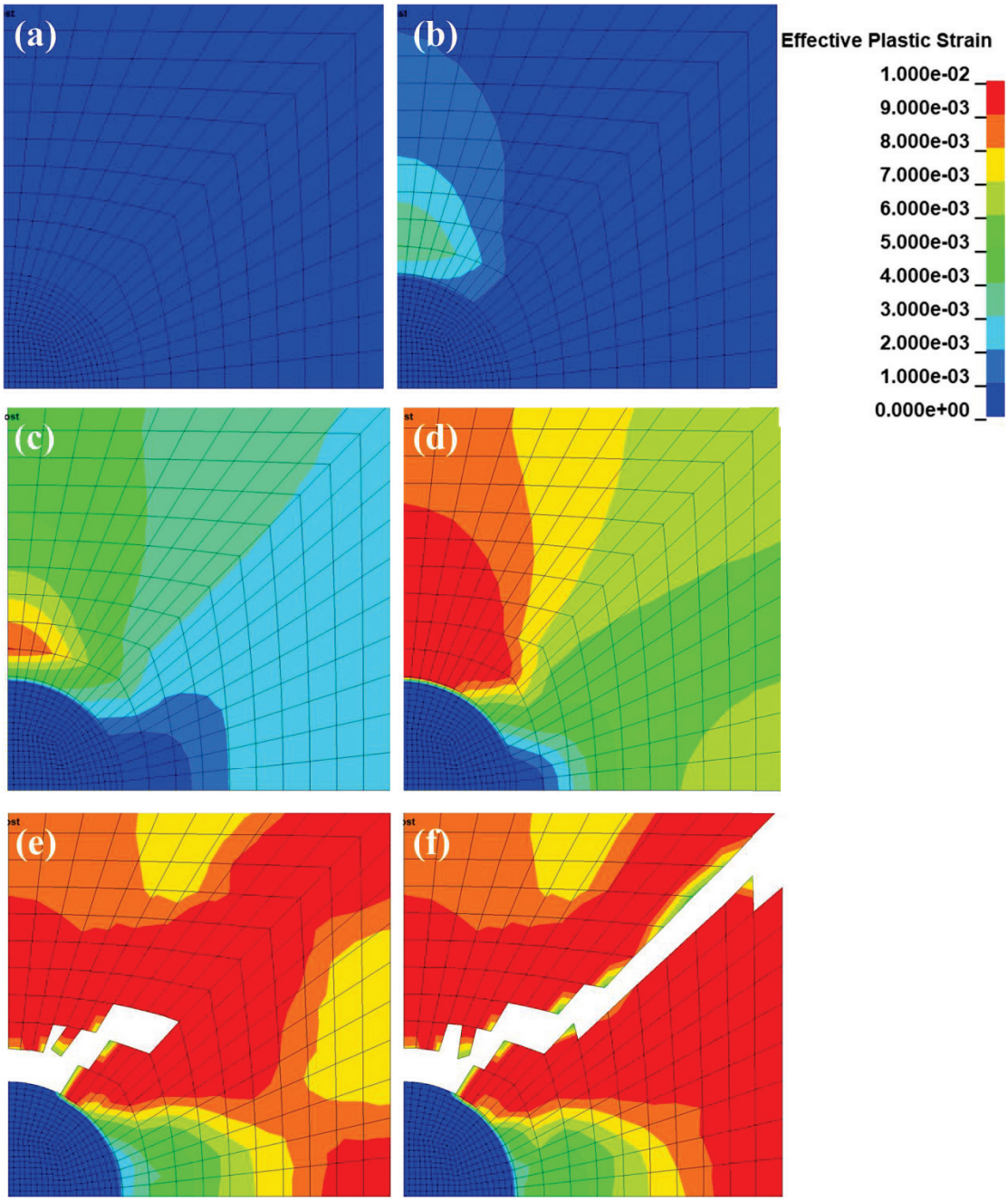

Figure 5.34. The 0.17 Poisson's ratio coarse meshed (a) 0.005, (b) 0.010, (c) 0.015, (d) 0.0205, (e) 0.0213 and (f) 0.0230 strain of silica filled epoxy composites.

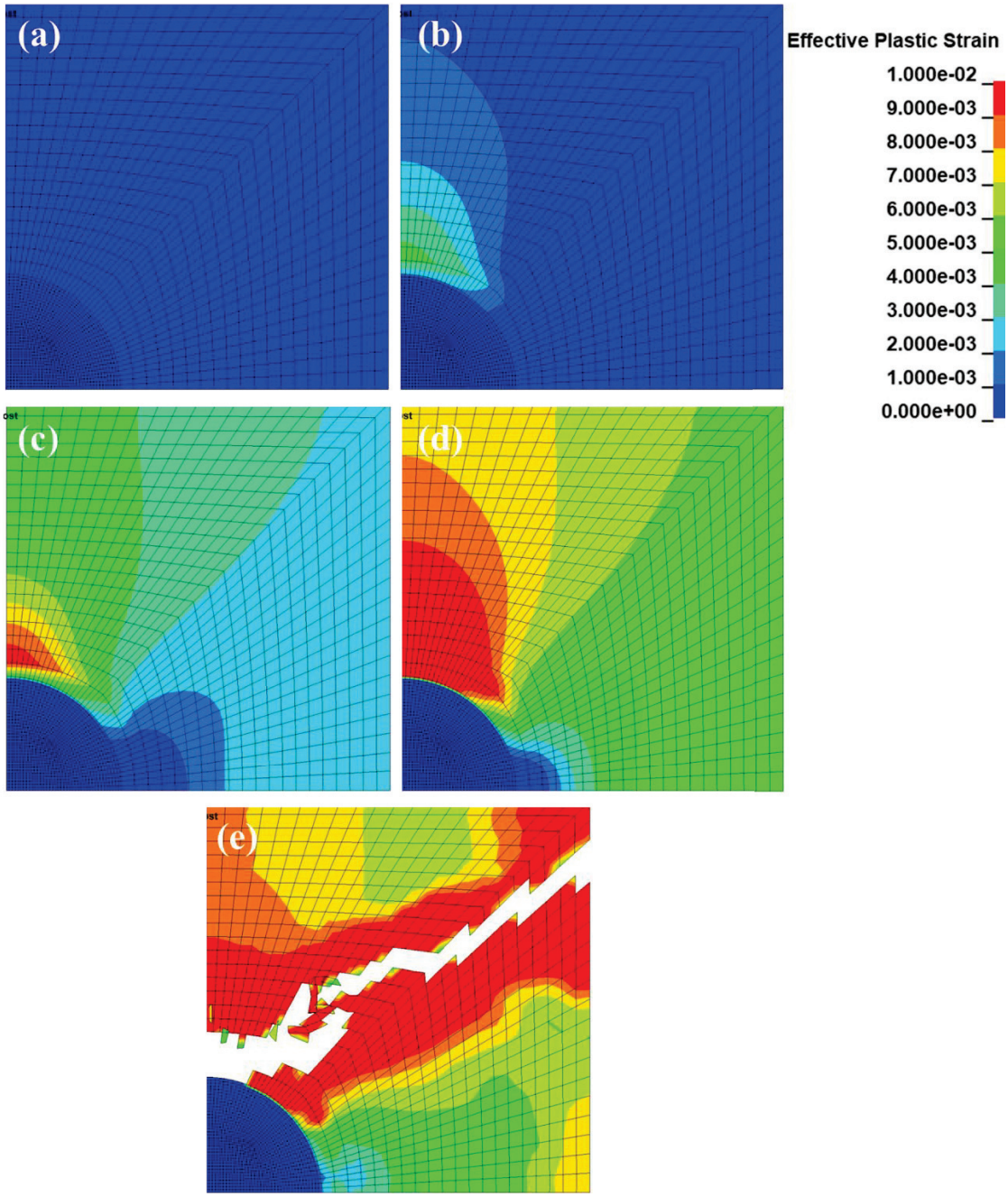

Figure 5.35. The 0.001 Poisson's ratio fine meshed (a) 0.005, (b) 0.010, (c) 0.015, (d) 0.020 and (e) 0.0205 strain of silica filled epoxy composites.

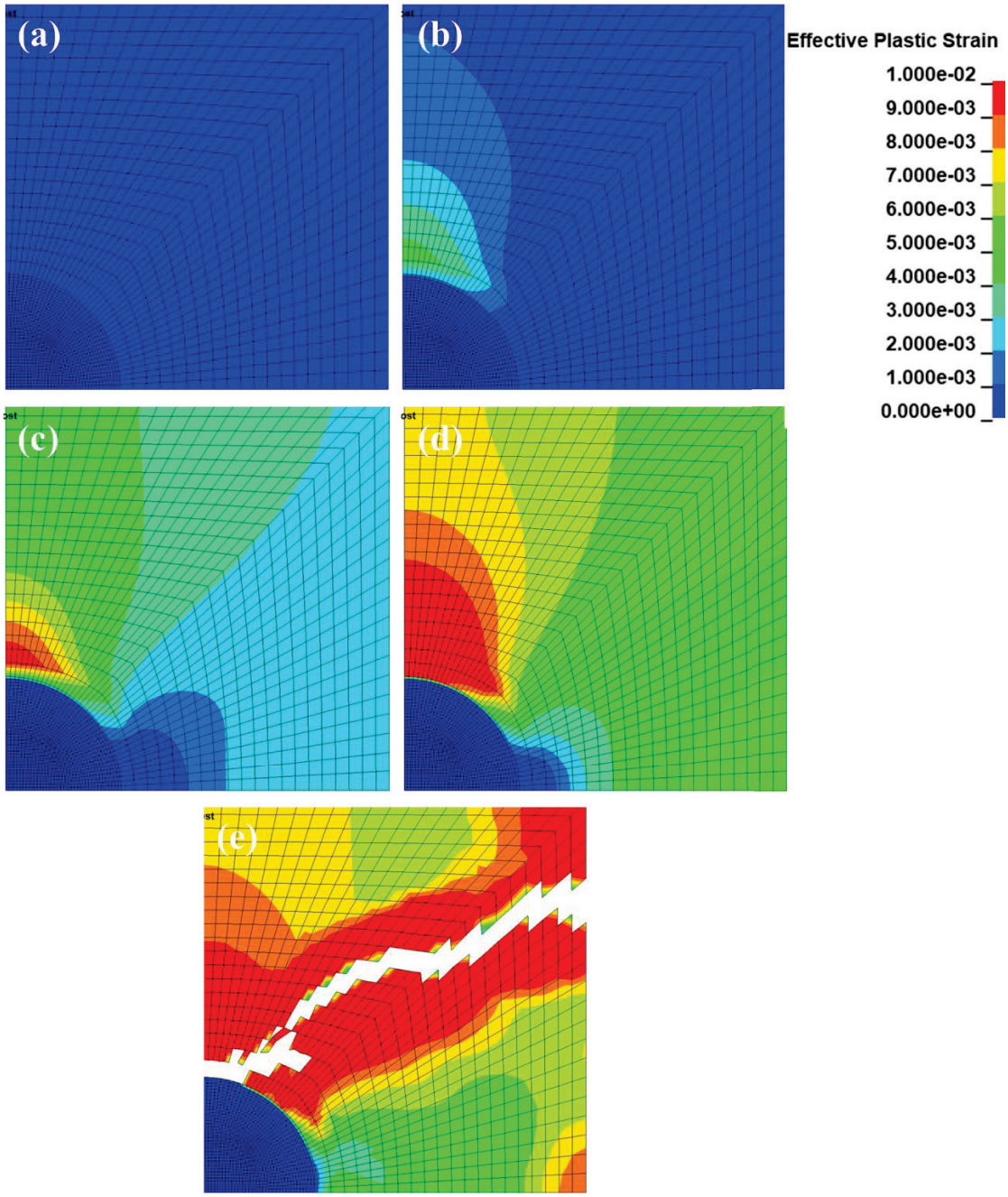

Figure 5.36. The 0.17 Poisson's ratio fine meshed (a) 0.005, (b) 0.010, (c) 0.015, (d) 0.019 and (e) 0.0198 strain of silica filled epoxy composites.

CHAPTER 6

DISCUSSION

6.1. The effect of heat treatment and acid leaching

Diatom frustules are formed by a bio-based precipitation reaction in which silica nano-spheres are agglomerated amorphously during cell division [127]. A living diatom frustule has a de-polymerized amorphous silica structure, resulting from Si-OH silanol group [201]. While, the diatom frustules are converted into opal-CT and quartz during deposition onto the ocean floor [202]. The amount of silica in the as-received frustule was about 90% and the rest is composed of other oxides. Macroporous silica can be used as a platform for in situ production of Thrombin Binding Aptamer for optical biosensing applications. Macroporous silica is produced by electrochemically etching crystalline silicon, followed by thermal oxidation at 900 °C [138]; its morphology is similar to that of 900 °C heat-treated and HF leached (1 N HF 15 min) diatom frustules, as illustrated in Figures 6.1(a and b).

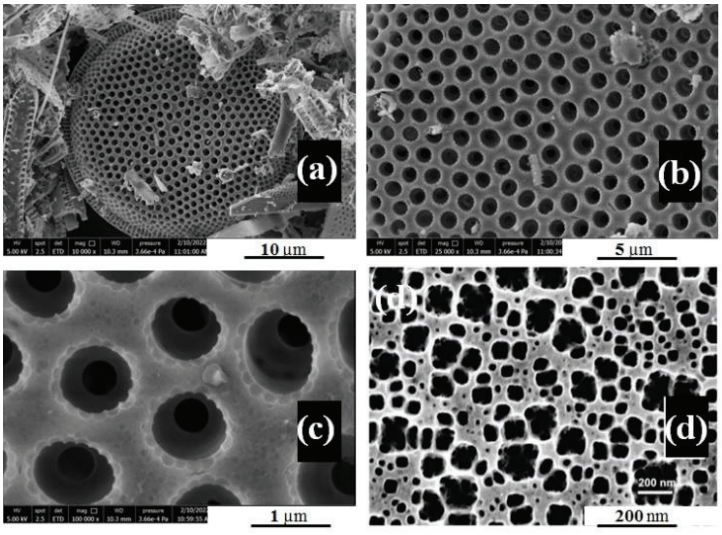

Figure 6.1. Comparative images of (a-c) 900 °C heat-treated and HF leached (1 N HF 15 min) diatom frustules and (d) synthetic silica [138] (Macroporous silica).

The XRD analysis of the as-received frustules complies with the above and it is mainly composed of amorphous silica (88%) with a small amount of crystalline quartz (about 10%). The organic matter and water molecules were reported to disappear in the natural diatom frustule after about 600 °C and partially ordered crystalline low-quartz and or precursor to low-cristobalite started to form at about 800 °C, while heating until about 1200 °C lead to the formation of low-cristobalite [193, 203]. A similar observation was made in the present study. Figure 6.2 exhibits the TGA curve of the as-received frustule and the weights of the frustules after a heat treatment at 900, 1000, 1100, and 1200 °C. The weight reduction in the TGA curve of the as-received frustule until about 600 °C is due to the removal of adsorbed water and the decomposition of organic material. This comes with a 3% reduction in weight. The weight then increases until 1200 °C with an amount of one percent. The weight reduction in the heat-treated frustules is about 4% at 900 °C, and then it increases by 1.5% when the heat-treatment temperature is increased to 1200 °C. The weight increase in the heat-treated frustules at increasing temperatures is therefore in accord with the TGA curve. The increase in the weight of the frustules is likely due to the oxidation of iron oxide.

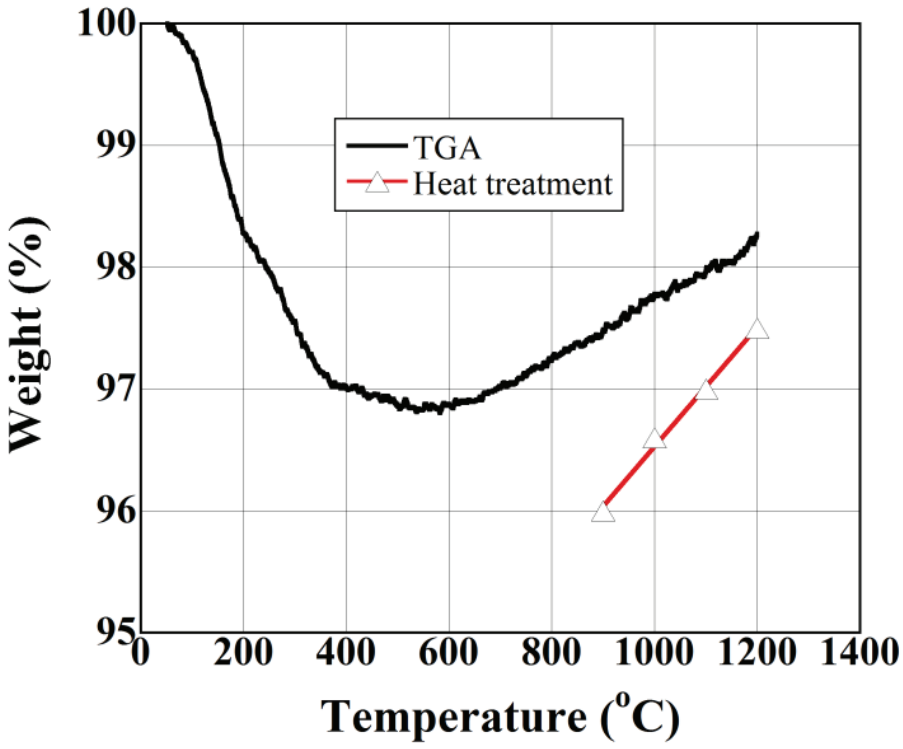

Figure 6.2. TGA curve and weight of heat-treated frustules.

Diatom frustules mainly consist of very small silica crystal particles agglomerated amorphously. Although silica is a very hard material, the bonds between these crystals in frustules are weaker than intra-particle bonds [17]. It is well known that silica is quite inert, being attacked by HCl and HF acid. About 12% of the as-received frustule passed under the filter after 10% (3.18 N) HCl acid leaching and this value increased to ~14% when the acid concentration increased to 20% (6.36 N). Furthermore, leaching 900 °C heat-treated frustules at 10% (3.18 N) HCl increased the under-filter weight from ~13% to ~15%. Undissolved frustules particles in the under-filter solution were weighed which were ~8, ~9, ~11, ~13 and ~18% 25, 900, 1000, 1100, and 1200 °C, respectively (Figure 5.7). It is also observed in Tables 5.3, 5.4, and 5.5 that HCl acid is not effective in reducing the particle size of diatom frustules. The rate of dissolution of crystalline and amorphous silica is essentially independent of the HCI acid [18].

The heat treatment at and above 900 °C until about 1200 °C resulted in the formation of low-cristobalite. As the heat treatment temperature increased to 900, 1000, 1100, and 1200 °C, the crystallinity increased sequentially to 20, 34, 39, and 46% without acid leaching (Figure 5.8(f)). Almost half of the frustule structure was converted into crystalline silica at 1200 °C for 2 h heat treatment. Acid leaching of the frustules heat-treat at 1200 °C etches the crystalline grain borders (Figure 5.16(e)). Figure 6.3 shows an SEM micrograph of a cell wall of a frustule heat-treated at 1200 °C and acid leached (1 N, 15 min). The measured crystalline grain sizes shown in the same figure (208-523 nm) fairly comply with the mean particle size of 1200 °C heat-treated frustules in Table 5.6. The light grey area between two grains marked by an arrow (A) in Figure 6.3 is most likely a partially dissolved amorphous phase. The surfaces of the leached crystalline particles are also seen to accommodate 60 nm particles on its surface as marked by the arrows (B) in the inset of Figure 6.3. These particles are most likely amorphous silica, the remnant of acid leaching.

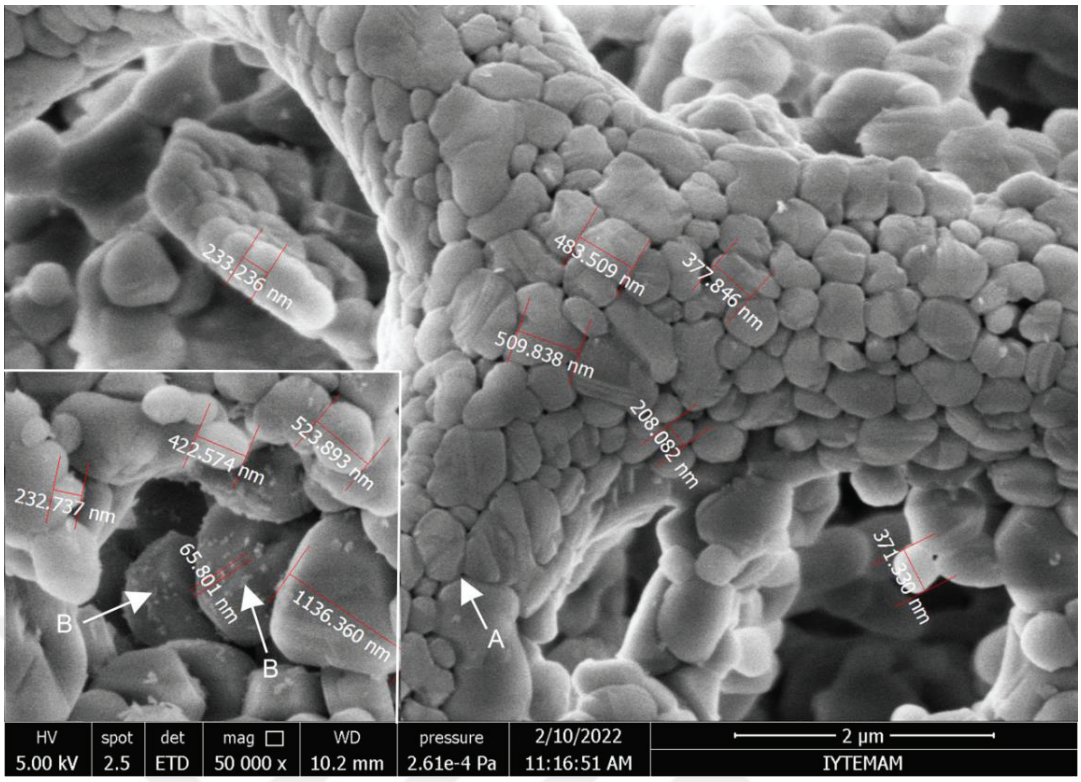

Figure 6.3. The SEM cell wall of a frustule heat-treated at 1200 °C and acid leached (1 N, 15 min) showing the crystalline and amorphous phases.

The microscopic observations demonstrate that the amorphous phase is mostly found in between the crystalline particles and acid leaching removes the outer amorphous phase faster than the crystalline grains. The thermodynamics of the dissolution reaction of silica in hydrofluoric acid is

$$SiO_2 + 6HF = H_2SiF_6 + 2H_2O \quad (6.1)$$

In silica materials, both crystalline and amorphous structures are made of four-dimensional SiO_4, combined by covalent $\equiv Si - O - Si \equiv$ (siloxane) bond to form three-dimensional silicate structures. The four siloxane keys must be broken to dissolve the silica network structure. It was shown that the dissolution rate of crystalline α-quartz in HF solution was slower than fused silica and the dissolution rate of both depended on the concentration of HF and time [18]. Almost linear relations were found between the dissolution rate and concentration and between the dissolution rate and time. The increased percentage of under-filter as-received frustule with increasing acid

concentration at 15 min leaching time is clearly seen in Figure 5.11(a). At increasing leaching times, 30 and 60 min, the percentage increases abruptly and reaches about 92%, regardless of the acid concentration. The percentage of under filter 900 °C heat-treated frustules however shows a gradual increase at 1 and 3 N HF concentrations with time, reaching 80 and 90% at 60 min, respectively. At higher acid concentrations of 5 and 7 N, the percentage of under-filter frustules are above 90% regardless of the time. On the other side, the higher crystalline concentration of the heat-treated frustules at increasing acid concentration and times shown in Figure 5.11(b) indicates a higher rate of amorphous phase passage to the under the filter. It is interesting to note that the amount of under-filter frustule increased in the frustules heat-treated at 900 and 1000 °C as tabulated in Table 5.9. This is most likely that the crystal phases formed at these temperatures have relatively small sizes and the density difference between the amorphous and crystalline phases develops internal stresses which lead to higher dissolution/disintegration of the frustules. The cracks were seen on the frustules in Figure 5.14(e) are presumed to be formed due to high internal stresses. At increasing temperatures, the size of crystal grains increases leading to reduced dissolution/disintegration of the frustules. The increased dissolution rate of under-filter frustules in the heat-treated frustules as compared with the as-received frustules listed in Table 5.7 is likely due to decreased frustule particle size in the under-filter solution. This is also seen in Table 5.7 in which the under-filter particle sizes of the frustules heat-treated at 900 °C are smaller than those of as-received frustules.

6.2. Mechanical Behavior of Nano-Structured Frustules Filled Epoxy

The studies summarized in the literature surveys on the use of silica nanoparticles in polymer matrices have proven that the addition of silica nanoparticles to polymers improves their mechanical properties. One of these investigations reports toughening epoxy resin with nano-silica fabricated from rice husk using a thermal treatment method with a particle size distribution in the range of 40–80 nm [92]. 1 wt% nano-silica fabricated from rice husk increases the tensile strength of epoxy from 38 MPa (neat epoxy) to 42 MPa, corresponding to a 10% increase in the tensile strength (Figure 6.4). Biorenewable silica increases the mechanical properties of nanocomposites and has considerable potential for use as matrix materials for high-performance composites. Other

examinations include producing or purchasing nano-silica particles. The highest values of the tensile strength (156.20 MPa) and modulus (10.06 GPa) are seen for 3 wt% purchasing of nano-silica filled epoxy as expected which is 45% and 12% higher than those of neat epoxy (Figure 6.5) [86]. It can also be observed that each nanocomposite has higher values of for tensile properties than those of neat epoxy, credited to the effect of nano-silica reinforcement. Due to the homogenous dispersion of nano-silica into the matrix and the good surface contacts it produces, a 3 wt% nano-silica filled epoxy sample provided the greatest values of tensile characteristics among all nanocomposites [86].

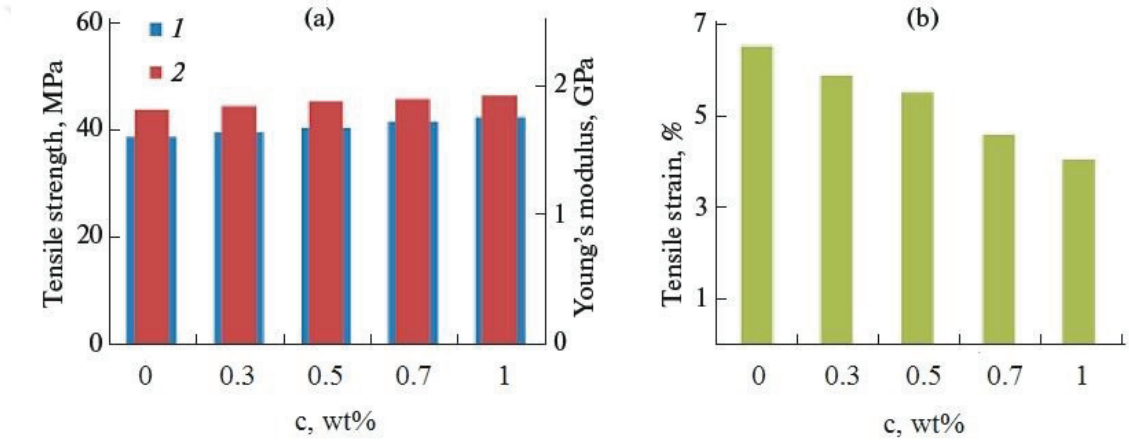

Figure 6.4. Comparison of (a) (1) tensile strength, (2) Young's modulus and (b) tensile strain of epoxy resin were modified with 0–1 wt% nano-silica fabricated from rice husk [92].

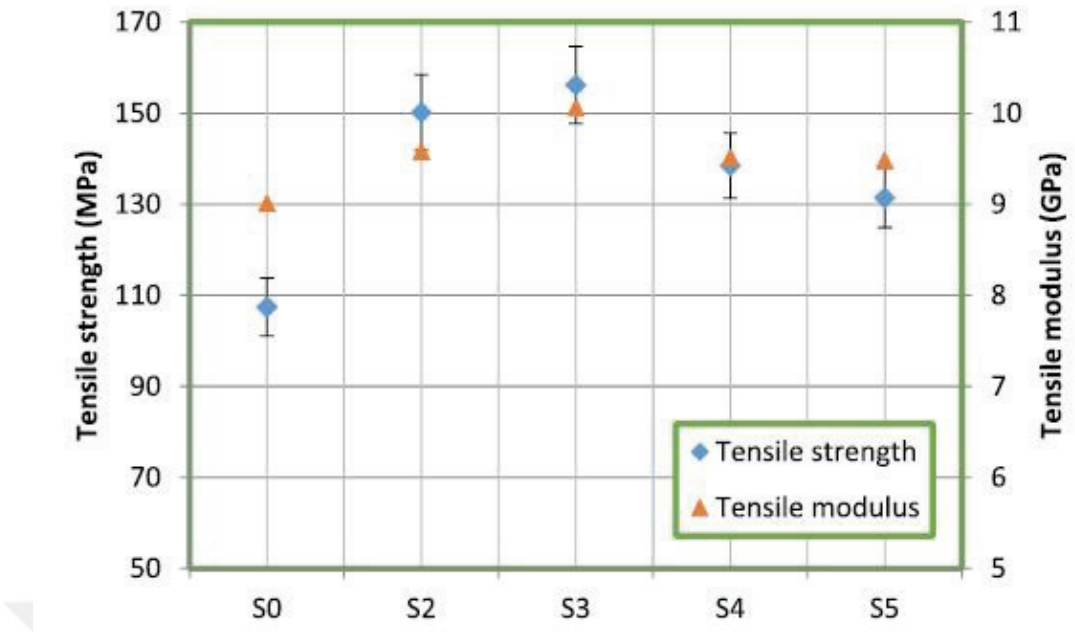

Figure 6.5. Tensile strength and tensile modulus of nano-silica added glass composites [86].

The results of the above literature survey and HF-leached, ball-milled, and 1200 °C heat-treated nano-structured silica including frustules-filled epoxy are illustrated in Figure 6.6 which shows tensile strength versus weight percent of silica. The strength values alter significantly in each study. An increase in nano-silica content in the epoxy matrix generally increased the tensile strength. The results of the tensile tests demonstrate that the addition of silica nanoparticles to the epoxy increased the samples elastic modulus and tensile strengths as a result of the potent interfacial interactions between the epoxy matrix and the nanoparticles. These interfacial interactions would probably be enhanced by the high surface area and three-dimensional pore structure of the silica nanoparticles [85]. When the increased amount of nanoparticles, considering the possible interaction of nanoparticle agglomeration with epoxy resin can be said that it has a reducing effect on strength [81]. The maximum silica content in Figure 2.19 is about 10% and the maximum tensile strength is about 160 MPa. Furthermore, nano-silica filled epoxy nanocomposites increase the modulus of elasticity in the literature survey (Figure 6.7). The tensile strength and modulus of the neat epoxy are sequentially 79 MPa and 4237 MPa. The tensile strengths of 1.16, 2.33 and 4.66 wt% HF-leached, ball-milled and 1200 °C heat-treated nano-structured frustules are 79 MPa, 87 MPa, 95 MPa, and 108 MPa, respectively. The

highest increase in the tensile strength happens when 4.66 wt% nano-structured diatom frustules are added to the epoxy matrix. As seen in Figure 6.7, the increases in elastic modulus are about 30%.

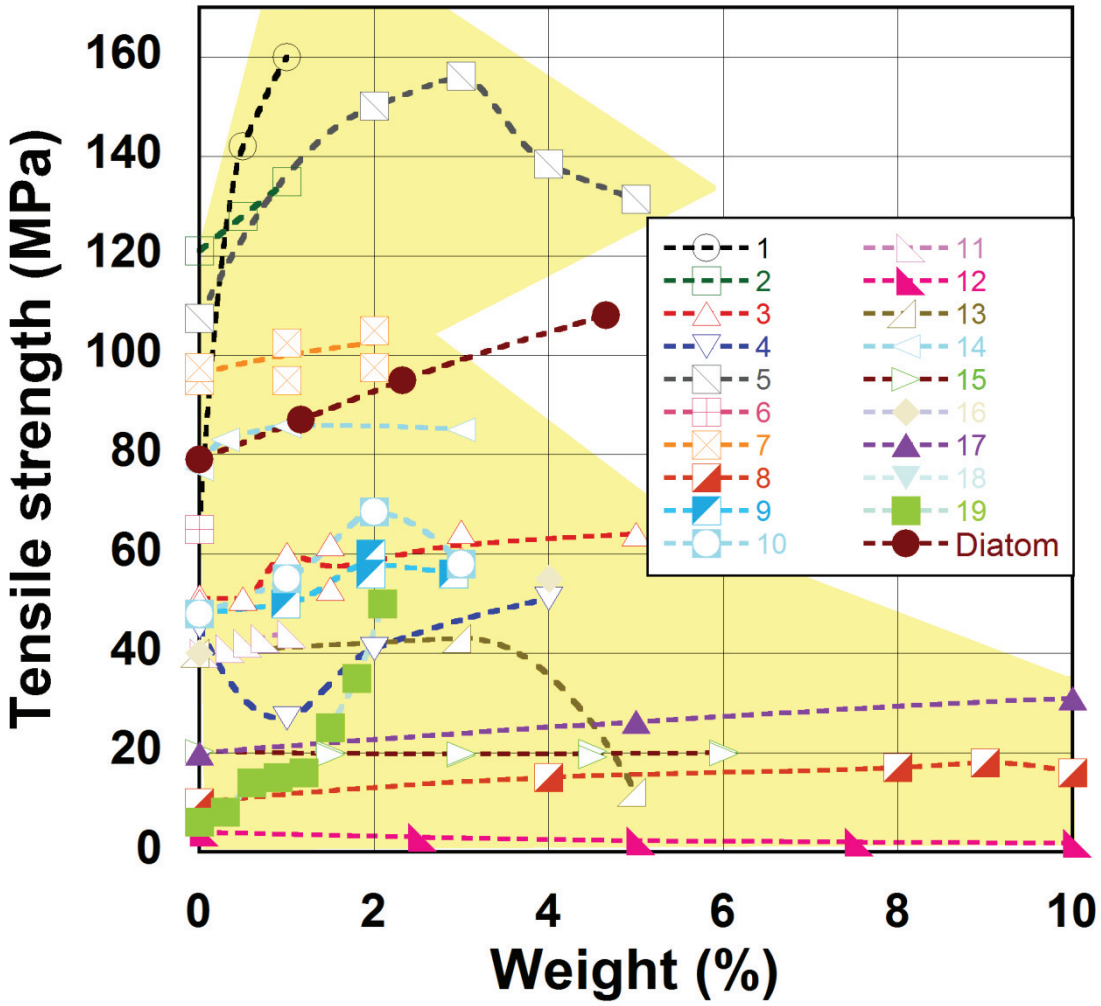

Figure 6.6. Tensile strength of silica modified epoxy composites 1 [82], 2 [83], 3 [84], 4 [85], 5 [86], 6 [87], 7 [88], 8 [89], 9 [90], 10 [91], 11 [92], 12 [93], 13 [94], 14 [95], 15 [81], 16 [96], 17 [100], 18 [97], 19 [98] and HF leached (1 N HF 15 min) and ball milled (500 rpm 1 h) 1200 °C heat-treated frustules filled epoxy samples.

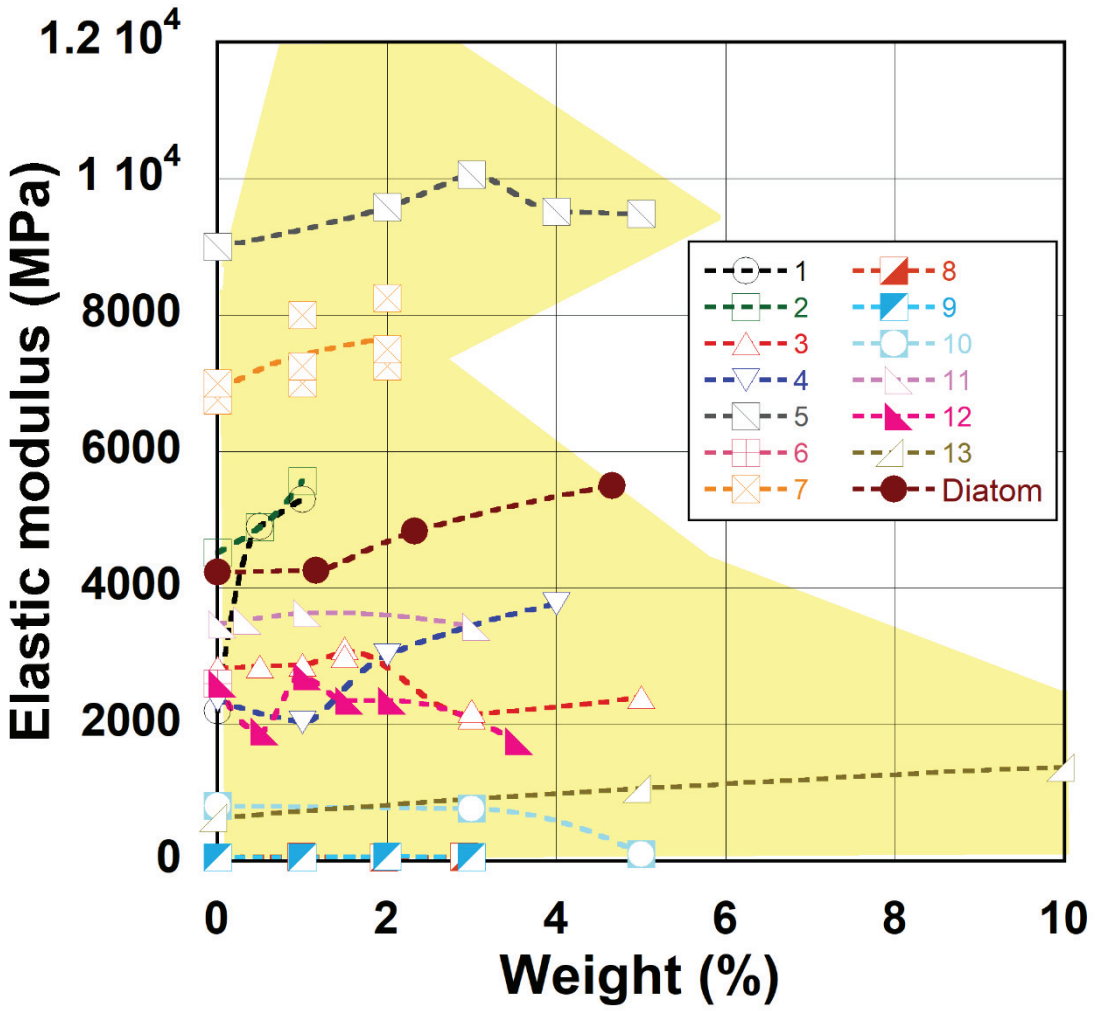

Figure 6.7. Elastic modulus of silica modified epoxy composites 1 [82], 2 [83], 3 [84], 4 [85], 5 [86], 6 [87], 7 [88], 8 [90], 9 [92], 10 [94], 11 [95], 12 [96], 13 [97] and HF leached (1 N HF 15 min) and ball milled (500 rpm 1 h) 1200 °C heat-treated frustules filled epoxy samples.

6.3. Fracture Surface Analysis

The fracture mode of a composite could be predicted by looking at how its cracks spread. A ductile fracture has slow-moving fissures that are significantly deformed by plastic deformation. On the other hand, in a brittle fracture, the cracks propagate quickly and are either accompanied by minimal or even no plastic deformation. In addition, the neat epoxy matrix possesses a brittle fracture and a reasonably smooth fracture surface. It should be emphasized that these observations support the tensile property research

results. The propagation zones, which can be loosely divided into two typical regions: the crack initiation zone and the crack propagation zone, are where all the fracture surfaces radiate outward from the initial site with numerous minor fracture steps [90]. The stress-strain graphs and the striking improvement in the epoxy's toughness and strain caused by the addition of silica nanoparticles to the samples showed that the epoxy's brittle behavior would change to become ductile at the yield point. This is related to the silica nanoparticles' surrounding microcracks. Some microcracks developed on the surface of the nanoparticles when stress was applied to the nanocomposites. This resulted in yielding behavior by wasting some of the applied energy [85]. Also, nano-structured frustules take part in interface with cracks. This also partly proves the homogeneous loading of the frustules. The density and number of fracture branches in epoxy/nanocomposites increase with reinforcements. There is a significant amount of nano-silica particles in the extension direction of cracks which can absorb the rupture energy and prevent the propagation of cracks (Figure 6.8(b)). This shows that the nano-silica particles in the epoxy resin dispersed quite well and they have a strong interface with the epoxy resin, which provides consistently higher levels of strengthening for silica nanoparticle additions than those reported in the literature (Figure 6.6) [81-100]. The crack paths are deviated by nano-silica particles, increasing the strength (Figure 6.8(a and b)) [45]. It should be noted that the epoxy matrix nano-silica particle interaction affects crack initiation [204]; cracks tend to move through weak epoxy matrix nano-silica particle interfaces and avoid strong interfaces.

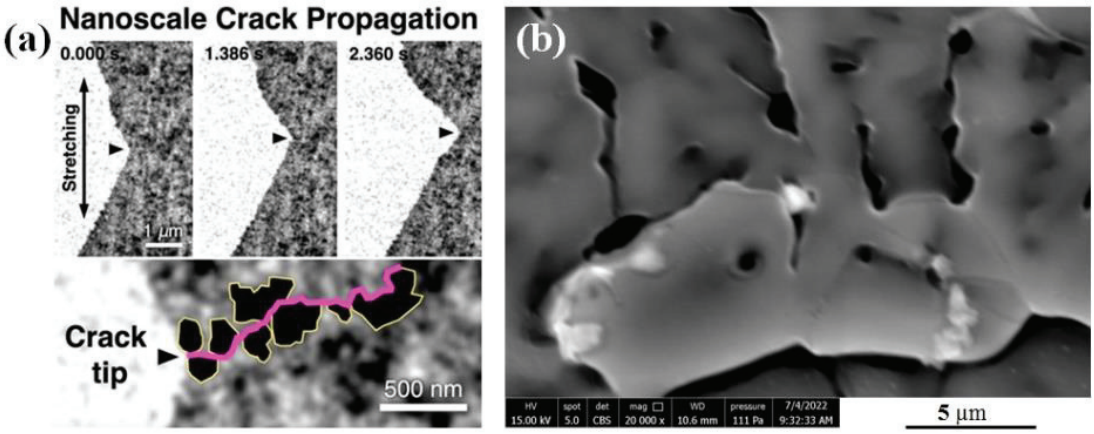

Figure 6.8. Crack path in the (a) nanoparticle-filled [45] and (b) HF leached, ball milled and 1200 °C heat-treated 0.5 vol% (1.165 wt%) nano-structured frustules filled epoxy samples.

6.4. Numerical Modelling

The majority of common materials have a positive Poisson's ratio, which means they become fatter when compressed and thinner when stretched. Auxetic materials, on the other hand, have negative Poisson's ratios (i.e. they get thinner when compressed and fatter when stretched) (Figure 6.9) [205]. According to the traditional theory of elasticity, anisotropic solids are permitted to have Poisson's ratios in the range $-1 \leq v \leq 0.5$, but isotropic materials are permitted a larger range [206]. The use of auxetic materials may lead to the creation of products of higher quality because it has been demonstrated that negative Poisson's ratios produce many positive improvements in other features of materials, such as enhanced resistance to indentation [207] and enhanced material properties [208]. In recent years, auxetic behavior has been predicted and/or experimentally measured in a number of materials including synthetic foams [209, 210], nano- and micro-structured polymers [211], metals [212], silicates [213, 214] and zeolites [215]. The negative Poisson's ratios in these materials are caused by the specific geometry of the material's micro- or nanostructure, as well as the way the micro/ nanostructure deforms when subjected to uniaxial stress.

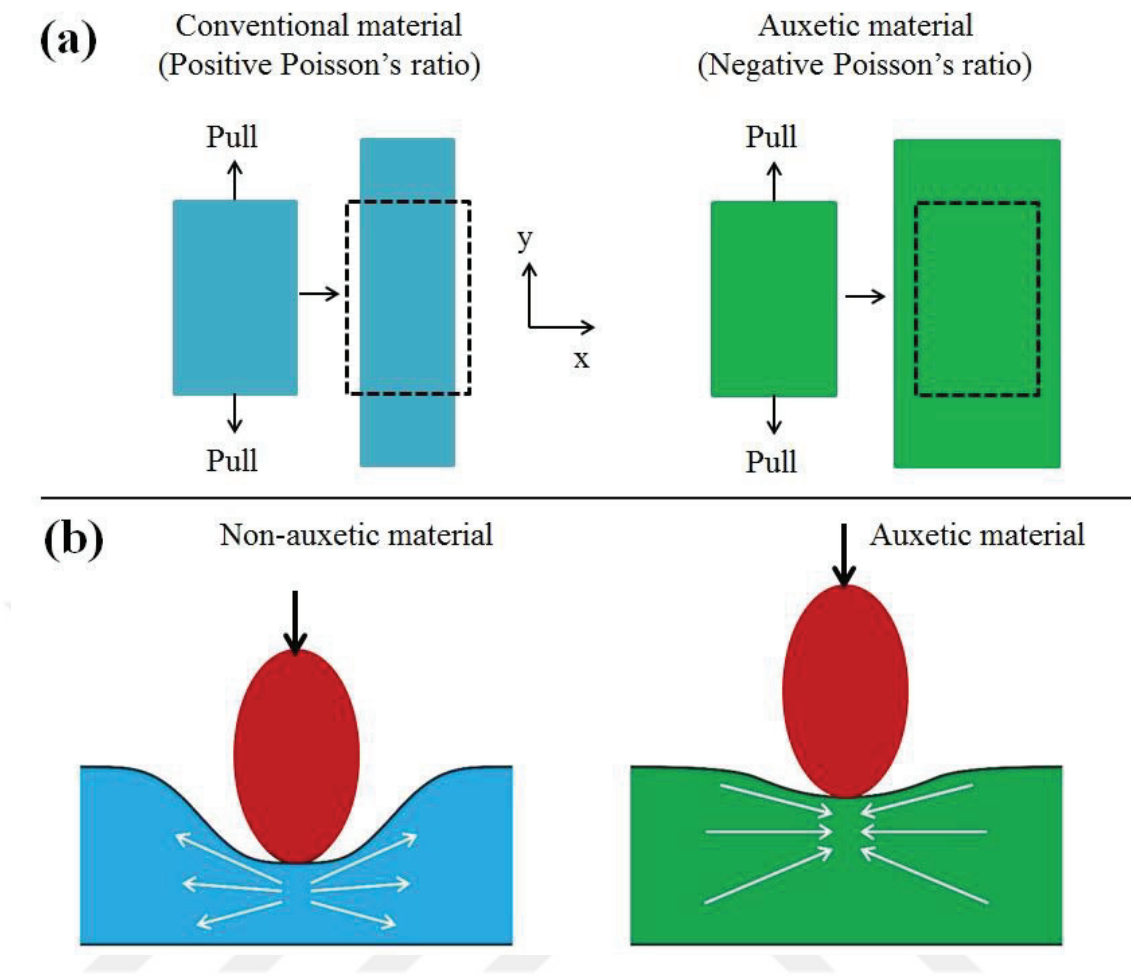

Figure 6.9. Differences in deformation behavior between conventional and auxetic materials (a) extension and (b) impact compression.

Low-cristobalite exhibits a negative Poisson's ratio (-0.17) at room temperature, meaning that isotropic polycrystalline aggregates of low-cristobalite, such as fired silica refractory without residual quartz and with negligible tridymite content, should behave auxetically. Auxetic behavior has been verified by theoretical (analytical) model calculations as well [216], and many mechanisms have been developed to explain this behavior [217]. The elastic characteristics of quartz and cristobalite, the standard silica polymorphs, are investigated, with a focus on the structural phase transition and the high-temperature phase. According to the molecular dynamics simulations performed by Kimizuka and coworkers, the temperature dependence of the elastic, shear and bulk modulus, and the Poisson's ratio are calculated [218, 219]. According to these results, the Poisson's ratio remains negative in the whole range of temperatures from room temperature up to more than 1500 °C, i.e. low- and high cristobalite are both auxetic. A

recent attempt to achieve a combination of auxetic behavior and enhanced mechanical properties was made by Assidi and Ganghoffer [220], who suggested embedding auxetic inclusions in a non-auxetic matrix. The effect of Poisson's ratio on the mechanical behavior of an isotropic material can be derived from eq. (6.2), with Young's modulus assumed to be constant [221].

$$v = \frac{3K - 2G}{2(3K + G)} \tag{6.2}$$

The shear modulus (material response to shear stress), bulk modulus (material response to volumetric stress), and Poisson's ratio are each represented by the G, K, and ν, respectively. The sign of a Poisson's ratio is determined by the relationship between K and G, as seen in eq. (6.2). As can be seen, materials with a Poisson's ratio of 0.5 or above, such as rubber, are easily deformed in shear but not in volume. As the Poisson's ratio for isotropic materials approaches the negative limit of (-1), the shear modulus approaches infinity and the material maintains its shape under loading. The material is strong in shear but easy to deform. At this point, it must be indicated that these relationships are valid only for isotropic materials, since in the case of anisotropic materials the bounds on Poisson's ratio are theoretically larger [221]. Auxetic materials do not maintain volume during elastic deformations; however, the volume of the material rises during tensile deformations, and vice versa. Since the Poisson's ratio has no effect on the deformation behavior while the material is yielding, this statement only relates to the deformation behavior before the material achieves the yield stress. Thereafter, the material maintains the volume attained at yield.

To examine the dependability of the components, it is crucial to look at the mechanism of the composite's fracture. Due to the complex behavior of failure, which is greatly influenced by the fiber orientation, fiber length, and the fiber/matrix bond strength, etc., the mechanism of the composite's fracture, however, seems not to have been fully clarified [222]. The findings demonstrate that the mechanical characteristics of composite materials improve as the percentage of frustules increases, and the key strengthening mechanisms involved are fracture deflection, frustules debonding and crushing. Stronger interactions between the matrix and fibers may enable the fiber to

debond rather than pull out, thereby allowing high energy to diffuse over a greater interfacial area [223]. The elastic moduli of 2 vol% silica composites were calculated using the rule of mixtures and the Eshelby model. Rule of mixtures exhibits very good agreement with the experimental elastic modulus for 2 vol% composite. The numerical modelling results of true stress-strain curves are summarized in figure 5.32 along with the experimental data presented in section 5.5. At first, it could be noted that the stress values increase linearly in the elastic region. This linear trend was also reported in a numerical work [224]. An increase in the number of elements (mesh density) is known to increase the accuracy of any finite element unit cell model. The best agreement between the numerical and experimental results of the stress-strain curves was achieved in the fine mesh model. While Poisson's ratio decreases from 0.17 to 0.001, the tensile strength of the composite increases from 83 MPa to 85 MPa. Combine these results with experimental 2 vol% composite (HF leached (1 N HF 15 min) and ball milled (500 rpm 1 h) 1200 °C heat-treated frustules filled epoxy composite), tensile strength increasea to 108 MPa. This difference can explain the Poisson's ratio effect.

CHAPTER 7

CONCLUSIONS

The present work investigated obtaining nano-silica particles by means of ball milling of the acid-leached natural and heat-treated frustules and used these nanopowders as reinforcing phases in an epoxy matrix. Besides, the mechanical properties of natural nano-structured diatom frustules were assessed.

The characterization of frustules showed that the as-received diatom frustule was composed of 90.08% silica with a minor quantity of other oxides. The heat treatment of as-received frustules at 900, 1000, 1100, and 1200 °C increased the crystallinity from 9.3 (25 °C) sequentially to about 20, 34, 39, and 46% without acid leaching. The mean particle size of the as-received frustule decreases from 15.6 μm to 14.7, 14.5, 14.4, and 13.7 μm after heat treatment at 900, 1000, 1100, and 1200°C and from 7.2 μm sequentially to 7.6, 7.6, 7.4, and 6.7 μm after ball milling.

Thermal treatment, acid leaching, and ball milling were performed to obtain nano-silica powder from diatom frustules. With the increase of the heat treatment temperature from 25 to 1200 °C, the mean powder size decreased from 14.2 μm to 10.6 μm 10% HCl. Furthermore, the mean powder size decreased from 7.5 μm to 5.8 μm 20% HCl. The mean particle size of the as-received and heat-treated frustules was almost reduced to half by applying ball milling (500 rpm 1 h) (HCl acid leaching). Undissolved frustule particles in the under-filter solution were weighed which were ~8, ~9, ~11, ~13, and ~18% 25, 900, 1000, 1100, and 1200 °C, respectively. The results showed that HCl acid is not effective in reducing the particle size of diatom frustules.

The percentage of crystal phase of natural frustule increased from 9.2% to about 12, 29, 35, and 42% when leached sequentially by 1, 3, 5, and 7 N HF solution for 15 min. This also confirmed a higher rate of amorphous phase dissolution with acid leaching of the as-received frustule. Furthermore, the increased percent crystallinity of heat-treated frustule without HF-leaching exhibited a further increase after acid leaching. The crystal phase percentage of the filtered acid-leached frustules also increased with increasing acid concentration and time of leaching; the crystallinity reached 50-60% when the acid concentration was increased to 7 N. With the increase in the heat treatment temperature

from 25 to 1200 °C, the mean powder size decreased from 774 nm to 547 nm and the crystallinity increased from 12% to 48%. Both acid leaching and heat treatment were found to be very effective in decreasing the particle size of the frustules. The amorphous silica was observed in between crystal silica grains and acid leaching removed the amorphous phase faster than the crystalline grains. This resulted in an easy fracture side during ball milling and a nano-size powder with a crystallinity between 12 to 48%. On the other side, the highest weight of under-filter nanopowder, 245 nm, was obtained by leaching (1 N HF and 15 min) 900 °C heat-treated frustules.

The tensile strength of epoxy increased from ~79 MPa (neat epoxy) to ~108 MPa in the 2 vol% silica composite, corresponding to a 37% increase. The increase in yield strength was about 50%. The fracture strain increased from 0.028 for neat epoxy to 0.0305 for 2 vol% of silica composite. The modulus of the epoxy resin increased from 4.23 GPa to 5.50 GPa with the addition of 2 vol% frustules. The increase in elastic modulus was about 30%. The increase in modulus of the nano structured frustules filled composites indicated an increase in the rigidity of epoxy. The elastic moduli of 2 vol% silica composites were also calculated using the rule of mixtures and the Eshelby model. The rule of mixtures demonstrated very good agreement with the experimental elastic modulus for 2 vol% composites.

Numerical modelling of 2 vol% silica filled epoxy composites was investigated and compared with experimental results. The best agreement between the numerical and experimental results of the stress-strain curves was achieved in the fine mesh model. While Poisson's ratio decreased from 0.17 to 0.001, the tensile strength of the composite increased from 83 MPa to 85 MPa. Combine these results with experimental 2 vol% composite (HF leached (1 N HF 15 min) and ball milled (500 rpm 1 h) 1200 °C heat-treated frustules filled epoxy composite), tensile strength increased to 108 MPa.

Microscopic analysis of the fracture surfaces of samples indicated that as the frustules content increased, the fracture surface appearance changed from wavy form in neat epoxy to ribbed (jagged) form. The elemental mapping results exhibited the existence of elements Si (45.53 wt%), O (53.09 wt%), and Al (1.38 wt%), on the HF leached and ball-milled 1200 °C heat-treated nano-structured frustules. The fracture surfaces of frustules showed that the measured crystalline grain sizes were between 425 and 685 nm fairly complying with the mean particle size of 1200 °C heat-treated frustules. Also, the micrographs demonstrated that the dispersion of frustules in the epoxy matrix was relatively uniform and that there was no agglomeration in the composites. There was

a significant amount of nano-silica particles in the extension direction of cracks which can absorb the rupture energy and prevent the propagation of cracks. While the volume percentage of frustules increased, the concentration on the fracture surfaces of nano-silica increased. Addiction to significantly higher content of nano-structured frustules led to induce massive sub-cracks or micro-cracks which could encounter more flaws during crack propagation in the nanocomposite.

REFERENCES

1. Liu, X.; Zhao, S. H.; Yang, Y.; Zhang, X. Y.; Wu, Y. P., Structure and properties of star-shaped solution-polymerized styrene-butadiene rubber and its co-coagulated rubber filled with silica/carbon black-I: morphological structure and mechanical properties. *Polym. Adv. Technol.* **2009,** *20* (11), 818-825.

2. Chen, J.; Lekawa-Raus, A.; Trevarthen, J.; Gizewski, T.; Lukawski, D.; Hazra, K.; Rahatekar, S. S.; Koziol, K. K. K., Carbon nanotube films spun from a gas phase reactor for manufacturing carbon nanotube film/carbon fibre epoxy hybrid composites for electrical applications. *Carbon* **2020,** *158*, 282-290.

3. Desai, A. V.; Haque, M. A., Mechanics of the interface for carbon nanotube–polymer composites. *Thin-Walled Structures* **2005,** *43* (11), 1787-1803.

4. Vahedi, F.; Eskandarzade, M.; Osouli-Bostanabad, K.; Tutunchi, A., Graphene nanosheets reinforced epoxy nanocomposites: mechanical and electrical properties evaluation. *Polymer Science, Series A* **2018,** *60* (6), 854-865.

5. Irez, A. B.; Bayraktar, E.; Miskioglu, I., Fracture toughness analysis of epoxy-recycled rubber-based composite reinforced with graphene nanoplatelets for structural applications in automotive and aeronautics. *Polymers* **2020,** *12* (2), 448.

6. Balazs, A. C.; Emrick, T.; Russell, T. P., Nanoparticle polymer composites: where two small worlds meet. *Science (New York, N.Y.)* **2006,** *314* (5802), 1107-10.

7. Krishnamoorti, R.; Vaia, R. A., Polymer nanocomposites. *Journal of Polymer Science Part B: Polymer Physics* **2007,** *45* (24), 3252-3256.

8. Schaefer, D. W.; Justice, R. S., How Nano Are Nanocomposites?. *Macromolecules* **2007,** *40* (24), 8501-8517.

9. Crawford, S. A.; Higgins, M. J.; Mulvaney, P.; Wetherbee, R., Nanostructure of the diatom frustule as revealed by atomic force and scanning electron microscopy. *Journal of Phycology* **2001,** *37* (4), 543-554.

10. Round, F. E.; Crawford, R. M.; Mann, D. G., *The Diatoms : biology & morphology of the genera*. Cambridge University Press: Cambridge [England]; New York, 1990.

11. Lund, J. W. G., Werner, D. [Ed.] 1977. The biology of diatoms. Bot. Monogr., V. 13. University of California Press, Berkeley and New York. *Limnology and Oceanography* **1979,** *24* (1), 200-200.

12. Sharma, N.; Simon, D. P.; Diaz-Garza, A. M.; Fantino, E.; Messaabi, A.; Meddeb-Mouelhi, F.; Germain, H.; Desgagné-Penix, I., Diatoms Biotechnology: Various Industrial Applications for a Greener Tomorrow. **2021,** *8*.

13. Zhao, J.; Gaddis, C.; Cai, Y.; Sandhage, K., Free-standing microscale structures of zirconia nanocrystals with biologically replicable 3-d shapes. *Journal of Materials Research* **2005,** *20*, 282-287.

14. Gaddis, C. S.; Sandhage, K. H., Freestanding microscale 3D polymeric structures with biologically-derived shapes and nanoscale features. *Journal of Materials Research* **2004,** *19* (9), 2541-2545.

15. Losic, D.; Mitchell, J. G.; Voelcker, N. H., Complex gold nanostructures derived by templating from diatom frustules. *Chemical communications (Cambridge, England)* **2005,** (39), 4905-7.

16. Sandhage, K. H.; Allan, S. M.; Dickerson, M. B.; Gaddis, C. S.; Shian, S.; Weatherspoon, M. R.; Cai, Y.; Ahmad, G.; Haluska, M. S.; Snyder, R. L.; Unocic, R. R.; Zalar, F. M.; Zhang, Y.; Rapp, R. A.; Hildebrand, M.; Palenik, B. P., Merging biological self-assembly with synthetic chemical tailoring: the potential for 3-d genetically engineered micro/nano-devices (3-D GEMS). *International Journal of Applied Ceramic Technology* **2005,** 2, 317–326.17.

17. Wee, K. M.; Rogers, T. N.; Altan, B. S.; Hackney, S. A.; Hamm, C., Engineering and medical applications of diatoms. *Journal of nanoscience and nanotechnology* **2005,** *5* (1), 88-91.

18. Liang, D.-t.; Readey, D. W., Dissolution kinetics of crystalline and amorphous silica in hydrofluori*f* hydrochloric acid mixtures. *Journal of the American Ceramic Society* **1987,** *70*, 570-577.

19. Nayak, S. K.; Mohanty, S.; Nayak, S. K., Thermal, electrical and mechanical properties of expanded graphite and micro-sic filled hybrid epoxy composite for electronic packaging applications. *Journal of Electronic Materials* **2020,** *49* (1), 212-225.

20. Nerilli, F.; Marino, M.; Vairo, G., A numerical failure analysis of multi-bolted joints in frp laminates based on basalt fibers. *Procedia Engineering* **2015,** *109*, 492-506.

21. Becker, O.; Varley, R.; Simon, G., Thermal stability and water uptake of high performance epoxy layered silicate nanocomposites. *European Polymer Journal* **2004,** *40*, 187-195.

22. Campbell, F. C., Manufacturing processes for advanced composites. 2003; p 1-517.

23. Camargo, P. H. C.; Satyanarayana, K. G.; Wypych, F., Nanocomposites: synthesis, structure, properties and new application opportunities. *Materials Research* **2009,** *12*, 1-39.

24. Hári, J.; Pukánszky, B., 8 - Nanocomposites: preparation, structure, and properties. in *applied plastics engineering handbook*, Kutz, M., Ed. William Andrew Publishing: Oxford, 2011; pp 109-142.

25. Piggott, M., Load Bearing Fibre Composites. **2002**.

26. Birkley, A. W., Rubbery materials and their compounds. *Journal of Polymer Science Part A: Polymer Chemistry* **1989,** *29* (8), 1223-1223.

27. Alexandre, M.; Dubois, P., Polymer-layered silicate nanocomposites: preparation, properties and uses of a new class of materials. *Materials Science and Engineering: R: Reports* **2000,** *28*, 1-63.

28. Mebert, A. M.; Baglole, C. J.; Desimone, M. F.; Maysinger, D., Nanoengineered silica: properties, applications and toxicity. food and chemical toxicology. *British Industrial Biological Research Association* **2017,** *109* (1), 753-770.

29. Idris, C. O. O. S. I. I. A. C. O. K. D. M. K., The suitability of local quartz sand in the production of bath crucibles. *International Journal of Scientific & Technology Research* **2017,** *6*, 126-128.

30. Panzeri, L., Mortar and surface dating with optically stimulated luminescence (OSL): Innovative techniques for the age determination of buildings. *Nuovo Cimento della Societa Italiana di Fisica C* **2013,** *36*, 205-216.

31. Martin, L. F.; Ackermans, N. L.; Richter, H.; Kircher, P.; Hummel, J.; Codron, D.; Clauss, M.; Hatt, J.-M., Macrowear effects of external quartz abrasives of different size and concentration in rabbits (Oryctolagus cuniculus). *Molecular and Developmental Evolution* **2021,** 338, 586– 597.

32. Tolstoy, A.; Lesovik, V.; Fediuk, R.; Amran, M.; Gunasekaran, M.; Vatin, N.; Vasiliev, Y., Production of greener high-strength concrete using russian quartz sandstone mine waste aggregates. *Materials* **2020,** *13*, 5575.

33. Linek, M.; Nita, P.; Żebrowski, W.; Wolka, P., Assessment of granite, quartz and syenite aggregate suitability intended for the application in case of transport pavement concrete. *IOP Conference Series: Materials Science and Engineering* **2019,** *471*, 032076.

34. Vatalis, K. I.; Charalambides, G.; Benetis, N. P., Market of high purity quartz innovative applications. *Procedia Economics and Finance* **2015,** *24*, 734-742.

35. Kondolf, G. M., PROFILE: Hungry Water: Effects of dams and gravel mining on river channels. *Environmental Management* **1997,** *21* (4), 533-551.

36. Weber, K. J., Book Review: Sand. R. Siever. Scientific American Library, New York, **1989,** *65*, 201-202.

37. Mizota, C.; Toh, N.; Matsuhisa, Y., Origin of cristobalite in soils derived from volcanic ash in temperate and tropical regions. *Geoderma* **1987,** *39* (4), 323-330.

38. Richard Drees, L.; Wilding, L. P.; Smeck, N. E.; Senkayi, A. L., Silica in soils: quartz and disordered silica polymorphs. In *Minerals in Soil Environments* **1989**;pp 913-974.

39. Gutiérrez-Castorena, M. d. C.; Effland, W. R., Pedogenic and biogenic siliceous features. In *Interpretation of Micromorphological Features of Soils and Regoliths*, Stoops, G.; Marcelino, V.; Mees, F., Eds. Elsevier: Amsterdam, **2010**; pp 471-496.

40. Kukartsev, V. A.; Cherepanov, A. I.; Kukartsev, V. V.; Tynchenko, V. S.; Kurashkin, S. O.; Sergienko, R. B.; Tynchenko, V. V.; Bashmur, K. A., Increasing the efficiency of foundry production by changing the technology of pretreatment with quartzite. **2022,** *12* (8), 1266.

41. Hasan, M.; Saidi, T.; Muyasir, A.; Alkhaly, Y. R.; Muslimsyah, M., Characteristic of calcined diatomaceous earth from aceh besar district - indonesia as cementitious binder characteristic of calcined diatomaceous earth from aceh besar district -*Indonesia As Cementitious Binder* **2020,** 933.

42. Gilchrist, J. D., 23 - Silica Bricks. In *Fuels, Furnaces and Refractories*, Gilchrist, J. D., Ed. Pergamon: **1977**; pp 273-283.

43. Dion, C.; Dufresne, A.; Jacob, M.; Perrault, G., Assessment of exposure to quartz, cristobalite and silicon carbide fibres (whiskers) in a silicon carbide plant. *The Annals of occupational hygiene* **2005,** *49*, 335-43.

44. de, S.; Magalhães, W.; Persegil, M. C., Silica Derived from Burned Rice Hulls. *Materials Research* **2002,** *5*.

45. Hassan, T.; Salam, A.; Khan, A.; Khan, S. U.; Khanzada, H.; Wasim, M.; Khan, M.; Kim, I.-S., Functional nanocomposites and their potential applications: A review. *Journal of Polymer Research* **2021,** *28*.

46. Prasertsri, S.; Rattanasom, N., Mechanical and damping properties of silica/natural rubber composites prepared from latex system. *Polymer Testing* **2011,** *30* (5), 515-526.

47. González-Jiménez, A.; Bernal-Ortega, P.; Salamanca, F. M.; Valentin, J. L., Shape-memory composites based on ionic elastomers. **2022,** *14* (6), 1230.

48. Irez, A. B.; Bayraktar, E.; Miskioglu, I., Design and mechanical-physical properties of epoxy-rubber based composites reinforced with nanoparticles. *Procedia Engineering* **2017,** *184*, 486-496.

49. Zou, H.; Wu, S.; Shen, J., Polymer/Silica nanocomposites: preparation, characterization, properties, and applications. *Chemical reviews* **2008,** *108*, 3893-957.

50. Shah, V.; Bhaliya, J.; Patel, G. M.; Deshmukh, K., Advances in polymeric nanocomposites for automotive applications: A review. **2022,** *33* (10), 3023-3048.

51. Singh, L. P.; Bhattacharyya, S. K.; Kumar, R.; Mishra, G.; Sharma, U.; Singh, G.; Ahalawat, S., Sol-Gel processing of silica nanoparticles and their applications. *Adv Colloid Interface Sci* **2014,** *214*, 17-37.

52. Lazareva, S.; Shikina, N.; Tatarova, L. E.; Ismagilov, Z., Synthesis of high-purity silica nanoparticles by sol-gel method. *Eurasian Chemico-Technological Journal* **2017,** *19*, 295.

53. da Rocha, E. B. D.; Linhares, F. N.; Gabriel, C. F. S.; de Sousa, A. M. F.; Furtado, C. R. G., Stress relaxation of nitrile rubber composites filled with a hybrid metakaolin/carbon black filler under tensile and compressive forces. *Applied Clay Science* **2018,** *151*, 181-188.

54. Zhao, S.; Xie, S.; Sun, P.; Zhao, Z.; Li, L.; Shao, X.; Liu, X.; Xin, Z., Synergistic effect of graphene and silicon dioxide hybrids through hydrogen bonding self-assembly in elastomer composites. *RSC Advances* **2018,** *8* (32), 17813-17825.

55. Mitryaeva, N. S.; Akimenko, S. S., Influence of multi-walled carbon nanotubes in carbon black mixture on rubber properties. *Procedia Engineering* **2016,** *152*, 689-693.

56. Geng, H.; Zhao, Y.; Liu, J.; Cui, Y.; Wang, Y.; Zhao, Q.; Wang, S., Hollow mesoporous silica as a high drug loading carrier for regulation insoluble drug release. *International journal of pharmaceutics* **2016,** *510* (1), 184-94.

57. Jiao, J.; Li, X.; Zhang, S.; Liu, J.; Di, D.; Zhang, Y.; Zhao, Q.; Wang, S., Redox and pH dual-responsive PEG and chitosan-conjugated hollow mesoporous silica for controlled drug release. *Materials science & engineering. C, Materials for biological applications* **2016,** *67*, 26-33.

58. Cheng, Y.-J.; Zeng, X.; Cheng, D.-B.; Xu, X.-D.; Zhang, X.-Z.; Zhuo, R.-X.; He, F., Functional mesoporous silica nanoparticles (MSNs) for highly controllable drug release and synergistic therapy. *Colloids and Surfaces B: Biointerfaces* **2016,** *145*, 217-225.

59. Alkimim, I. P.; Silva, L. L.; Cardoso, D., Synthesis of hybrid spherical silicas and application in catalytic transesterification reaction. *Microporous and Mesoporous Materials* **2017,** *254*, 37-44.

60. Maria Claesson, E.; Mehendale, N. C.; Klein Gebbink, R. J. M.; van Koten, G.; Philipse, A. P., Magnetic silica colloids for catalysis. *Journal of Magnetism and Magnetic Materials* **2007,** *311* (1), 41-45.

61. Anbarasu, G.; Malathy, M.; Karthikeyan, P.; Rajavel, R., Silica functionalized Cu(II) acetylacetonate Schiff base complex: An efficient catalyst for the oxidative condensation reaction of benzyl alcohol with amines. *Journal of Solid State Chemistry* **2017,** *253*, 305-312.

62. Gustafsson, H.; Holmberg, K., Emulsion-based synthesis of porous silica. *Adv Colloid Interface Sci* **2017,** *247*, 426-434.

63. Yu, H. S.; Rhee, K.-I.; Lee, C. K.; Yang, D.-H., Two-step ammoniation of by-product fluosilicic acid to produce high quality amorphous silica. *Korean Journal of Chemical Engineering* **2000,** *17* (4), 401-408.

64. Castillo, X.; Pizarro, J.; Ortiz, C.; Cid, H.; Flores, M.; De Canck, E.; Van Der Voort, P., A cheap mesoporous silica from fly ash as an outstanding adsorbent for sulfate in water. *Microporous and Mesoporous Materials* **2018,** *272*, 184-192.

65. Elineema, G.; Kim, J. K.; Hilonga, A.; Shao, G. N.; Kim, Y.-N.; Quang, D. V.; Sarawade, P. B.; Kim, H. T., Quantitative recovery of high purity nanoporous silica from waste products of the phosphate fertilizer industry. *Journal of Industrial and Engineering Chemistry* **2013,** *19* (1), 63-67.

66. Conradi, M., Nanosilica-reinforced polymer composites. *Materiali in Tehnologije* **2013,** *47*, 285-293.

67. Kaya, İ.; Gül, M.; Şenol, D., Synthesis and characterization of epoxy resins containing imine group and their curing processes with aromatic diamine. *Journal of Macromolecular Science, Part A* **2019,** *56* (6), 618-627.

68. Chen, G.; Zhang, Q.; Hu, Z.; Wang, S.; Wu, K.; Shi, J.; Liang, L.; Lu, M., Liquid crystalline epoxies bearing biphenyl ether and aromatic ester mesogenic units: Synthesis and thermal properties. *Journal of Macromolecular Science, Part A* **2019,** *56* (5), 484-495.

69. Gul, S.; Kausar, A.; Mehmood, M.; Muhammad, B.; Jabeen, S., Progress on epoxy/polyamide and inorganic nanofiller-based hybrids: introduction, application, and future potential. *Polym.-Plast. Technol. Eng.* **2016,** *55*.

70. H.P.S, A. K.; Fizree, H. M.; Bhat, A. H.; Jawaid, M.; Abdullah, C., Development and characterization of epoxy nanocomposites based on nano-structured oil palm ash. *Composites Part B Engineering* **2013,** *53*, 324-333.

71. Njuguna, J.; Pielichowski, K.; Alcock, J., Epoxy-based fibre reinforced nanocomposites. *Advanced Engineering Materials* **2007,** *9*, 835-847.

72. Dong, M.; Zhang, H.; Tzounis, L.; Santagiuliana, G.; Bilotti, E.; Papageorgiou, D. G., Multifunctional epoxy nanocomposites reinforced by two-dimensional materials: A review. *Carbon* **2021,** *185*, 57-81.

73. Teh, P. L.; Jaafar, M.; Md Akil, H.; Yeoh, C. K.; Seetharamu, K. N.; Wagiman, A. N. R.; Beh, K. S., The properties of epoxy resin coated silica fillers composites. *Materials Letters* **2007,** *61*, 2156-2158.

74. Imanaka, M.; Takeuchi, Y.; Nakamura, Y.; Nishimura, A.; Iida, T., Fracture toughness of spherical silica-filled epoxy adhesives. *International Journal of Adhesion and Adhesives* **2001,** *21* (5), 389-396.

75. Teh, P. L.; Jaafar, M.; Md Akil, H.; Seetharamu, K. N.; Wagiman, A. N. R.; Beh, K. S., High filled epoxy composites for electronic packaging application. **2007**; p 275-281.

76. Guadagno, L.; Pantelakis, S.; Strohmayer, A.; Raimondo, M., High-Performance properties of an aerospace epoxy resin loaded with carbon nanofibers and glycidyl polyhedral oligomeric silsesquioxane. **2022,** *9* (4), 222.

77. Landry, B.; LaPlante, G.; LeBlanc, L. R., Environmental effects on mode II fatigue delamination growth in an aerospace grade carbon/epoxy composite. *Composites Part A: Applied Science and Manufacturing* **2012,** *43* (3), 475-485.

78. Zhao, Y.; Chen, Z.-K.; Liu, Y.; Xiao, H.-M.; Feng, Q.-P.; Fu, S.-Y., Simultaneously enhanced cryogenic tensile strength and fracture toughness of epoxy resins by carboxylic nitrile-butadiene nano-rubber. *Composites Part A: Applied Science and Manufacturing* **2013,** *55*, 178-187.

79. Wetzel, B.; Rosso, P.; Haupert, F.; Friedrich, K., Epoxy nanocomposites - fracture and toughening mechanisms. *Engineering Fracture Mechanics* **2006,** *73*, 2375-2398.

80. Hartwig, A.; Sebald, M.; Pütz, D.; Aberle, L., Preparation, characterisation and properties of nanocomposites based on epoxy resins – An Overview. *Macromolecular Symposia* **2005,** *221* (1), 127-136.

81. Sarı, M.; Gemi, L.; Yazman, S.; Akdemir, A., Investigating mechanical properties of SiO_2 nanoparticle reinforced epoxy/nanocomposites. **2016**.

82. Dinesh, T.; Kadirvel, A.; Hariharan, P., Thermo-mechanical and wear behaviour of surface-treated pineapple woven fibre and nano-silica dispersed mahua oil toughened epoxy composite. *Silicon* **2020**, 10.

83. Dani, M. S. H.; Venkateshwaran, N., Role of surface functionalized crystalline nano-silica on mechanical, fatigue and drop load impact damage behaviour of

effective stacking sequenced e-glass fibre-reinforced epoxy resin composite. *Silicon* **2020**, 10.

84. Suresha, B.; Divya, G. S.; Hemanth, G.; Somashekar, H. M., Physico-mechanical properties of nano silica-filled epoxy-based mono and hybrid composites for structural applications. *Silicon* **2020**.

85. Albooyeh, A.; Bayat, M.; Rafieian, P.; Dadrasi, A.; Khatibi, M. M., Silica aerogel/epoxy nanocomposites: Mechanical, vibrational, and morphological properties. *Journal of Applied Polymer Science* **2020,** *137* (43), 49338.

86. Prajapati, J. K.; Gupta, M. K., Development of hybrid glass fibre/nano silica composite for sustainable product: mechanical, dynamic mechanical and optical properties. *Materials Research Express* **2019,** *6* (11).

87. Gokuldass, R.; Ramesh, R., Mechanical and low velocity impact behaviour of intra-ply glass/kevlar fibre reinforced nano-silica and micro-rubber modified epoxy resin hybrid composite. *Materials Research Express* **2019,** *6* (5), 10.

88. Dilfi, K. F. A.; Che, Z. J.; Xian, G. J., Grafting of nano-silica onto ramie fiber for enhanced mechanical and interfacial properties of ramie/epoxy composite. *Journal of Zhejiang University-Science A* **2019,** *20* (9), 660-674.

89. Asif, M.; Ramezani, M.; Khan, K. A.; Khan, M. A.; Aw, K. C., Investigation of the strain-rate-dependent mechanical behavior of a photopolymer matrix composite with fumed nano-silica filler. *Polym. Eng. Sci.* **2019,** *59* (8), 1695-1700.

90. Tian, J.; Tan, Y.; Wang, X.; Gao, L.; Zhang, Z.; Tang, B., Investigation on mechanical properties and reinforced mechanisms of hyperbranched polyesters functionalized nano-silica modified epoxy composites. *Materials Research Express* **2019,** *6* (8), 085347.

91. Maghsoudi, K.; Motahari, S., Mechanical, thermal, and hydrophobic properties of silica aerogel–epoxy composites. *Journal of Applied Polymer Science* **2018,** *135* (3), 45706.

92. Pham, T. D.; Vu, C. M.; Choi, H. J., Enhanced fracture toughness and mechanical properties of epoxy resin with rice husk-based nano-silica. *Polymer Science Series A* **2017,** *59* (3), 437-444.

93. Feng, Q. H.; Yang, J. P.; Yu, Y. L.; Tian, F. Y.; Zhang, B. M.; Feng, M. J.; Wang, S. B., The ionic conductivity, mechanical performance and phase structural electrolytes based on polyethylene and nano-silica. *Mater. Sci. Eng. B-Adv. Funct. Solid-State Mater.* **2017,** *219*, 37-44.

94. Abenojar, J.; Tutor, J.; Ballesteros, Y.; del Real, J. C.; Martinez, M. A., Erosion-wear, mechanical and thermal properties of silica filled epoxy nanocomposites. *Compos. Pt. B-Eng.* **2017,** *120*, 42-53.

95. Constantinescu, D. M.; Apostol, D. A.; Picu, C. R.; Krawczyk, K.; Sieberer, M., Mechanical properties of epoxy nanocomposites reinforced with functionalized silica nanoparticles. *Procedia Structural Integrity* **2017,** *5*, 647-652.

96. Shariati, M.; Farzi, G.; Dadrasi, A., Mechanical properties and energy absorption capability of thin-walled square columns of silica/epoxy nanocomposite. *Construction and Building Materials* **2015,** *78*, 362-368.

97. Afzal, A.; Siddiqi, H. M.; Mujahid, A.; Saeed, S., AFM substantiation of the fracture behavior and mechanical properties of sol–gel derived silica packed epoxy networks. *Journal of Sol-Gel Science and Technology* **2012,** *61* (1), 44-48.

98. Nikje, M. M. A.; Garmarudi, A. B.; Tehrani, Z. M.; Haghshenas, M.; Shakhesi, S., Thermal and mechanical evaluation of epoxy resin composites by synthesis of amine-based coupling agent-nano silica complex. *Polym.-Plast. Technol. Eng.* **2011,** *50* (6), 646-650.

99. Mortazavi, B.; Ahzi, S.; Bardon, J.; Laachachi, A.; Ruch, D.; Tms, Investigation of mechanical properties of silica/epoxy nano-composites by molecular dynamics and finite element modeling. **2011**; p 117-120.

100. Rostamiyan, Y.; Mashhadzadeh, A. H.; SalmanKhani, A., Optimization of mechanical properties of epoxy-based hybrid nanocomposite: Effect of using nano silica and high-impact polystyrene by mixture design approach. *Materials & Design* **2014,** *56*, 1068-1077.

101. Aggarwal, S. L., Rubber compounding, principles, materials, and techniques. *Journal of Polymer Science Part C: Polymer Letters* **1990,** *28* (6), 210-211.

102. Dhanorkar, R.; Mohanty, S.; Gupta, V., Synthesis of functionalized styrene butadiene rubber and its applications in sbr–silica composites for high performance tire applications. *Industrial & Engineering Chemistry Research* **2021,** *60*.

103. Hewitt, N., Compounding precipitated silica in elastomers. **2007**.

104. Bach, Q.-V.; Vu, C. M.; Vu, H. T., Effects of Co-Silanized Silica on the Mechanical properties and thermal characteristics of natural rubber/styrene-butadiene rubber blend. *Silicon* **2020,** *12* (8), 1799-1809.

105. Rajaee, P.; Ghasemi, F. A.; Fasihi, M.; Saberian, M., Effect of styrene-butadiene rubber and fumed silica nano-filler on the microstructure and mechanical properties of glass fiber reinforced unsaturated polyester resin. *Compos. Pt. B-Eng.* **2019,** *173*.

106. Tian, Q. F.; Tang, Y.; Ding, T.; Li, X. H.; Zhang, Z. J., Effect of nano-silica surface-capped by bis 3-(triethoxysilyl)propyl tetrasulfide on the mechanical properties of styrene-butadiene rubber/butadiene rubber nanocomposites. *Composites Communications* **2018,** *10*, 190-193.

107. Bansod, N. D.; Das, C., Studies on mechanical, rheological, thermal and morphological properties of in situ silica-filled butadiene rubber composites. *Plast. Rubber Compos.* **2018,** *47* (8), 345-351.

108. Yin, C.; Zhang, Q.; Gu, J.; Zhao, Z.; Zheng, J.; Gong, G.; Liang, T.; Zhang, H., Cure Characteristics and Mechanical Properties of Vinyltriethoxysilane Grafted Styrene-Butadiene Rubber/Silica Blends. *Polym.-Plast. Technol. Eng.* **2012,** *51* (12), 1218-1222.

109. Arayapranee, W., Rubber Abrasion resistance. **2012**.

110. Posadas, P.; Gonzalez-Jimenez, A.; Valentin, J. L., Natural rubber: Properties, behavior and uses. **2016**; pp 1-24.

111. Chuayjuljit, S.; Eiumnoh, S.; Potiyaraj, P., Using silica from rice husk as a reinforcing filler in natural rubber. **2001,** *26*.

112. Salim, Z., The effect of high purity rice husk silica synthesised using solvent-thermal extraction method on the properties of natural rubber compounds. **2018**.

113. Muhammud, A. M.; Gupta, N. K., Nanostructured SiO_2 material: synthesis advances and applications in rubber reinforcement. *RSC Adv* **2022,** *12* (29), 18524-18546.

114. Morton, M., Rubber Technology, 2nd Edition. **1973**.

115. Leblanc, J. L., Rubber–filler interactions and rheological properties in filled compounds. *Progress in Polymer Science* **2002,** *27* (4), 627-687.

116. Ciesielski, A., An introduction to rubber technology. **1999**.

117. Zhang, X. M.; Xue, X. D.; Jia, H. B.; Wang, J. Y.; Ji, Q. M.; Xu, Z. D., Influence of ionic liquid on the polymer-filler coupling and mechanical properties of nano-silica filled elastomer. *Journal of Applied Polymer Science* **2017,** *134* (7).

118. Liu, J.; Tian, X. H.; Sun, J. Y.; Wang, S. Y.; Duan, J. C., Mechanical properties and thermal resistance of natural rubber nanocomposite reinforced with quaternized polyvinyl alcohol/silica nanoclusters. *Journal of Nano Research* **2016,** *43*, 46-56.

119. Tangudom, P.; Thongsang, S.; Sombatsompop, N., Cure and mechanical properties and abrasive wear behavior of natural rubber, styrene–butadiene rubber and their blends reinforced with silica hybrid fillers. *Materials & Design* **2014,** *53*, 856-864.

120. Rassamee, W.; Thaijaroen, W.; Pongprayoon, T., Mechanical and Dynamic properties of silica-filled rubber compounds. *Advances in Chemical Engineering*, **2013,** 781, 475.

121. Meera, A. P.; Tlili, R.; Boudenne, A.; Ibos, L.; Poornima, V.; Thomas, S.; Candau, Y., Thermophysical and mechanical properties of TiO_2 and silica nanoparticle-filled natural rubber composites. *J. Elastomer Plast.* **2012,** *44* (4), 369-382.

122. Arun, K. J.; Francis, P. J. J.; Joseph, R., Mechanical properties of nr latex- nano silica composites. *Optoelectronics and Advanced Materials-Rapid Communications* **2010,** *4* (10), 1520-1525.

123. Salimi, D.; Khorasani, S. N.; Abadchi, M. R.; Veshare, S. J., Optimization of physico-mechanical properties of silica-filled NR/SBR compounds. *Adv. Polym. Technol.* **2009,** *28* (4), 224-232.

124. Liu, J. W.; Wu, C. F.; Zhang, P.; Zhao, S. G., Effects of cyclohexylamine modified silica on the mechanical properties of filled natural rubber. *J. Macromol. Sci. Part B-Phys.* **2008,** *47* (4), 689-700.

125. Reincke, K.; Grellmann, W.; Heinrich, G., Investigation of mechanical and fracture mechanical properties of elastomers filled with precipitated silica and

nanofillers based upon layered silicates. *Rubber Chem. Technol.* **2004,** *77* (4), 662-677.

126. Jong, L., Improved mechanical properties of silica reinforced rubber with natural polymer. *Polymer Testing* **2019,** *79*, 106009.

127. Vrieling, E. G.; Beelen, T. P. M.; van Santen, R. A.; Gieskes, W. W. C., Diatom silicon biomineralization as an inspirational source of new approaches to silica production. *J Biotechnol* **1999,** *70* (1-3), 39-51.

128. Parkinson, J.; Gordon, R., Beyond micromachining: the potential of diatoms. *Trends in biotechnology* **1999,** *17* (5), 190-6.

129. Fuhrmann, T.; Landwehr, S.; El Rharbi-Kucki, M.; Sumper, M., Diatoms as living photonic crystals. *Applied Physics B* **2004,** *78* (3), 257-260.

130. Almqvist, N.; Delamo, Y.; Smith, B. L.; Thomson, N. H.; Bartholdson, A.; Lal, R.; Brzezinski, M.; Hansma, P. K., Micromechanical and structural properties of a pennate diatom investigated by atomic force microscopy. *Journal of microscopy* **2001,** *202* (Pt 3), 518-32.

131. Anderson, M. W.; Holmes, S. M.; Hanif, N.; Cundy, C. S., Hierarchical pore structures through diatom zeolitization. **2000,** *39* (15), 2707-2710.

132. Bradbury, J., Nature's Nanotechnologists: Unveiling the secrets of diatoms. *PLOS Biology* **2004,** *2* (10), 306.

133. Cai, X.; Zhu, G.; Zhang, W.; Zhao, H.; Wang, C.; Qiu, S.; Wei, Y., Diatom-templated synthesis of ordered meso/macroporous hierarchical materials. **2006,** *18*, 3641-3645.

134. Gordon, R.; Parkinson, J., Potential roles for diatomists in nanotechnology. *Journal of nanoscience and nanotechnology* **2005,** *5* (1), 35-40.

135. Aitken, Z.; Luo, S.; Reynolds, S.; Thaulow, C.; Greer, J., Microstructure provides insights into evolutionary design and resilience of Coscinodiscus sp. frustule. *Proceedings of the National Academy of Sciences of the United States of America* **2016,** *113*.

136. Soleimani, M.; van Breemen, L. C. A.; Maddala, S. P.; Joosten, R. R. M.; Wu, H.; Schreur-Piet, I.; van Benthem, R. A. T. M.; Friedrich, H., In Situ manipulation and micromechanical characterization of diatom frustule constituents using focused ion beam scanning electron microscopy. **2021,** *5* (12), 2100638.

137. Zgłobicka, I.; Gluch, J.; Liao, Z.; Werner, S.; Guttmann, P.; Li, Q.; Bazarnik, P.; Płociński, T.; Andrzej, W.; Kurzydłowski, K. J., Insight into diatom frustule structures using various imaging techniques. *Scientific Reports* **2021,** *11*, 14555.

138. Rea, I.; Terracciano, M.; De Stefano, L., Synthetic vs Natural: Diatoms bioderived porous materials for the next generation of healthcare nanodevices. *Advanced healthcare materials* **2017,** *6* (3).

139. Zurzolo, C.; Bowler, C., Exploring bioinorganic pattern formation in diatoms. A story of polarized trafficking. *Plant physiology* **2002,** *127*, 1339-45.

140. Cai, Y.; Allan, S. M.; Sandhage, K. H.; Zalar, F. M., Three-dimensional magnesia-based nanocrystal assemblies via low-temperature magnesiothermic reaction of diatom microshells. *Journal of the American Ceramic Society* **2005,** *88* (7), 2005-2010.

141. Scala, S.; Bowler, C., Molecular insights into the novel aspects of diatom biology. *Cellular and molecular life sciences : CMLS* **2001,** *58*, 1666-73.

142. John P. Smol, E. F. S., The Diatoms: Applications for the environmental and earth sciences. *Cambridge University Press* **2010**.

143. Werner, D., *The Biology of Diatoms*. University of California Press: Berkeley, **1977**.

144. Ongerth, J.; Hutton, P., DE filtration to remove cryptosporidium. *Journal American Water Works Association - J AMER WATER WORK ASSN* **1997,** *89*, 39-46.

145. Mishra, M.; Arukha, A. P.; Bashir, T.; Yadav, D.; Prasad, G., All new faces of diatoms: potential source of nanomaterials and beyond. *Frontiers in microbiology* **2017,** *8*, 1239.

146. Sardo, A.; Orefice, I.; Balzano, S.; Barra, L.; Romano, G., Mini-Review: Potential of diatom-derived silica for biomedical applications. **2021,** *11* (10), 4533.

147. Jamali, A. A.; Akbari, F.; Ghorakhlu, M. M.; de la Guardia, M.; Yari Khosroushahi, A., Applications of diatoms as potential microalgae in nanobiotechnology. *BioImpacts : BI* **2012,** *2* (2), 83-9.

148. Wang, J.-K.; Seibert, M., Prospects for commercial production of diatoms. *Biotechnology for Biofuels* **2017,** *10* (1), 16.

149. Bayu, A.; Rachman, A.; Noerdjito, D.; Putra, M.; Widayatno, W., High-value chemicals from marine diatoms: a biorefinery approach. *IOP Conference Series: Earth and Environmental Science* **2020,** *460*, 012012.

150. Zobi, F., Diatom biosilica in targeted drug delivery and biosensing applications: recent studies. **2022,** *2* (2), 342-360.

151. Rea, I.; De Stefano, L., Recent advances on diatom-based biosensors. *Sensors* **2019,** *19*, 5208.

152. Yang, J.; Zhen, L.; Ren, F.; Campbell, J.; Rorrer, G. L.; Wang, A. X., Ultra-sensitive immunoassay biosensors using hybrid plasmonic-biosilica nanostructured materials. **2015,** *8* (8), 659-667.

153. Dolatabadi, J. E. N.; Guardia, M. d. l. J. T. i. A. C., Applications of diatoms and silica nanotechnology in biosensing, drug and gene delivery, and formation of complex metal nanostructures. **2011,** *30*, 1538-1548.

154. Bozarth, A.; Maier, U. G.; Zauner, S., Diatoms in biotechnology: modern tools and applications. *Applied microbiology and biotechnology* **2009,** *82* (2), 195-201.

155. Kuczynska, P.; Jemiola-Rzeminska, M.; Strzalka, K., Photosynthetic pigments in diatoms. *Mar Drugs* **2015,** *13* (9), 5847-81.

156. Hussein, H.; Abdullah, M., Anticancer Compounds Derived from Marine Diatoms. *Marine Drugs* **2020,** *18*, 356.

157. Brocks, J. J.; Buick, R.; Logan, G. A.; Summons, R. E., Composition and syngeneity of molecular fossils from the 2.78 to 2.45 billion-year-old Mount Bruce Supergroup, Pilbara Craton, Western Australia. *Geochimica et Cosmochimica Acta* **2003,** *67* (22), 4289-4319.

158. Knothe, G., Improving biodiesel fuel properties by modifying fatty ester composition. *Energy & Environmental Science* **2009,** *2* (7), 759-766.

159. Bik, H. M.; Porazinska, D. L.; Creer, S.; Caporaso, J. G.; Knight, R.; Thomas, W. K., Sequencing our way towards understanding global eukaryotic biodiversity. *Trends in ecology & evolution* **2012,** *27* (4), 233-43.

160. Tossavainen, M.; Lahti, K.; Edelmann, M.; Eskola, R.; Lampi, A.-M.; Piironen, V.; Korvonen, P.; Ojala, A.; Romantschuk, M., Integrated utilization of microalgae cultured in aquaculture wastewater: wastewater treatment and production of valuable fatty acids and tocopherols. *Journal of Applied Phycology* **2019,** *31* (3), 1753-1763.

161. Choi, H.-J., Parametric study of brewery wastewater effluent treatment using Chlorella vulgaris microalgae. *Environmental Engineering Research* **2016,** *21* (4), 401-408.

162. El-Kassas, H. Y.; Mohamed, L. A., Bioremediation of the textile waste effluent by Chlorella vulgaris. *The Egyptian Journal of Aquatic Research* **2014,** *40* (3), 301-308.

163. Aggrey, P.; Nartey, M.; Kan, Y.; Cvjetinovic, J.; Andrews, A.; Salimon, A. I.; Dragnevski, K. I.; Korsunsky, A. M., On the diatomite-based nanostructure-preserving material synthesis for energy applications. *RSC Advances* **2021,** *11* (51), 31884-31922.

164. Nagao, R.; Kato, K.; Suzuki, T.; Ifuku, K.; Uchiyama, I.; Kashino, Y.; Dohmae, N.; Akimoto, S.; Shen, J.-R.; Miyazaki, N.; Akita, F., Structural basis for energy harvesting and dissipation in a diatom PSII–FCPII supercomplex. *Nature Plants* **2019,** *5*, 1.

165. Tang, X.; Wen, G.; Song, Y., Novel scalable synthesis of porous silicon/carbon composite as anode material for superior lithium-ion batteries. *Journal of Alloys and Compounds* **2018,** *739*, 510-517.

166. Maeda, H.; Matsumoto, M.; Maeda, Y.; Egashira, Y.; Tanaka, T.; Kasuga, T., Utilization of diatom frustules for thermal management applications. *Journal of Applied Phycology* **2017,** *29* (4), 1907-1911.

167. Hasan, M.; Saidi, T.; Afifuddin, M., Mechanical properties and absorption of lightweight concrete using lightweight aggregate from diatomaceous earth. *Construction and Building Materials* **2021,** *277*, 122324.

168. Li, J.; Zhang, W.; Li, C.; Monteiro, P. J. M., Green concrete containing diatomaceous earth and limestone: Workability, mechanical properties, and life-cycle assessment. *Journal of Cleaner Production* **2019,** *223*, 662-679.

169. Lyu, S.; Wang, Y.; Han, H.; Ding, C.; Li, D.; Wang, J.-K.; Zhang, J.; Huang, J.; Sun, D.; Yu, P., Microstructure characterization and mechanical properties of Al-matrix composites reinforced by artificially-cultured diatom frustules. *Materials & Design* **2021,** *206*, 109755.

170. Li, Q.; Gluch, J.; Liao, Z.; Posseckardt, J.; Clausner, A.; Łępicka, M.; Grądzka-Dahlke, M.; Zschech, E., Morphology and mechanical properties of fossil diatom frustules from genera of ellerbeckia and melosira. *Nanomaterials* **2021,** *11*, 1615.

171. Hamm, C. E.; Merkel, R.; Springer, O.; Jurkojc, P.; Maier, C.; Prechtel, K.; Smetacek, V., Architecture and material properties of diatom shells provide effective mechanical protection. *Nature* **2003,** *421* (6925), 841-843.

172. Tsai, W.-T.; Lai, C.-W.; Hsien, K.-J., Characterization and adsorption properties of diatomaceous earth modified by hydrofluoric acid etching. *Journal of Colloid and Interface Science* **2006,** *297* (2), 749-754.

173. Zhang, D.; Wang, Y.; Zhang, W.; Pan, J.; Cai, J., Enlargement of diatom frustules pores by hydrofluoric acid etching at room temperature. *Journal of Materials Science* **2011,** *46*, 5665-5671.

174. Reka, A. A.; Pavlovski, B.; Fazlija, E.; Berisha, A.; Pacarizi, M.; Daghmehchi, M.; Sacalis, C.; Jovanovski, G.; Makreski, P.; Oral, A., Diatomaceous earth: characterization, thermal modification, and application. *Open Chemistry* **2021,** *19* (1), 451-461.

175. Meradi, H.; Atoui, L.; Bahloul, L.; Boubendira, K.; Bouazdia, A.; Ismail, F. In Characterization by thermal analysis of natural kieselguhr and sand for industrial application. *International Conference on Technologies and Materials for Renewable Energy, Environment and Sustainability (TMREES),* Beirut, LEBANON, Apr 17-20; **2015**; pp 1282-1288.

176. Ouis, D.; El Kebir, A.; Moulefera, I.; Sabantina, L.; Abdelghani, B., Synthesis, characterization and adsorption of bisphenol a using novel hybrid materiel produced from pani matrix reinforced by kieselguhr. *Journal of Inorganic and Organometallic Polymers and Materials* **2022,** *32,* 1-11.

177. Le, T. D. H.; Bonani, W.; Speranza, G.; Sglavo, V.; Ceccato, R.; Maniglio, D.; Motta, A.; Migliaresi, C., Processing and characterization of diatom nanoparticles and microparticles as potential source of silicon for bone tissue engineering. *Materials Science & Engineering C-Materials for Biological Applications* **2016,** *59*, 471-479.

178. Gulturk, E.; Guden, M., Thermal and acid treatment of diatom frustules. *Journal of Achievements in Materials and Manufacturing Engineering* **2011,** *46*, 196-203.

179. Zeren, D.; Guden, M., The increased compression strength of an epoxy resin with the addition of heat-treated natural nano-structured diatom frustules. *Journal of Composite Materials* **2016,** *51*.

180. Zeren, D.; Kesici, K.; Sukatar, A.; Guden, M., The shape and size effect of the diatom frustule addition on the compression behavior of an epoxy. *Materials Science Forum* **2018,** *915*.

181. Taşdemirci, A.; Yüksel, S.; Karsu, D.; Gültürk, E.; Hall, I. W.; Güden, M., Diatom frustule-filled epoxy: Experimental and numerical study of the quasi-static and high strain rate compression behavior. *Materials Science and Engineering: A* **2008,** *480* (1), 373-382.

182. Gültürk, E. A.; Güden, M.; Taşdemirci, A., Calcined and natural frustules filled epoxy matrices: The effect of volume fraction on the tensile and compression behavior. *Composites Part B: Engineering* **2013,** *44* (1), 491-500.

183. Galotta, A.; Giust, E.; Bortolotti, M.; Soraru, G. D.; Sglavo, V. M.; Biesuz, M., Cold sintering of diatomaceous earth. *Journal of the American Ceramic Society* **2021,** *104* (9), 4329-4340.

184. Sapiai, N.; Jumahat, A.; Jawaid, M.; Midani, M.; Khan, A., Tensile and flexural properties of silica nanoparticles modified unidirectional kenaf and hybrid glass/kenaf epoxy composites. **2020,** *12* (11), 2733.

185. Awad, S. A.; Khalaf, E. M., Investigation of improvement of properties of polypropylene modified by nano silica composites. *Composites Communications* **2019,** *12*, 59-63.

186. Dileep, P.; Jacob, S.; Chandra, C. S. J.; Dominic, C. D. M.; Poornima, M. P.; Rappai, J. P.; Narayanankutty, S. K., Functionalized nanosilica for vulcanization efficiency and mechanical properties of natural rubber composites. *Silicon* **2022,** *14* (8), 4411-4422.

187. Wang, Y.-q.; Guo, Y.; Cui, R.-x.; Wang, Z.-m.; Wu, Y.-l., Preparation and mechanical properties of nano-silica/UPR polymer composite. **2014,** *21* (4), 471-477.

188. Carneiro, M., Preparation and characterization of nano silica from equisetum arvenses. *Journal of Bioprocessing & Biotechniques* **2015,** *05*.

189. Saleh, N.; Ibrahim, R.; Salman, A., Characterization of nano-silica prepared from local silica sand and its application in cement mortar using optimization technique. *Advanced Powder Technology* **2015,** *26*.

190. El-Didamony, H.; El-Fadaly, E.; Amer, A. A.; Abazeed, I. H., Synthesis and characterization of low cost nanosilica from sodium silicate solution and their applications in ceramic engobes. *Boletín de la Sociedad Española de Cerámica y Vidrio* **2020,** *59* (1), 31-43.

191. Akl, M.; Ibrahim, A., Preparation and characterization of silica nanoparticles by wet mechanical attrition of white and yellow sand. *Journal of Nanomedicine & Nanotechnology* **2013,** *04*.

192. Purcar, V.; Rădiţoiu, V.; Nichita, C.; Bălan, A.; Rădiţoiu, A.; Căprărescu, S.; Raduly, F. M.; Manea, R.; Şomoghi, R.; Nicolae, C.-A.; Raut, I.; Jecu, L., Preparation and characterization of silica nanoparticles and of silica-gentamicin nanostructured solution obtained by microwave-assisted synthesis. **2021,** *14* (8), 2086.

193. Arasuna, A.; Okuno, M., Structural change of the frustule of diatom by thermal treatment. *Geoscience Letters* **2018,** *5*.

194. Taya, M. a. R. J. A., Metal matrix composites : thermomechanical behavior. *Oxford, England.: Pergamon Press. 264* **1989**.

195. Douglas, E. J., The determination of the elastic field of an ellipsoidal inclusion and related problems. *Proceedings of the Royal Society A* **1957**, 376-396.

196. Mori, T.; Tanaka, K., Average stress in matrix and average elastic energy of materials with misfitting inclusions. *Acta Metallurgica* **1973,** *21* (5), 571-574.

197. Withers, P. J.; Stobbs, W. M.; Pedersen, O. B., The application of the eshelby method of internal stress determination to short fibre metal matrix composites. *Acta Metallurgica* **1989,** *37* (11), 3061-3084.

198. Hsueh, C.-H., Young's modulus of unidirectional discontinuous-fibre composites. *Composites Science and Technology* **2000,** *60*, 2671-2680.

199. Tandon, G. P.; Weng, G. J., The effect of aspect ratio of inclusions on the elastic properties of unidirectionally aligned composites. **1984,** *5* (4), 327-333.

200. Gendron-Badou, A. c.; Coradin, T.; Maquet, J.; Fröhlich, F.; Livage, J., Spectroscopic characterization of biogenic silica. *Journal of Non-Crystalline Solids* **2003,** *316*, 331-337.

201. Gendron-Badou, A. c.; Coradin, T.; Maquet, J.; Fröhlich, F.; Livage, J., Spectroscopic characterization of biogenic silica. *Journal of Non-Crystalline Solids* **2003,** *316* (2), 331-337.

202. Isaacs, C. M., Influence of rock composition on kinetics of silica phase changes in the Monterey Formation, Santa Barbara area, California. *Geology* **1982,** *10* (6), 304-308.

203. Arasuna, A.; Okuno, M.; Okudera, H.; Mizukami, T.; Arai, S.; Katayama, S. i.; Koyano, M.; Ito, N., Structural changes of synthetic opal by heat treatment. *Physics and Chemistry of Minerals* **2013,** *40*.

204. Soman, I.; Selvadurai, S.; Alagumalai, V.; Kakur, N., Effect of silica nanoparticles on mechanical and thermal properties of neat epoxy and filament wounded E-glass/epoxy and basalt/epoxy composite tubes. *Materials Research Express* **2019,** *6*.

205. Evans, K. E.; Nkansah, M. A.; Hutchinson, I. J.; Rogers, S. C., Molecular network design. *Nature* **1991,** *353* (6340), 124-124.

206. Lempriere, B. M., Poisson's ratio in orthotropic materials. **1968,** *6* (11), 2226-2227.

207. Alderson, A.; Alderson, K. L., Auxetic materials. **2007,** *221* (4), 565-575.

208. Wang, Z.; Hu, H., Auxetic materials and their potential applications in textiles. *Textile Research Journal* **2014,** *84*.

209. Lakes, R., Foam Structures with a Negative Poisson's Ratio. **1987,** *235* (4792), 1038-1040.

210. Chan, N.; Evans, K. E., Fabrication methods for auxetic foams. *Journal of Materials Science* **1997,** *32* (22), 5945-5953.

211. Verma, P.; He, C.; Griffin, A. C., Implications for auxetic response in liquid crystalline polymers: X-Ray scattering and space-filling molecular modeling. **2020,** *257* (10), 2000261.

212. Baughman, R. H.; Shacklette, J. M.; Zakhidov, A. A.; Stafström, S., Negative Poisson's ratios as a common feature of cubic metals. *Nature* **1998,** *392* (6674), 362-365.

213. Keskar, N. R.; Chelikowsky, J. R., Structural properties of nine silica polymorphs. *Physical Review B* **1992,** *46* (1), 1-13.

214. Yeganeh-Haeri, A.; Weidner, D. J.; Parise, J. B., Elasticity of agr-Cristobalite: A Silicon dioxide with a negative poisson's ratio. *Science (New York, N.Y.)* **1992,** *257* (5070), 650-2.

215. Grima, J. N.; Jackson, R.; Alderson, A.; Evans, K. E., Do zeolites have negative poisson's ratios? **2000,** *12* (24), 1912-1918.

216. Guo, C. Y.; Wheeler, L. T. J. J. o. T. M.; Solids, P. o., Extreme poisson's ratios and related elastic crystal properties. **2006,** *54*, 690-707.

217. Alderson, A.; Evans, K. E., Deformation mechanisms leading to auxetic behaviour in the α-cristobalite and α-quartz structures of both silica and germania. *Journal of Physics: Condensed Matter* **2009,** *21* (2), 025401.

218. Kimizuka, H.; Kaburaki, H.; Kogure, Y., Mechanism for negative poisson ratios over the transition of cristobalite, a molecular-dynamics study. *Physical Review Letters* **2000,** *84* (24), 5548-5551.

219. Kimizuka, H.; Kaburaki, H., Molecular dynamics study of the high-temperature elasticity of SiO_2 polymorphs: Structural phase transition and elastic anomaly. **2005,** *242* (3), 607-620.

220. Assidi, M.; Ganghoffer, J.-F., Composites with auxetic inclusions showing both an auxetic behavior and enhancement of their mechanical properties. *Composite Structures* **2012,** *94* (8), 2373-2382.

221. Lakes, R., Advances in negative Poisson's ratio materials. **1993,** *5* (4), 293-296.

222. Sato, N.; Kurauchi, T.; Sato, S.; Kamigaito, O., Mechanism of fracture of short glass fibre-reinforced polyamide thermoplastic. *Journal of Materials Science* **1984,** *19* (4), 1145-1152.

223. Li, J.; Zhang, Y. F., The Tensile Properties of Short Carbon fiber reinforced ABS and ABS/PA6 composites. **2010,** *29* (11), 1727-1733.

224. Bondioli, F.; Cannillo, V.; Fabbri, E.; Messori, M., Epoxy-silica nanocomposites: Preparation, experimental characterization, and modeling. **2005,** *97* (6), 2382-2386.

VITA

Sevkan ÜLKER

EDUCATION

- ***Ph.D.*** (2017-2022): Department of Materials Science and Engineering, İzmir Institute of Technology, İzmir, Turkey
- ***M.Sc.*** (2013-2017): Department of Materials Science and Engineering, İzmir Institute of Technology, İzmir, Turkey
- ***B.Sc.*** (2006-2011): Department of Physics, Ege University, İzmir, Turkey

EMPLOYMENT HISTORY

- Researcher in Department of Materials Science and Engineering, İzmir Institute of Technology, İzmir, Turkey (2017-2022)
- Sales Support Assistant in IC Energy, İzmir, Turkey (2016-2017)
- Researcher in Department of Materials Science and Engineering, İzmir Institute of Technology, İzmir, Turkey (2013-2015)

PUBLICATIONS

- Ulker, S.; Guden, M., The effect of the temperature of heat treatment process and the concentration and duration of acid leaching on the size and crystallinity of nano-silica powders formed by the dissociation of natural diatom frustule. *Materials Express* **2022,** 12, 1094-1107.

SCHOLARSHIPS

- The Council of Higher Education 100/2000 Program (2017-2021): New Generation Composites and Multifunctional Nanocomposite Materials.